

Nanoscale Magnetic Imaging of Ferromagnetic Nanostructures

Inauguraldissertation

zur Erlangung der Würde eines Doktors der Philosophie

vorgelegt der
Philosophisch-Naturwissenschaftlichen Fakultät
der Universität Basel

von

Marcus Wyss

aus Hubersdorf SO, Schweiz

Basel, 2018

Originaldokument gespeichert auf dem Dokumentenserver der Universität Basel
edoc.unibas.ch

Genehmigt von der Philosophisch-Naturwissenschaftlichen Fakultät auf Antrag von

Prof. Dr. Martino Poggio
Fakultätsverantwortlicher

Prof. Dr. Dieter Kölle
Korreferent

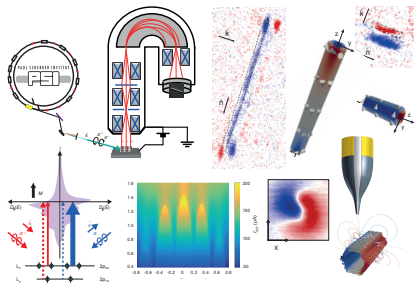
Basel, den 13.11.2018

Prof. Dr. Martin Spiess
Dekan

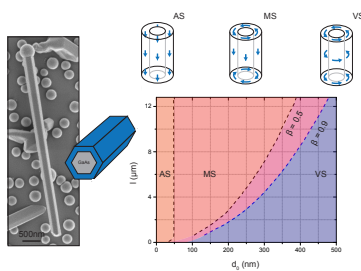
Introduction

Thesis Outline

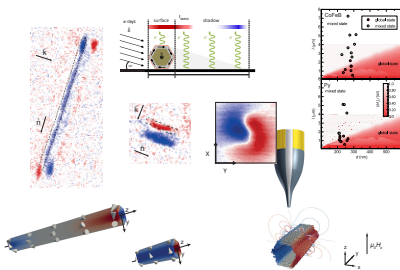
The thesis is structured as follows.



Chapter 1 provides an introduction into the working principles of two outstanding nanoscale magnetic imaging techniques. Namely the x-ray magnetic dichroism photoemission electron microscopy (XMCD-PEEM) under the use of synchrotron radiation and the scanning SQUID-on-tip technique, which was built in the lab from the beginning. At the end of the chapter the advantages and disadvantages of the two magnetic imaging techniques are described.



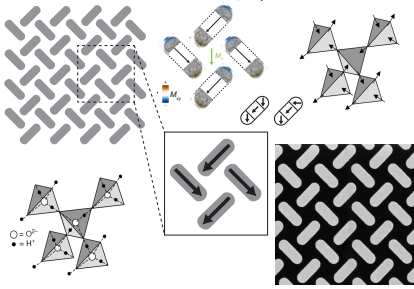
Chapter 2 is intended to provide a brief introduction into how tubular shaped ferromagnetic nanotubes are fabricated and how the magnetization behaves depending on the length and diameter in such three-dimensional architecture. Further, I would like to show how the samples for the x-ray magnetic dichroism photoemission electron microscopy (XMCD-PEEM) and the scanning SQUID-on-tip experiments are manufactured under the use of a precision micromanipulating method.



Chapter 3 is devoted to experimental results obtained by imaging the remnant magnetization configurations of ferromagnetic nanotubes (FNTs) using x-ray magnetic circular dichroism photoemission electron microscopy (XMCD-PEEM) at room-temperature. The obtained magnetic images of the FNTs provide direct evidence for flux-closure configurations, including a global vortex state, in which magnetization points circumferentially around the tube axis. Furthermore, micromagnetic simulations predict and

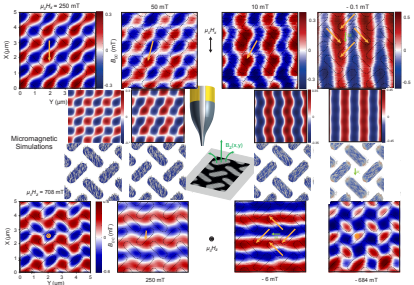
measurements confirm that vortex states can be programmed as the equilibrium remnant magnetization configurations by reducing the ratio of the FNTs length and diameter. The magnetic stray-field distribution of FNTs, with different lengths, are imaged at cryogenic temperatures using the scanning SQUID-on-tip technique in series of applied magnetic fields perpendicular to the long axes of them. Both magnetic imaging techniques show the promise of using ge-

ometry to program both the overall equilibrium magnetization configurations and the reversal process in nanomagnets.



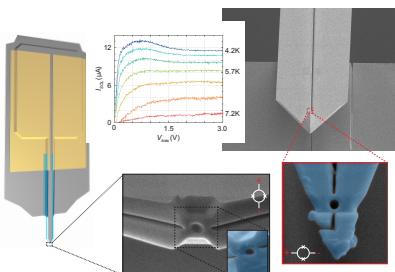
Chapter 4 This chapter provides an introduction to artificial spin ice systems. In particular a novel geometry, the “chiral ice” will be introduced. Furthermore the design as well as the fabrication of this system, which consists of magnetostatically-coupled nanomagnets will be described. Recent experimental measurements will be discussed, which have shown that the magnetostatic field at the edges of the array is responsible for an observed collective rotation of the average magnetization in a unique sense during thermal relaxation at room temperature, analogous to a ratchet. In thicker samples, two energetically stable edge states exist due to the bending of the magnetization at the edges of the nanomagnets. Furthermore, I show that the edge bending increases the number of degrees of freedom of the magnetization in artificial spin ice and that these additional degrees of freedom are not captured in dipolar models, which are typically used in studies of artificial spin ice systems.

relaxation at room temperature, analogous to a ratchet. In thicker samples, two energetically stable edge states exist due to the bending of the magnetization at the edges of the nanomagnets. Furthermore, I show that the edge bending increases the number of degrees of freedom of the magnetization in artificial spin ice and that these additional degrees of freedom are not captured in dipolar models, which are typically used in studies of artificial spin ice systems.



Chapter 5 This chapter describes measurements of the magnetic stray field distribution of the “chiral ice” as a function of different applied magnetic in-plane and out-of-plane fields. The experiment is performed at cryogenic temperature and for the magnetic imaging the scanning SQUID-on-tip technique is used. The measured stray field distributions at different magnetic field strengths are very well described by the micromagnetic simulations of the expected distributions. In particular, the simulations elucidate the stray field distribution at zero field. Indeed, the measurements show that successive regions of alternating stray field intensity are separated by a boundary that displays a meander pattern. The simulations demonstrate that this pronounced pattern is due to the bending of the magnetization at the edges of the nanostructures. The meander pattern is almost inexistent assuming simulations with uniformly magnetized nanomagnets. These observations demonstrate that the number of degrees of freedom in artificial spin ice is in fact much larger than captured in dipolar models. Such degrees of freedom may find use in reprogrammable magnonic crystals, where the in-plane magnetic field has been shown to allow tuning of the band frequency.

distribution at zero field. Indeed, the measurements show that successive regions of alternating stray field intensity are separated by a boundary that displays a meander pattern. The simulations demonstrate that this pronounced pattern is due to the bending of the magnetization at the edges of the nanostructures. The meander pattern is almost inexistent assuming simulations with uniformly magnetized nanomagnets. These observations demonstrate that the number of degrees of freedom in artificial spin ice is in fact much larger than captured in dipolar models. Such degrees of freedom may find use in reprogrammable magnonic crystals, where the in-plane magnetic field has been shown to allow tuning of the band frequency.



Chapter 6 describes a further development of the SQUID-on-tip technology by extending its capability by one measurable size. The idea is to use instead of a hollow quartz tip a commercially available Si-cantilever, normally used for atomic force microscopy (AFM) imaging, as a support. To realize such a probe, a focused ion beam (FIB) is used to mill the apex of the Si-cantilever in a suitable shape, which later serves as a template for the nanoSQUID. This thesis show, how those Si-cantilevers are machined using a

focused ion beam (FIB) and what different configurations were manufactured to get a working Pb SQUID at the apex of a mechanical resonator. With such a new technology we expect to retain the favorable properties of the SQUID-on-tip, while also adding sensitivity to tip-sample forces, which can be read out under the use of standard non-contact AFM techniques. This hybrid scanning probe should allow to image the topography and the magnetic stray field of a magnetic nanostructure simultaneously. Thereby it would be possible to correlate changes in the measured magnetic stray field distribution directly with the surface topography of the sample.

Contents

Introduction	III
Thesis Outline	III
1. Introduction to two nanoscale magnetic imaging techniques	1
1.1. Synchrotron Radiation	1
1.1.1. Photoemission electron microscopy (PEEM)	2
1.1.2. X-ray magnetic circular dichroism (XMCD)	5
1.2. Superconducting Quantum Interference Device: A highly sensitive magnetic field probe	7
1.2.1. Introduction	7
1.2.2. Superconducting Quantum Interference Device (SQUID)	7
1.3. Scanning Probe Microscopy	11
1.3.1. Development of the SQUID-on-tip technique	11
1.3.2. Fabrication of a SQUID-on-tip sensor	13
1.3.3. Characterization of a SQUID-on-tip sensor	15
1.3.4. Scanning SQUID Microscopy	18
1.4. Comparison of the introduced magnetic imaging techniques	20
2. Ferromagnetic Nanotubes	23
2.1. Introduction	23
2.2. Fabrication of ferromagnetic nanotubes	24
2.3. Equilibrium states in ferromagnetic nanotubes	26
2.4. Sample Preparation for the XMCD-PEEM experiments	27
2.5. Sample Preparation for scanning SQUID-on-tip experiments	28
3. Imaging of magnetic configurations in ferromagnetic nanotubes	31
3.1. Magnetic configurations of ferromagnetic nanotubes studied with PEEM in remanence	31
3.2. Numerical Micromagnetic Simulations	36
3.3. Comparison to micromagnetic simulations	37
3.4. Conclusion to magnetic configurations in FNTs imaged with XMCD-PEEM	39
3.5. Imaging stray magnetic field of individual ferromagnetic nanotubes using scanning SQUID-on-tip	40
3.6. Conclusion to the magnetic imaging under the use of two different magnetic imaging techniques	44
4. Introduction to Artificial Spin Ices	45
4.1. From water ice to artificial spin ice	45
4.2. “Chiral ice” - an artificial spin ice system	47
4.3. Fabrication of a chiral artificial spin ice system	50

5. Imaging of a Chiral Artificial Spin Ice System	51
5.1. Defining suitable working points for the magnetic reversal experiment	51
5.2. Magnetic reversal measurements with applied out-of-plane magnetic fields . .	55
5.3. Magnetic reversal measurements with applied in-plane magnetic fields	57
5.4. Micromagnetic Simulations of the in-plane field experiment	59
5.5. Conclusion and Outlook	63
6. A nanoSQUID on a Si-Cantilever: A hybrid system as a new magnetic imaging tool	65
6.1. Pb nanoSQUID on a Si-cantilever	65
6.2. Fabrication of a Pb nanoSQUID on a Si-cantilever	66
6.3. A single Dayem bridge at the apex of a Si-cantilever	66
6.4. Two Dayem bridges at the apex of a Si-cantilever	68
6.5. Further development of the technology	72
6.6. Next steps in the development of this promising scanning probe technology . .	74
6.7. A tungsten carboxyl nanoSQUID on a Si-cantilever	74
7. Conclusion, Discussion and Outlook	77
Acknowledgements	79
Bibliography	81
A. A: XMCD-PEEM Measurements	89
A.1. XMCD-PEEM sample holder	89
A.2. XMCD-PEEM, PEEM, and SEM images	89
B. B: Phase Diagrams of the XMCD-PEEM Measurements	97
C. C: Scientific Systems	101
C.1. home-built scanning microscope	101
C.2. home-built thermal Pb evaporation system	102
D. D: Pb nanoSQUID on Si-cantilever	103
D.1. Evaporation mask for the fabrication of Au-pads on the carrier chip	103
D.2. Si-cantilever properties	103
D.3. Single Dayem bridge on a Si-cantilever	105
D.4. Configuration ①: Two Dayem bridges on a Si-cantilever	105
D.5. Configuration ②: Two Dayem bridges on a Si-cantilever	105
D.6. Configuration ③:	106
E. E: Chiral Artificial Spin Ice	107
E.1. Magnetic reversal measurements with applied in-plane magnetic fields	107
E.2. Magnetic reversal measurements with applied out-of-plane magnetic fields . .	108
Curriculum Vitae	109
Education	109
Scientific Talks at Conferences	110

List of Publications	111
--------------------------------	-----

1. Introduction to two nanoscale magnetic imaging techniques

This chapter is intended to provide an introduction into the working principles of two nanoscale magnetic imaging techniques. First I would like to introduce synchrotron radiation as an outstanding imaging tool, which offers the opportunity to image element selective the in-plane direction of the local net magnetization of magnetic materials at the surface to a certain depth. Additional information about the average magnetization of the volume traversed by the x-rays is obtained in the shadow region, which allows a more complete description of the magnetic state.

Further, I would like to introduce the scanning SQUID-on-tip (SOT) technique, which was built in the lab from the beginning in collaboration. The fabrication as well as the characterization of this highly sensitive sensors to the magnetic stray field components in z -direction, is described. Moreover I would like to highlight the advantages and the disadvantages of these two magnificent nanoscale imaging techniques.

1.1. Synchrotron Radiation

Synchrotron radiation has become in the last two decades an outstanding imaging tool for condensed matter physics. This is mainly because synchrotron radiation provides the unique capabilities to study magnetic phenomena. Especially x-ray techniques, with the unique advantage of coupling directly to the spin-resolved electronic states of interest, allow to get a deeper understanding of phenomena in magnetic materials. But synchrotron radiation is not only used for condensed matter physics; its application ranges from life science, where especially pharmaceutical companies and medical researchers use macromolecular crystallography to obtain structural information about promising compounds for new drug candidates up to environmental science, where mainly the high brilliance allows high-resolution study of ultra-dilute substances, the identification of species and the ability to track pollutants as they move through the environment. All in all, one could say synchrotron radiation is a powerful tool which can be used for many different applications in science.

In general, a synchrotron consists of a circular ring, also called storage ring, where electrons are accelerated up to a relativistic speed and maintained at a fixed energy in the range of few GeV. The electrons travel in a closed loop under ultrahigh vacuum and they are kept in the orbit by strong magnetic fields. At a desired time by a magnet, called bending magnet, the trajectory of an electron can be changed due to the Lorentz force. The electron loses energy by emitting electromagnetic radiation. The radiation emitted is the typical dipole radiation, but thanks to very high speed it suffers from a relativistic contraction which leads to a forward peaked beam, where the energy of the radiation is shifted to the X-ray region [1]. The emitted radiation has a continuous energy spectrum ranging from the infrared (1.2 meV - 1.6 eV) to the hard x-ray (6 - 300 keV) region. The position of the photon flux peak depends on the energy of the circulating electrons and the magnetic field of the bending magnet. The higher the energy

of the electrons, the higher the peak position. That's why storage rings are classified according to the energy of the circulating electrons ranging from 2 to 8 GeV with a few exceptions. An important measure of the quality of the source is the so-called brilliance. The brilliance is the number of emitted photons per second in a narrow energy bandwidth (BW) per unit solid angle. This quantity takes into account the ability of the storage ring to generate a very narrow cone of radiation out of a very small source dimension [1]. Some measurements of this thesis were performed at the Surface/Interface: Microscopy (SIM) beamline of the Swiss Light Source (SLS) at the Paul Scherrer Institut (PSI). The performed measurements are described in detail in chapter 3. At The SLS, the energy of the circulating electrons in the storage ring is 2.4 GeV and the brilliance is given to be 10^{15} photons/s/0.1%BW/0.4 A at 1 keV.

1.1.1. Photoemission electron microscopy (PEEM)

Part of this work was performed at the Surface/Interface: Microscopy (SIM) beamline of the Swiss Light Source (SLS) at the Paul Scherrer Institut (PSI) using the photoemission electron microscope (PEEM) [8].

In a PEEM, emitted electrons of a sample under illumination with x-rays are imaged. A high flux of soft x-rays with variable polarization are produced by the SIM beamline from an undulator source located in the storage ring, which has a constant value of current of around 400 mA at the SLS. The photon energy of the SIM beamline ranges from 90 eV up to 2000 eV [11]. By tuning the x-ray energy to the Fe L₃- or to the Fe L₂-edge the local net magnetization of the sample surface can be imaged employing the x-ray magnetic circular dichroism (XMCD). The angle between the incoming monochromatic x-rays and the sample surface is $\theta_k = 16^\circ$ as shown in the schematic of the SIM beamline in figure 1.1.

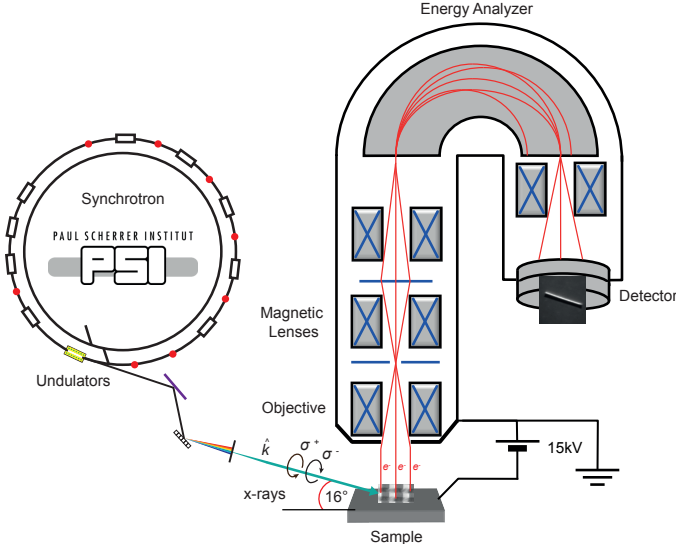


Figure 1.1. | Schematic of the Surface/Interface: Microscopy (SIM) beamline of the Swiss Light Source (SLS) at the Paul Scherrer Institut (PSI) and the associated photoemission electron microscope (PEEM) consisting of the sample, accelerating voltage, lenses, energy filter, and detector. For the beamline just the most important components are depicted. The dimensions as well as the paths of the x-ray beam and the photoelectrons do not display the actual dimensions in the setup.

The beamline consists of two 3.8-m-long undulators as insertion devices behind each other. The undulators have a periodic magnet structure, which forces traversing electrons to undergo oscillations and thus radiate energy followed by a collimating mirror, which narrows the beam of waves directly after the shielding wall, a plane grating monochromator and focusing mirrors. Under the use of the so-called tune-detune mode, a fast switching of the wave polarization is possible in the range of 1-2 seconds. To match the small energy band pass in the range of meV of the monochromator one of the two undulators is tuned to the energy, so that x-rays with a specific polarization are delivered to the sample chamber of the PEEM. The second undulator is detuned by changing the gap a few millimeters, this leads to a shift of the center of the emitted photon energy away from the energy band pass of the monochromator such that nearly no intensity can pass [11].

In general PEEM is the imaging of excited secondary electrons, which reveal an intensity map proportional to the local x-ray absorption cross section to a certain depth. The maximum probing depth of total electron yield depends on the core level energy and ranges from 15 to 141 Å. It was found that the signal intensity decreases exponentially with coating thickness [12]. Due to the photoelectric effect, electrons leave the sample after excitation with x-rays. A strong electric field of 15 kV is applied between the sample and the objective lens of the PEEM to accelerate the low energy secondary electrons. This acceleration is important to maintain the local information about the spatial origin of all emitted electrons, which would be impossible with low energy electrons. Accordingly fast electrons are imaged with an electron microscope. The image is magnified a hundred- or thousand-fold with a set of magnetic lenses. To optimize the path of the electrons through the microscope and to correct image distortions, deflectors and stigmators are used. The electrons are detected with a multichannel plate and a phosphor screen and imaged with a CCD camera. The probing depth of the measurements could be tuned by using an energy filter, which allows to select specific electrons for imaging. The emitted electrons move on parabolic trajectory from the sample to the microscope. Their exact path depends on the angle and the velocity. Hence, electrons emitted from the same spot will not appear at the same spot on the image. This leads to an increased spot size. The spatial resolution of a PEEM is determined by the angular- and velocity-variations of the electrons which leads to the spherical and angular aberration of the imaging system. It follows that a very rough sample surface will deteriorate the spatial resolution. Furthermore, a large energy spread of the electrons will reduce the spatial resolution. To reduce the electron energy spread an aperture [13] or as already mentioned earlier in this subsection an energy filter [15] can be used at the expense of intensity. The best spatial resolution of PEEM reported so far is about 20 nm [16] or even better in an aberration-corrected photoemission electron microscope, where a spatial resolution about 5.4 nm [17] was achieved.

The characteristic magnetic XMCD contrast is obtained by taking PEEM images using x-rays with opposite helicity σ^+ and σ^- and normalize to their sum. The asymmetry image can be calculated using equation 1.1.

$$I_{\text{XMCD}} = \frac{I_{\sigma^+} - I_{\sigma^-}}{(I_{\sigma^+} + I_{\sigma^-})} \quad (1.1)$$

Figure 1.2 shows in (a) a SEM image of a ferromagnetic nanotube lying on a Si substrate and in (b) the corresponding absorption image taken from the same area at the Fe L₃-edge using circular left polarized x-rays σ^+ , followed in (c) by another absorption image taken with circular right polarized x-rays σ^- . In (b), the direction of the incoming x-ray polarization vector \hat{k}

is shown, depicted as a white arrow. In both images, one can already see the absorption asymmetry in those parts where they occur. The pixelwise division of the absorption images, which delivers a XMCD image as shown in (d) with enhanced magnetic contrast, the asymmetry is much more pronounced at those positions, where an asymmetry of the absorption images is located. In this specific case, the local net magnetization at the surface points parallel (antiparallel) to the incoming x-ray polarization vector \hat{k} at both ends of the ferromagnetic nanotube, which in the XMCD image leads to a black (white) contrast. The rest of the ferromagnetic nanotube shows an almost gray contrast, which means that the local net magnetization at the surface points perpendicular to \hat{k} and is therefore axially aligned.

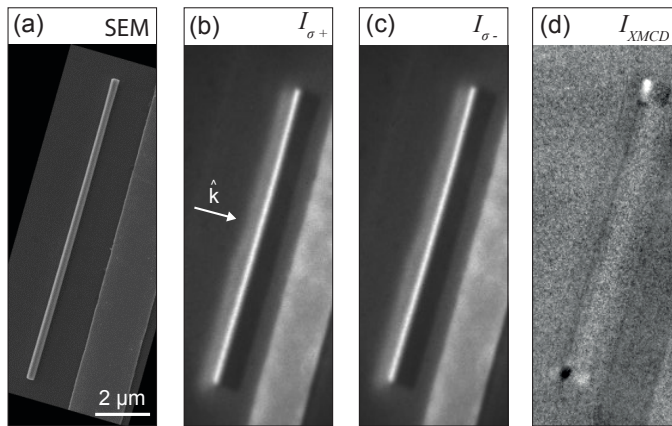


Figure 1.2. | (a) SEM of an 11.3- μm -long CoFeB nanotube placed close to a Au alignment marker visible on the right of the image. (b) and (c) are absorption images recorded at the Fe L_3 -edge using x-rays with opposite helicity σ^+ and σ^- . In (b) the direction of the x-ray polarization vector \hat{k} is shown. (d) shows the obtained XMCD image by the division of σ^+ and σ^- under the use of equation 1.1. The enhanced magnetic contrast could be clearly seen at those positions, where an asymmetry of the absorption images is located, which is in this case at the end of the nanotube. Black contrast shows that the magnetization is pointing parallel to the direction of \hat{k} and white means anti-parallel, particular visible at the bottom- and top-end of the nanotube, indicating opposing vortex states at both ends. The center of the nanotube shows a gray contrast which means that the magnetization is axially aligned. The XMCD signal, visible in the shadow behind the nanotube, will be described more in detail in chapter 3.

For the image acquisition for each polarization an exposure time of one second was chosen, averaged 10 times. The switch of the polarization takes 1-2 seconds. We obtain XMCD image sequences with a time frame of 21 seconds per image. Because we image static and not dynamic magnetic configurations [18, 19], the chosen time frame is sufficient. During image acquisition the sample may slightly move due to mechanical drift. To consider this circumstance in the PEEM images as well as in final XMCD image, a drift correction program is applied to the acquired image sequences. This program uses the first PEEM image of an image sequence as a reference. On the reference image one has to define a region where the x-ray absorbing structure is located. If the structure in this defined region slightly drifts, the correction program shifts the location of the second image in that way that the structure is again superimposed. This process is repeated until the entire stack of the recorded images are superimposed giving a drift corrected image sequence, which can be used to calculate the asymmetric XMCD image.

1.1.2. X-ray magnetic circular dichroism (XMCD)

A standard method to study magnetic thin films and surfaces is x-ray magnetic circular dichroism (XMCD). Strong XMCD effects appear at the L-edges of the transition metal ferromagnets Iron (Fe), Cobalt (Co) and Nickel (Ni). The reason for this is that the d -states carry most of the magnetic moment. Dichroism in general is a polarization dependent absorption behavior, where in the case of an anisotropic spin distribution it is called magnetic dichroism. The XMCD effect was predicted by Erskine and Stern in 1975, where they performed band structure calculations for the $M_{3,2}$ absorption edges of Ni [2]. The first experimental results using this effect were obtained in 1987, where a significant XMCD effect at the K-absorption edge of an Fe foil was measured [3]. A simple description of the XMCD effect for $3d$ transition metals provides the so-called two-step model [4]. In this model, the first step is described as follows: Electrons from a spin-orbit-split core-level, for example $2p_{3,2}$ and $2p_{1,2}$, are absorbed through circularly polarized x-ray photons with a helicity of $+1$ (σ^+), leaving empty core states. This leads to the excitation of spin-polarized electrons into the unoccupied $3d$ -band. This band is exchange split into spin-up and spin-down bands, as illustrated in 1.3 (a) and due to the exchange interaction the density of unoccupied states at the Fermi level is different for the two spin directions.

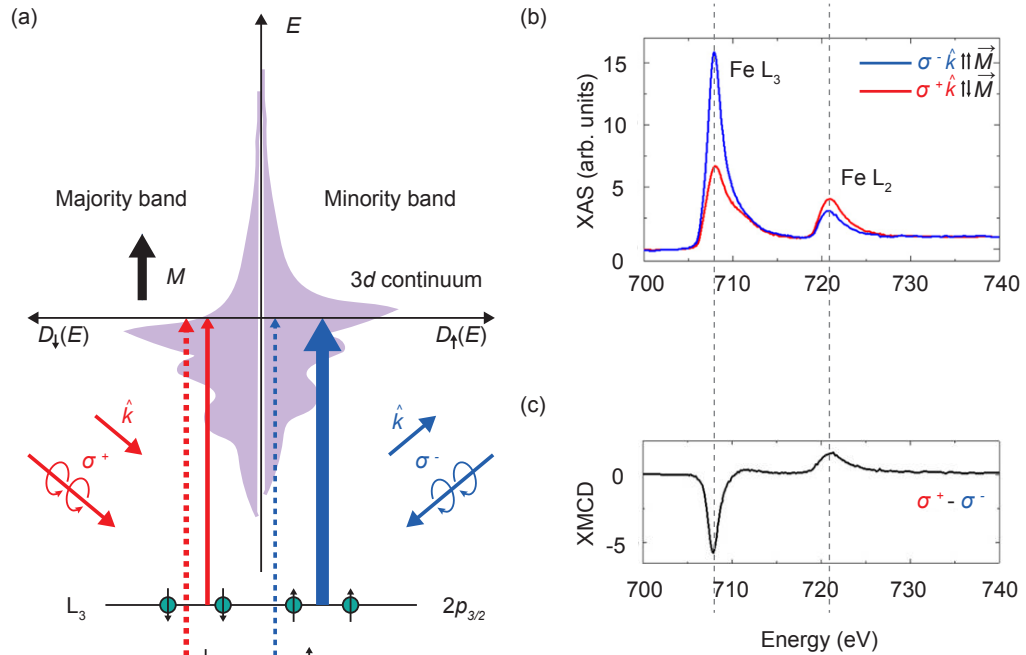


Figure 1.3. | Schematic of the electronic transitions in a Fe atom where the electrons are excited with circularly polarized x-rays having a helicity of ± 1 (σ^{\pm}). (b) X-ray absorption spectrum in the energy range where the Fe L_3 - and L_2 is located. The XAS is recorded using x-rays with opposite helicity σ^+ and σ^- . (c) corresponding XMCD signal. The images in (b) and (c) are adapted from [5].

The transition of an electron having a spin pointing up ($m_s = +1/2$) or down ($m_s = -1/2$) could be approximated as a magnetic dipole transition, there the selection rules defines which transitions are allowed. All transitions between orbitals follow the selection rules, which states

that the only allowed transitions from $2p_{3/2,1/2}$ into empty d -states are $\Delta l = \pm 1$, $\Delta m_l = 0, \pm 1$ and $\Delta m_s = 0$.

By summing up all possible excitations weighted by their probabilities the spin polarization of the excited electrons are found. 62.5 % of excited electrons carry a spin of $m_s = +1/2$, which are arising from the $2p_{3/2}$ state and only 37.5 % carry a spin of $m_s = -1/2$. From the $2p_{1/2}$ state 75 % of excited electrons carry a spin of $m_s = -1/2$ and only 25 % of $m_s = +1/2$. It is remarkable that the sign of the spin polarization is different for different $2p$ -states. If there is no spin-orbit splitting and therefore no energy gap between $2p_{3/2}$ and $2p_{1/2}$ states, the averaged spin polarization is zero. If the helicity of circularly polarized x-ray photons is changed to -1 (σ^-) the result is the same but with reversed sign. In the second step the spin-polarized electrons are analysed by a spin-resolving detector consisting of the exchange split d -final-state. This spin-resolving technique, called photoemission electron microscope (PEEM) was mentioned in the previous subchapter 1.1.1.

In figure 1.3 (b) a typical x-ray absorption spectrum (XAS) taken with x-rays having a helicity of ± 1 (σ^\pm) is shown. The XAS are recorded in the energy range from 700 - 740 eV, where the Fe L_3 - ($E \sim 708$ eV) and L_2 -edge ($E \sim 721$ eV) is expected [6]. At both resonance peaks a clear asymmetry of the absorption cross-section is visible. The difference depends on the helicity of the incoming x-rays and is described more in detail in this subchapter. By subtracting the σ^- -curve from the σ^+ -curve one get the typical XMCD signal as shown in 1.3 (c). This XMCD signal includes information about the direction of the local magnetization (M) of the sample under illumination. The intensity of the XMCD signal is a measure of the projection M along the propagation direction \hat{k} of the circularly polarized x-rays [1, 7]. The intensity of the signal is given by the following equation, where α is the angle between M and \hat{k} :

$$I_{\text{XMCD}} \propto M \hat{k} = \langle M \rangle \cos(\alpha) \quad (1.2)$$

Ferromagnetic domains with a magnetization pointing parallel or antiparallel to the x-ray polarization vector \hat{k} corresponds to a high intensity or a low intensity in the spatially resolved XMCD image obtained using the previous described photoemission electron microscope (PEEM). Magnetic domains with a magnetization pointing perpendicular to the x-ray polarization vector \hat{k} will have the same intensity as the non-magnetic environment [7].

At this point, I would like to refer the reader to the book Magnetism and Synchrotron Radiation from E. Beaurepaire et. al. [1], which describes more in detail the XMCD-PEEM technique. Or a review written by Loïc Le Guyader et. al. [8], which describes recent activities at the Surface/Interface: Microscopy (SIM) beamline of the Swiss Light Source (SLS) at the Paul Scherrer Institut (PSI), with a focus on instrumental and analytical developments.

1.2. Superconducting Quantum Interference Device: A highly sensitive magnetic field probe

1.2.1. Introduction

In superconductors, the current is carried by pairs of electron with opposite spins and momentum called cooper pairs and not by single electrons. This mechanism has been described theoretically by the BCS-theory in 1957 [21]. If the temperature is lower than the transition temperature (T_c) of the superconductor, the binding energy of the Cooper pairs is large compared to the thermal energy scattering. As a result, Cooper pairs propagate throughout the superconductor with a coherent phase and current flows without any resistance.

Superconductivity is found in a wide range of materials. It is present in pure elements like mercury (Hg), where it was first discovered by H. K. Onnes in 1911, niobium (Nb) or lead (Pb). It is also present in alloys like NbTi and NbN as well as in organic materials such as Rb_3C_{60} and $K_{3.3}Picene$, where all have a slightly higher T_c compared to the pure metals or even higher in ceramics like $YBa_2Cu_3O_7$ or $HgBa_2Ca_2Cu_3O_8$.

1.2.2. Superconducting Quantum Interference Device (SQUID)

A Superconducting Quantum Interference Device (SQUID) is one of the most sensitive magnetic field sensors available [22]. A SQUID consists of a superconducting loop intersected by two Josephson junctions (JJ). Two fundamental phenomena in superconductors are responsible for the working principle of a SQUID, these are the flux quantization and the Josephson effect.

To understand the concept of flux quantization in superconducting material, one has to consider a superconducting ring much thicker than the London penetration depth λ_L . The London penetration depth is a characteristic length in superconductors and refers to the distance where the magnetic field inside a superconductor decays to zero. For Pb, the London penetration depth was determined to be 30.5 nm [27]. If a small magnetic field is applied to the superconducting ring, no flux will thread the superconducting ring, due to screening currents flowing on the outer surface of the ring wall, which screen the magnetic field. In addition, screening currents flow on the outer surface of the ring wall to expel the applied magnetic field from the superconducting material. A screening current with opposite direction flows on the inner surface of the ring to keep the applied magnetic field outside the superconducting material. Since the thickness of the superconducting material is much larger than the London penetration depth, one can choose a closed circle deep inside the superconducting material, where in good approximation the supercurrent flowing in the ring is zero. The fluxoid quantization condition then simplifies to

$$\int_S B ds = n\Phi_0 \quad (1.3)$$

Here, the cross-sectional area bounded by the curve S , where ds is the arc length, Φ_0 is the magnetic flux quantum, n is a integer multiple and B is the magnetic field applied perpendicular to the superconducting ring. The equation shows that when the applied magnetic field is removed, the magnetic flux trapped in the ring is an integer multiple of the flux quantum.

Therefore equation 1.3 can be considered as a statement of flux quantization. The experimental proof of magnetic flux quantization in a superconducting ring was provided in 1961. R. Doll and M. Nábauer showed the flux quantization in a hollow Pb cylinder using a resonance method. They measured the mechanical torque exerted by a magnetic field on a small superconducting Pb tube with frozen-in magnetic flux [31]. At the same time another group observed experimentally quantized values of magnetic flux trapped in hollow tin cylinders. They set the cylinder in motion and measured the field with pickup coils. Further they found that the quantized unit is not $n \cdot \frac{h}{e}$, but $n \cdot \frac{h}{2e}$ within experimental error. Responsible for this double electron charge according to the BCS-theory is the Cooper pair.

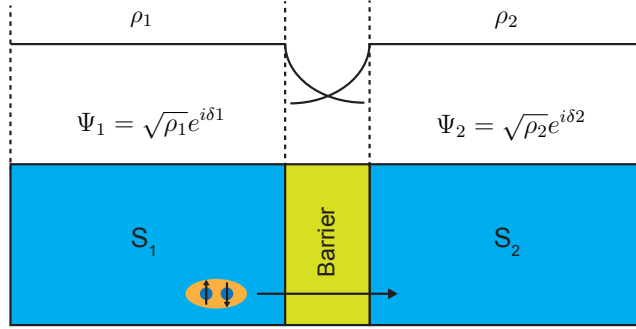


Figure 1.4. | Scheme of a Josephson junction. A thin insulator barrier (few nm) separates the two superconductors. The overlap of the macroscopic wave functions allows the tunneling of the Cooper pairs. Adapted from C. Granata et al. [24].

As already mentioned before in a SQUID the superconducting loop is separated by two thin insulating barriers of just a few nanometers. They divide the loop into two superconducting regions (S_1 , S_2). A scheme of a insulating barrier or Josephson junction is shown in figure 1.4 The whole ensemble of Cooper pairs on the left side as well as on the right side, can be described through macroscopic wave functions $\Psi_1 = \sqrt{\rho_1}e^{i\delta_1}$ and $\Psi_2 = \sqrt{\rho_2}e^{i\delta_2}$. Where $\sqrt{\rho_1}$ and $\sqrt{\rho_2}$ are the magnitude and δ_1 and δ_2 the phases of the macroscopic wave functions. In the absence of interactions between S_1 and S_2 the phases δ_1 and δ_2 will in general be different. Bringing them into contact over a large area, causes the phases to equalize: $\delta_1 = \delta_2$. If a thin insulating barrier separates the two superconductors, weak coupling is possible because of the overlap of the macroscopic wave functions as shown in 1.4, which allows Cooper pairs to tunnel through the barrier region. This effect is well known as the DC Josephson effect [26, 29]. A phase difference $\Delta\delta$ occur across the junction, which corresponds to a zero voltage supercurrent (I_s) up to a current value called Josephson critical current I_c . In the absence of any potentials the supercurrent I_s through a JJ varies sinusoidally with the phase difference $\Delta\delta(t) = \delta_2 - \delta_1$ and therefore shows the current-phase-relation. This effect is described by the first Josephson equation.

$$I_s(t) = I_c \cdot \sin(\Delta\delta(t)) \quad (1.4)$$

Here, $\Delta\delta$ is the phase difference between the wave functions on both sides and I_c the critical current of the barrier. In the presence of a bias voltage U between the two superconductors,

the phase evolves with time t according to the second Josephson equation, and is known as the voltage-phase relation.

$$U(t) = \frac{\Phi_0}{2\pi} \cdot \frac{\partial \Delta \delta}{\partial t} \quad (1.5)$$

Here, Φ_0 is the magnetic flux quantum given by $\Phi_0 = h/2e = 2.07 \cdot 10^{-15}$ Vs and U is the voltage across the junction. The first equation 1.4 describes the static (DC) and the second 1.5 the dynamic (AC) properties of a Josephson junction. Biased with a DC current, the voltage across the JJ remains zero up to the I_c as shown in the typical current-to-voltage characteristics (IVC) in figure 1.5 (b). Above the critical current the resistive state of the junction is reached where single electrons tunnel through the barrier and the IVC shows then a completely different behavior compared to the superconducting state. In (b) the IVC for integer n and half-integer $n+1/2$ values of applied flux is shown. The maximum current is obtained using equation 1.6.

$$I_c = 2I_0 \cdot \left| \cos\left(\pi \frac{\Phi}{\Phi_0}\right) \right| \quad (1.6)$$

In figure 1.5 a) a schematic view of the DC SQUID is shown, where I_b is the applied DC current and I_s is the circulating supercurrent flowing in the superconducting ring intersected by two JJs with the phases δ_1 and δ_2 . The maximum supercurrent that can flow across the ring is limited by the sum of the two critical currents of the two JJ. The magnetic flux Φ enclosed inside the superconducting ring modulates the critical current I_c periodically, with a period of one flux quantum $\Phi_0 = h/2e$. When the current in both arms are identical and the inductance and therefore the screening parameter $\beta_L = \frac{2LI_0}{\Phi_0}$ is very low, the critical current of the DC SQUID thus modulates between $2I_0$ and 0. For nonzero values of β_L a reduction of the modulation depth occurs. This illustrates the response of the DC SQUID in the superconducting state. If we now look to the case of a nonzero DC voltage V across the JJ in (b) one can see that the critical current (ΔI_c) as well as the voltage (ΔV) modulates with the applied flux Φ .

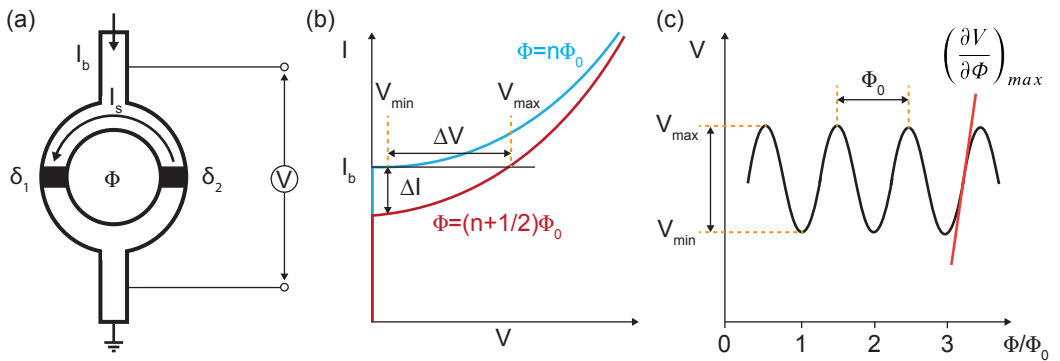


Figure 1.5. | (a) Schematic view of the DC SQUID. (b) Current-to-voltage-characteristics (IVC) at integer and half-integer values of applied flux. The working point is set by a constant bias current I_b . (c) Voltage-to-flux ($V - \Phi$) characteristic at a fixed bias current showing the periodic dependence of the SQUID voltage on applied flux. The working point is set to the position where the voltage-to-flux SQUID transfer function is maximize.

The corresponding voltage-to-flux ($V - \Phi$) characteristic at a constant bias current I_b is shown in figure 1.5 (c). The $V - \Phi$ characteristic shows that the modulation in I_c directly transfers into a modulation of the voltage V . This I_c modulation, caused by an interference of the superconducting wave functions in both SQUID arms, forms the basis of the working principle of the DC SQUID. A simple read-out method for SQUIDs, having nonhysteretic IVCs, is to bias with a current slightly above the maximum value of I_c . The DC voltage (V) across the junctions is read out directly as a function of applied magnetic flux. Using this read-out method, the SQUID acts directly as a flux-to-voltage transducer. The I_b is chosen in such a way that the amplitude of the voltage modulation is maximized and the applied flux is to be $(2n+1) \Phi_0/4$ ($n=0, 1, 2, \dots$), such that the voltage-to-flux transfer coefficient $|(\partial V/\partial \Phi)|_{max}$ is a maximum as shown in the $V - \Phi$ modulation in figure 1.5 c). As a result, the SQUID output voltage signal $\partial V = V_\Phi \partial \Phi$ in response to small magnetic flux signal $\partial \Phi$ is maximum. The SQUID can be operated in a small-signal mode around this optimal working point, which is typically located near the steepest part of the $V - \Phi$ characteristic. The proportionality between the voltage and the flux is maintained only for very small $\partial \Phi$, if the peak-to-peak flux amplitude exceeds the linear flux range – the so-called dynamic range – the output becomes strongly distorted. Under the use of a flux-locked feedback loop (FLL), the SQUID can be kept in this optimal working point. The deviation of the SQUID voltage V from the optimal working point is amplified, integrated, and fed back into the SQUID via a feedback resistor R_{FB} and a feedback coil, which is magnetically coupled to the SQUID via a mutual inductance. To make the impedance of the feedback coil negligible in the frequency range of interest, feedback resistances in the k Ω range are used, usually 10 k Ω , 23.1 k Ω or 30 k Ω . The flux in the SQUID is kept constant by the negative feedback for infinite integrator gain and the voltage V_{FB} across the feedback resistor depends linearly on the applied flux. The dynamic range can easily be made larger by decreasing the R_{FB} and/or increasing the inductance of the feedback coil.

At this point, for more information about the fundamentals and technology of SQUIDs and SQUID systems, I would like to refer the reader to the book *The SQUID Handbook* from J. Clark et. al. [22] or to a recently published review paper including recent applications of scanning SQUID microscopy from M. J. Martínez-Pérez et al. [23]. Another recently published review, which discusses the theoretical aspects, the fabrication techniques, the different nanoSQUIDs and the relative nanoscale applications [24].

1.3. Scanning Probe Microscopy

A scanning probe microscope has certain elements which are common to all different types. First of all a short-range interaction is sensed by a local probe with a spatial resolution, which depends on the geometrical shape of the probe itself and the distance to the sample. Scanning probe microscopy (SPM) covers a lateral range of imaging from several 100 μm down to few pm. Second, the probe is scanned over the surface under study by using piezoelectric actuators movable in three-dimensions and the measured quantities are recorded and processed in a computer system [48]. Based on a variety of tip-sample interactions the family of scanning probe microscopes have several members. A very prominent member from this family is the scanning tunneling microscope (STM) invented by G. Binnig and H. Rohrer in 1982 [49]. In the STM, a sharp metallic tip is scanned over the surface at a distance less than 1 nm. The distance is controlled by the tunneling current between the tip and the conducting surface. The atomic resolution of a STM is reached because the tunneling current is flowing from the very last atom of the tip apex to single atoms at the surface. A further development of this technique was the spin-polarized scanning tunneling microscopy which allows the investigation of magnetic structures at an atomic scale. Another very successful member is the atomic force microscope (AFM) which was developed in 1986 [50] and could image atomic-scale topography. Compared to the STM one can also map non-conductive surfaces. Shortly after the invention of the AFM it was determined that by equipping the force microscope with a ferromagnetic probe the detection of magnetostatic interactions at a local scale is possible, which could then be raster-scanned across any magnetic sample and was therefore named magnetic force microscope (MFM) [51]. These days, it is performed in air, liquid, vacuum, and at a variety of temperatures. Under ideal conditions, state-of-the-art MFM can reach spatial resolutions down to 10 nm [52], though more typically around 100 nm. In 2009, its application to magnetic resonance, magnetic resonance force microscopy (MRFM), resulted in the first demonstration of three-dimensional nuclear magnetic resonance imaging (MRI) with nanometer-scale resolution [54].

More recently a lot of effort has been put into the development of scanning NV center magnetometry. NV centers are optically addressable electronic defects in diamond which are used as scanning single-spin sensors with potential for high-resolution, high-sensitivity magnetic field imaging [55]. Recently this sensors reached a better resolution than 100 nm and field sensitivity down to 60 nT/ \sqrt{Hz} [56]. The possibility of operation at a variety of temperatures, including in ambient conditions, makes NV magnetometry attractive for a wide array of applications. Despite these advantages scanning NV magnetometry remains challenging at high fields due to the 28 GHz/T gyromagnetic ratio of the sensor electron spin. Improved resolution and sensitivity also appear to be limited by the difficulty of achieving NV centers with long spin-coherence times near the surface of the scanning tip. Furthermore, the required optical excitation poses a limit on the possible samples, since it strongly perturbs materials such as direct-band-gap semiconductors, nanomagnets, and fragile biological structures. Despite the rapid development of highly sensitive magnetic field probes, like for instance NV scanning probes [56], scanning SQUID's remain the most sensitive magnetic field probes.

1.3.1. Development of the SQUID-on-tip technique

Taking advantage of a SQUID's extreme sensitivity to magnetic flux, scanning SQUID microscopy (SSM) was first realized in the early 1980s. As imaging resolution has improved from

the micrometer- down into the nanometer-scale, a number of strategies have been employed to realize ever-smaller sensors, which simultaneously retain high magnetic flux sensitivity and can be scanned in close proximity to a sample. One strategy has involved miniaturizing the pick-up loop of a conventional SQUID and placing it at the extreme corner of the chip where it can come close to a sample. The most advanced of such devices uses a loop with a 200-nm inner diameter to achieve sub-micrometer imaging resolution and a sensitivity of $130 \text{ nT}/\sqrt{Hz}$ [33]. Although this design has the advantage of allowing for susceptibility measurements, the size of the sensor and minimum distance from the sample, which together determine the imaging resolution, are limited by the complex fabrication process.

The highest resolution and sensitivity have been achieved by a different solution: using nanometer-scale SQUID (nanoSQUID) sensors. Most nanoSQUIDs lie on the plane of a large substrate and are therefore complicated to apply as scanning sensors. Although there have been demonstrations of magnetic imaging by scanning samples in proximity to such SQUIDs, where the magnetic flux originating from an individual ferromagnetic Ni nanotube attached to a Si cantilever was measured [34]. The geometry of this used nanometer-scale SQUID was not amenable to a generally applicable microscopy. To solve this problem a design of the nanoSQUID is needed which allows to retain high magnetic flux sensitivity and can be scanned in close proximity to a sample. The Weizmann Institute introduced the SQUID-on-tip (SOT) design, in which a nanoSQUID is fabricated on the end of a pulled quartz tip [39]. The fabrication of such SOTs will be described in the following chapter 1.3.2. The SOT technique provides both a nanoSQUID having a high magnetic flux sensitivity at the end of the pulled quartz tip and a geometry that can be scanned in close proximity to a sample.

Working SOTs were first realized using Al as the superconducting material [39], however, the low critical temperature of Al prevented operation above 1.2 K. In addition, the large coherence length ξ and London penetration depth λ_L of the granular Al films precluded the realization of sensitive devices with dimensions below 100 nm. Later, better results were obtained with Nb and finally Pb [38], which allowed for higher operating temperatures and had both shorter ξ and λ_L . As a result, Nb and Pb SOTs could be made smaller than Al SOTs. Operating fields up to 1.2 T were realized for the Pb SOTs with 50 nm diameter, since all the characteristic lengths in the devices were on the order of ξ . Between the two materials, the Nb SOTs displayed a flux noise of $3.6 \mu\phi_0/\sqrt{Hz}$ compared to $50 \text{ n}\phi_0/\sqrt{Hz}$ for the Pb SOTs, which represents one of the lowest noise levels ever achieved [35–37]. The better performance of the Pb SOTs was likely due to the shorter ξ of the Nb SOTs.

Given the outstanding properties of the Pb SOTs, including 50-nm sensor-size, with sub-100 nm spatial resolution, a sensitivity of $5 \text{ nT}/\sqrt{Hz}$, and operation up to 7.2 K and 1.2 T, further experiments and development were carried out using this material. Technical refinements included SOTs with sensitivity to both in- and out-of-plane magnetic fields [41] and electrically tunable SOTs with uniform field sensitivity up to 0.5 T [42]. SSM with Pb SOTs has now been applied to probe dynamics and pinning of single superconducting vortices [43], to visualize superparamagnetic dynamics in topological insulators [44], and to observe emergent nanoscale superparamagnetism at oxide interfaces [45]. In addition, scanning thermal sensing based on Pb SOTs with 50 nm spatial resolution and $1\mu\text{K}/\sqrt{Hz}$ sensitivity was demonstrated [40]. This represents a sensitivity, which is four orders of magnitude better than other devices, and has already enabled the observation of dissipation due to individual quantum dots in carbon nanotubes and resonant localized states in graphene. Such sensitive thermal microscopy is possible only because of the suitable SOT geometry, which uses a nanoSQUID as the scanning probe rather than a miniaturized pick-up loop coupled to a conventional SQUID. Despite all of

the advantages of scanning SOT devices, their resolution, sensitivity, and ease of use are still limited by technical challenges. The most important limitation of the technique, however, has to do with poor control of the vertical tip-sample separation and the challenge of navigating on an arbitrary sample.

1.3.2. Fabrication of a SQUID-on-tip sensor

The first step in the fabrication of a SQUID-on-tip (SOT) sensor includes the fabrication of a hollow quartz tip, which possesses the right geometrical shape after the pulling. This contains, for instance, the length, aspect ratios, and diameter of the tip. A commercial Laser-Based Micropipette Puller (Sutter Instrument P-2000) is used, which allows to tune the geometrical shape of the pulled quartz tube. The geometrical shape of such a pulled quartz tube depends on a number of factors. The quartz tube pulling process is carried out in two steps, giving a pair of sharp pipettes with diameter in the range from 80 to 400 nm. The settings which play an important role in both steps are, for instance, the laser heating, the pulling force, or the delay time during the pulling process. After pulling, gold (Au) contacts are needed on two sides of the cylindrical base of the pipette.

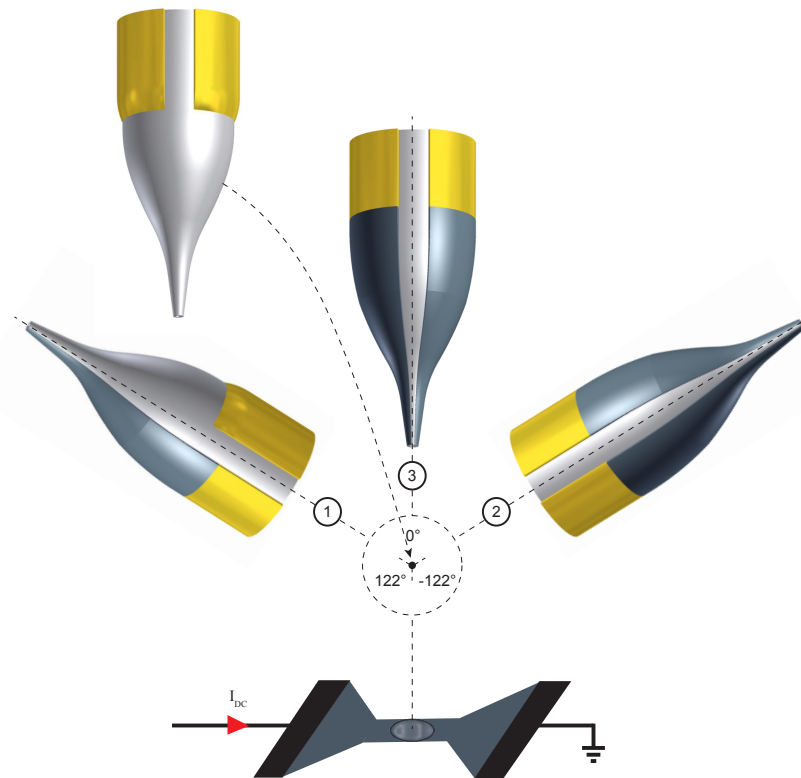


Figure 1.6. | Schematic of the three-stage thermal evaporation to obtain a SQUID-on-tip sensor on a sharp pulled pipette. After the pulling and the Au deposition of the two electrodes the pipette is mounted in the home-built thermal evaporation system. The three-stage Pb evaporation under three different angles with respect to the Pb source, is labeled in chronological order from ① - ③.

We deposit for the contacts 150 nm of Au through masks along the cylindrical pipette, opposite each other. The masks prevent overlap between the two Au contacts as well as the Au deposition on the tapered part of the pipette. Afterwards, the pipette is mounted on a rotatable cold finger which fits into the home-built thermal evaporation system and allows us to rotate the pipette around a horizontal axis in-situ. Furthermore, is kept at 4.2 K during the entire Pb evaporation process through a continuous flow of liquid helium. This continuous flow of liquid helium is important, because the Pb atoms have a high surface mobility which results in island growth. To get a smooth superconducting thin film, one has to cool the pipette during deposition. The home-built thermal evaporation system allows us to reach ultra-high vacuum (UHV) conditions with a base pressure of 1.5×10^{-7} mbar and a pressure during deposition of 8.0×10^{-7} mbar. Between the three-stage thermal evaporation, the system allows us to introduce ^4He gas into the chamber at 1.0×10^{-5} mbar to facilitate pipette cooling. After one minute the gas is pumped out to reach again base pressure. Figure 1.6 shows the schematic of the three-stage thermal evaporation of a SOT.

After mounting the pipette in the home-built thermal evaporation system we deposit the first electrode. To do that, the pipette is rotated by 122° with respect to the position of the Pb source which is defined as 0° . In general, angles larger than 90° prevent shorting of the two leads. Then 200 \AA of Pb is deposited, labeled with ① in figure 1.6. The deposition rate is in all evaporations $\sim 3.5 \text{ \AA s}^{-1}$. The thin superconducting film overlaps the Au contact on one side and ends at the end of the apex on the other side. After cooling, deposition is performed at an angle of -122° relative to the Pb source on the opposite side of the pipette, which builds the second electrode, labeled with ② in figure 1.6. For the second electrode the same amount of Pb is evaporated. Subsequently, the pipette is rotated so that the apex points towards the Pb source, i. e. an angle of 0° . Then 120 \AA of Pb is deposited on the apex to obtain the superconducting loop of the SQUID at the end of the apex, which overlaps the two leads on both sides, labeled with ③ in figure 1.6. In the overlapping regions stronger, superconductivity is reached, while the short parts of the loop next to the gap of the leads act as two Dayem-bridge weak links, thus forming a planar SQUID at the end of the pipette, which is therefore called SQUID-on-tip. The SOTs are extremely sensitive to electrostatic discharge because of their small size. For this reason the devices are shorted at all the times and opened only after mounting them in the microscope.

1.3.3. Characterization of a SQUID-on-tip sensor

After the three-stage thermal evaporation the devices have to be characterized to see if they show the characteristic interference pattern of a working SQUID. For this, the device has to be transferred into a test system. The test system should therefore reach a temperature lower than the critical temperature of Pb (about $T_c = 7.2$ K) and further it should be able to apply a magnetic field in z -direction. The test system consists of a test probe including a temperature sensor as well as a heater, which allows to heat up the local region around the mounted device. The test probe is built such that it fits into the opening neck of a liquid helium dewar. The dewar contains a superconducting solenoid which allows to apply magnetic fields up to ± 2.5 T along the z -axis. During the transfer, the SOTs are exposed to air at normal pressure and temperature for 20 minutes. After mounting the SOT in the test probe the device has to be un-shorted. A potentiometer is connected as protection against electrostatic discharge at the output of the test probe, which allows to switch the device output between shorted and open. The device should be shorted during pumping and cool down. Pumping the test probe is very important to prevent excessive oxidation of the SOT weak links, which can lead, in the worst case, to resistive devices. A resistive SOT has no more sensitivity to magnetic stray field and is therefore no longer usable for measurements.

After cooling the test probe to the base temperature of $T = 4.2$ K, one has to connect the SOT output with a constant DC voltage source (Yogogawa 7651), which allows to apply an input voltage (V_{bias}). For the read out of the current which flows through the SOT (I_{SOT}) a series SQUID array amplifier (SSAA) is used as a cryogenic current-to-voltage converter. A simplified measurement circuit is shown in Figure 1.7. An input voltage (V_{bias}) applies current to the SOT in series with a cold resistor (R_{bias}) of 6.5 k Ω , which is shunted by a resistor (R_{shunt}) of 3 Ω . Further in series there is a parasitic resistance ($R_{parasitic}$) of a few ohms, which is mainly due to the wiring and the Au contacts at the base of the pipette. The SSAA is inductively coupled through a nominal input inductance L_{IN} of 6 nH, to the SOT circuit and is operated in a closed-feedback loop. The current flowing through the SOT is measured proportional to the voltage drop over a feedback resistor (R_{FB}).

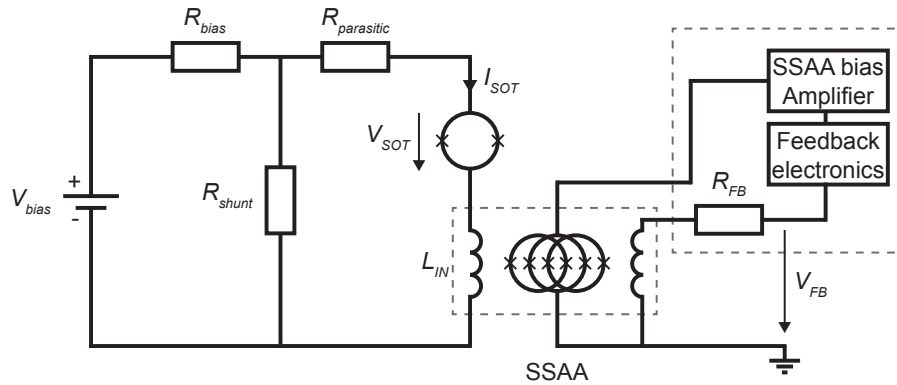


Figure 1.7. | Simplified SQUID-on-tip (SOT) measurement circuit showing on the left side the SOT circuit and on the right side the closed-feedback loop.

To characterize the SOT, an external magnetic field is applied and kept at a fixed strength. Further the input voltage is swept up and down while measuring simultaneously the voltage

drop across R_{FB} . If the SQUID is working, the measured I_{SOT} vs V_{bias} - curve should show two characteristic behaviors. At low V_{bias} the SOT is in the superconducting state, where all of the current is flowing through the SOT. The I_{SOT} vs V_{bias} characteristics is linear in this area with a slope corresponding to the cold bias resistance of $6.5k\Omega$ plus the parasitic resistance of a few ohms. The current flowing through the SOT is given by $I_{SOT} = V_{bias} \cdot (R_{shunt}/R_{bias})/(R_{parasitic}+R_{shunt})$. At some point the critical current I_c of the SOT is reached which marks the transition between the superconducting state and the resistive state. In the resistive state a big fraction of current is flowing through R_{shunt} and less current through the SOT, which leads to a much lower slope in the second area compared to the superconducting state. Figure 1.8 shows the typical characteristic quantum oscillations in a) of a series of measurements for applied magnetic fields between ± 0.8 T and in b) the derivative shows the magnetic response of the SQUID $\Delta I_{SOT}/\Delta B$ and therefore showing the regions where the SOT is highly sensitive to the external applied magnetic field. At higher magnetic fields the I_c gets lower in magnitude, until it is completely suppressed around ± 1.2 T, showing then just a resistive response with no transition. The effective SOT diameter can be calculated from the period of the interference pattern using equation 1.7. Where B_{period} is the magnetic field range of a full period and ϕ_0 is the magnetic flux quantum.

$$d_{tip} = 2 \cdot \sqrt{\frac{\phi_0}{B_{period} \cdot \pi}} \quad (1.7)$$

The SOT shown in Figure 1.8 has a calculated effective diameter of 200 nm. As a general rule the larger the period of the interference pattern, the smaller the effective diameter of the SOT.

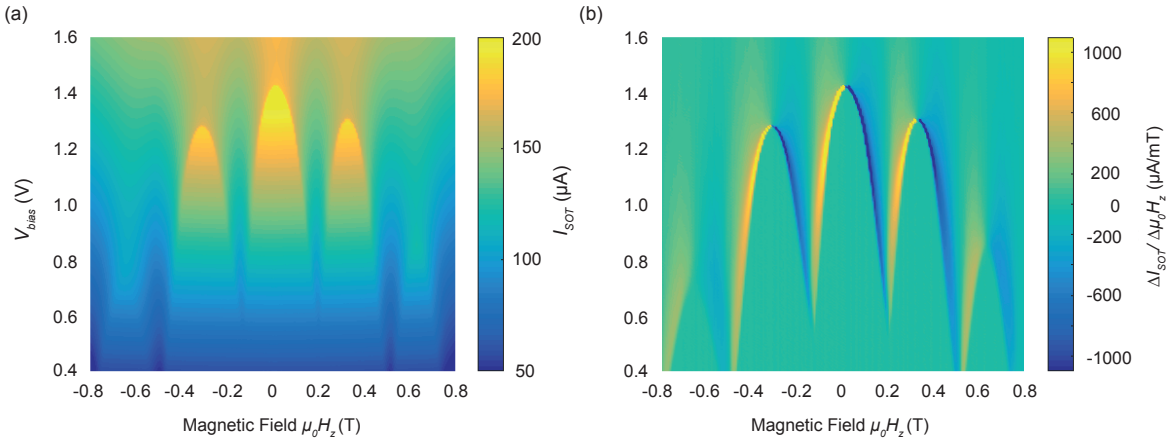


Figure 1.8. | (a) Current through the Pb SQUID-on-tip (colour coded) versus input voltage V_{bias} and applied magnetic field ($\mu_0 H_z$) showing quantum interference oscillations with a period corresponding to an effective SOT diameter of 200 nm. (b) Flux-to-voltage SQUID transfer function showing the most sensitive regions. The sensitivity is zero at the minimum and maximum.

SOTs are not only extremely sensitive to the local magnetic stray field component pointing in z -direction [39], but they are also extremely sensitive to the local temperature arising from a sample underneath [40]. To measure the temperature dependence of the SOT, which allows to determine afterward the thermal sensitivity of the device, a heater is mounted in the test probe. The heater allows to increase in steps homogeneously the local temperature of the brass piece surrounding the mounted SOT.

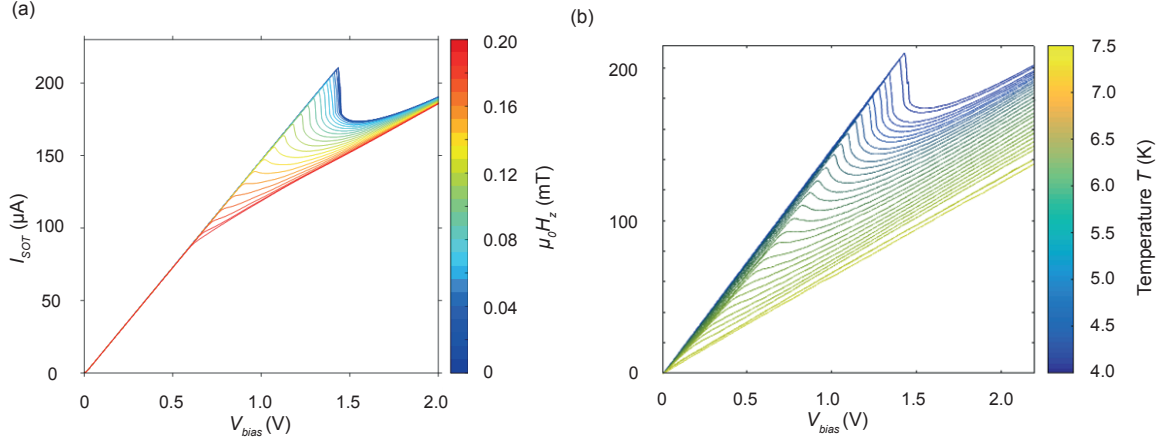


Figure 1.9. | (a) Magnetic field (colour coded) versus current through the Pb SQUID-on-tip and input voltage V_{bias} showing half a period of the interference pattern from figure 1.8 (a). The most sensitive region is located close to the transition between the superconducting and resistive state. (b) Temperature dependence of the SOT showing the temperature (colour coded) versus current through the Pb SQUID-on-tip and input voltage V_{bias} .

At 4.2 K starting from a typical I_{SOT} vs V_{bias} characteristics, the local temperature increase leads to a shift of the critical current in both the amplitude and the applied bias to lower values, till above the critical temperature of Pb, the superconductivity is completely suppressed, showing a linear response as shown in figure 1.9 b). In the resistive region above the critical current the change is linear. If we fit a linear function to the values at a fixed bias and different temperatures a thermal sensitivity of $26.1 \mu\text{A}/\text{K}$ is obtained for the above described sensor. The worse thermal sensitivity compared to the shown $1\mu\text{K}/\sqrt{\text{Hz}}$ by Halbertal et. al. [40], can be explained by the larger effective SOT diameter. In our case the effective SOT diameter is 200 nm compared to 50 nm by Halbertal et. al. [40]. Thermal imaging requires a certain amount of exchange gas in the sample chamber, so that a thermal coupling between scanning SOT and the sample is ensured. In principle for thermal imaging no SQUID is necessary; a single Josephson junction is enough to gain thermal sensitivity.

1.3.4. Scanning SQUID Microscopy

When the SQUID-on-tip (SOT) has been successfully characterized in the test probe, as previously described in chapter 1.3.3 and it has the desired properties for a planned experiment one has to mount it safely and quickly into the microscope. This process includes some steps and should always be carried out with maximum concentration to prevent the device from being destroyed. After fixing the SOT-holder on top, the sensor has to be positioned roughly above the sample mounted on top of a piezo-based nanopositioner, under the use of an optical light microscope. Using the z -positioner, the sample is brought manually close to the SOT. At some point the reflection from the tip on top of the Si-substrate is visible and thereby the roughly landing position of the apex. The SOT is then be positioned in x - and y -direction above the sample of interest with an accuracy in the order of $\pm 10 \mu\text{m}$. Once positioned the short has to be opened to have the opportunity to apply a bias voltage to the SOT after the cool down. Before starting the cool down one has to pump the microscope down to 1.0×10^{-5} mbar before starting the pre-cooling using liquid nitrogen. When a temperature of 110 K has been reached, the microscope can be transferred to the liquid helium bath cryostat. To reach the 4.2 K quickly one can use one shot of helium gas as an exchange gas. It turns out that the exchange gas leads to a higher signal-to-noise-ratio; for this reason the gas has been pumped out after cool down for all measurement presented in this thesis.

The microscope consists of two parts: on the bottom, the sample is mounted on top of a commercial piezo-based nanopositioner (attocube) including xyz -positioners and a xy -scanner; on top, the tip is mounted in the pendulum geometry at a fixed position. To approach the sample within a few nanometers and to keep the achieved distance after, one needs to properly isolate the system from its surroundings, this is mainly meant from vibrational as well as acoustic and electrical noises. For vibration isolation we placed the dewar on a heavy optical sealed hole table top (Newport RP Reliance). The table was placed on three commercial isolators (Newport S-2000). These isolators attenuate vibrations from the environment at low frequencies, having already a 30 dB attenuation at 10 Hz, with a typical disadvantage of amplification around the resonance of 1 Hz. To reduce acoustic noise, we covered the dewar with heavy Pb strips to damp the noise modes of the dewar.

SOTs are completely blind to topography and thus rely on stray magnetic fields – or thermal gradients – to judge the distance from a sample surface. Given that even the slightest contact with the sample can destroy a SOT, this vulnerability significantly limits the minimum tip-sample working distance to a safe margin, typically well over 100 nm. This large tip-sample separation, in turn, limits both the resolution and sensitivity of the resulting magnetic image. It also puts strong requirements on the flatness of the sample and the lateral scanning range due to unavoidable sample tilt. Together, all of these factors make the SOT technique difficult to perform.

To approach with the SOT in the microscope into close proximity to the sample, the SOT has to be operated in the FFL mode and locked at the working point with the highest voltage-to-flux ratio. On a big enough magnetic sample a direct approach on the DC magnetic signal along the z -axis B_{DC} is possible. This kind of approach was used to bring the apex of the tip in close proximity to the chiral spin ice system, these measurements are described more in detail in chapter 5. If no magnetic structure is present, or the magnetic structure is too small to align the SOT above it, one needs for instance current-carrying nanowires on top of the substrate surrounding the sample of interest, which allows to approach on the AC magnetic field amplitude along the z -axis B_{AC} and later to move towards the region of interest. While

the bottom piezo-based nanopositioner is moving in z -direction, to the set voltage, the x -scanner moves simultaneously to some extent. With this approaching scheme we increase the possibility to catch up some flux while moving. If the set threshold is not reached, the sample moves a step closer towards the SOT and the whole process is repeated until the set threshold is reached. This is the case when enough flux is coupled into the SOT coming from the stray-field of a magnetic structure (B_{DC}) or a current-carrying nanowire underneath (B_{AC}). Depending on the sample and its specific stray magnetic field distribution, it is then necessary to bring the SOT even closer. Figure 1.10 shows the three detectable signals using a scanning SOT. The AC magnetic field amplitude B_{AC} in (b) as well as the AC temperature change ΔT_{AC} in (c) are signals coming from a current-carrying wire underneath the SOT. In this two types of images a close to the Au wire placed out of the page magnetized ferromagnetic nanotube is not visible. To map the DC magnetic field, the current flow through the Au wire is interrupted to prevent that some spurious signal ΔT_{AC} can leak into the B_{DC} image. In (d) the DC magnetic signal along the z -axis of the out of the page magnetized ferromagnetic nanotube is shown. The AC magnetic field amplitude produced by the wire could be determined with a simulated Biot-Savart field of a current-carrying nanowire as shown in (a). The magnetic field strength from the experimental data could be compared with the simulations and allows to determine the distance between the sample and the SOT. The distance between the SOT and the ferromagnetic nanotube was determined to be ~ 300 nm.

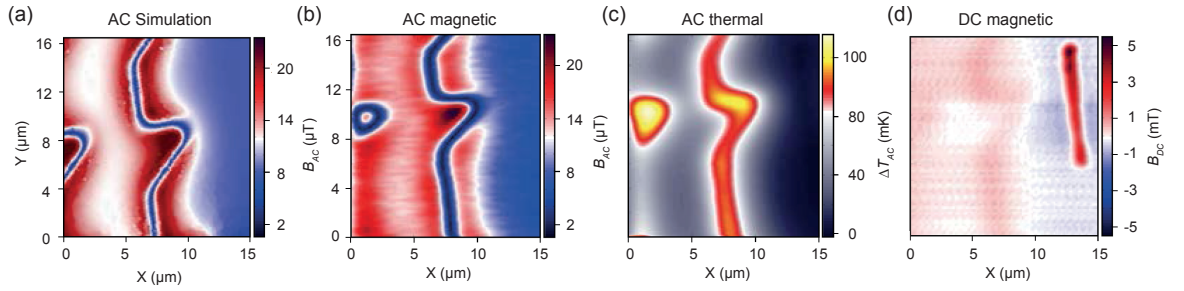


Figure 1.10. | (a) Simulation of the AC magnetic field amplitude along the z -axis B_{AC} produced by the current flowing through the Au wire; corresponding measurements of the AC magnetic field amplitude B_{AC} in (b), (c) the AC temperature change ΔT_{AC} due to I_{AC} , and (d) the DC magnetic field along the z -axis B_{DC} , recorded by the SOT above the area where close to the Au wire an out of the page magnetized ferromagnetic nanotube was located. To map the DC magnetic field the current flow through the Au wire is interrupted to prevent that some spurious signal ΔT_{AC} can leak into the B_{DC} image.

A SQUID is by definition a low impedance device. Usually the electronics used to read-out at room-temperature are optimized for high impedances. This impedance mismatch results in a decrease in the signal-to-noise ratio. There are different possible ways to overcome this circumstance like for instance use a non-dispersive read-out method [57], in this work we choose to use a SQUID series array amplifier, which is essentially an array of 100 SQUIDSs connected in series, if properly cooled down they are phase-coherent [53]. The current through the SOT passes a line which is inductively coupled to this array, as previous shown in figure 1.7. The change in flux through them changes their critical current and simultaneously the output voltage. To keep the working point of the SQUIDSs at the most sensitive region, that is where the flux-voltage modulation is the most linear, a flux-locked feedback loop (FLL) is used. The SSAA has two functions, first it is a flux-to-voltage converter and second because the current is inductively coupled at very low temperatures it is a low-impedance current-to-

voltage converter. The room-temperature feedback box is bandwidth limited to 6 MHz, which means that we cannot measure signals at frequencies higher than 3 MHz. Our system noise limit is set by the SSAA current noise density which is $2.6 \text{ pA}/\sqrt{\text{Hz}}$. The feedback box has the option to use a second order Bessel type anti-aliasing filter with a cutoff frequency set to 10 kHz.

1.4. Comparison of the introduced magnetic imaging techniques

Both previous presented magnetic imaging techniques have their specific advantages as well as disadvantages. If we first look at which temperatures both techniques could operate, a big difference is coming from the fact that for the SOT a superconducting material is used, which define the limits of the operation temperature. In this work Pb is used as a superconducting material, so the upper limit is set by the critical temperature given by 7.2 K and the lower limit by the used cryogenic device. Using a helium bath cryostat filled up with Helium-4 a temperature of 4.2 K, or in combination with a dilution fridge 300 mK can be reached. The PEEM operates usually at ambient temperature but there is a possibility to cool the endstation with liquid nitrogen to about 120 K at the SIM beamline [8].

The spatial resolution in the case of the SOT is given by the effective tip diameter, the record reported so far by Vasyukov et al. [38] was 56 nm. In this work the effective diameter of the used SOT was calculated from the interference pattern to be 148 nm. In the PEEM it is much more complicated to reach a high spatial resolution, because it depends on a lot of factors starting from the sample roughness, acceleration voltage, all the optical lenses and there settings, the chromatic (electrons with different speed) and spherical aberrations (electrons at different angle), the mechanical drift during image acquisition, which all leads to a blurring of the image. The typical spatial resolution of the SIM beamline is about 50 nm [8]. In this work the spatial resolution of the presented PEEM measurements was with 100 nm a little worse, compared to the typical value. This can be explained by the non-flat sample, because around topographic features the accelerating field is curved. This results in a general degradation in spatial resolution and local focusing.

With the scanning SOT mounted in pendulum geometry one is sensitive to the stray field component pointing in \hat{e}_z -direction above the sample of interest. PEEM is an element selective imaging technique which probes in total electron yield measurements (TEY) a few nanometers deep the local magnetization of a sample pointing parallel or anti-parallel towards the propagation direction of the x-rays.

One of the most important disadvantages of PEEM is that emitted secondary electrons from the sample are imaged. Secondary electrons interact strongly with an external magnetic field, because of the negative charge and the resulting Lorentz forces. Already very tiny external applied in-plane magnetic fields changes the trajectories of the secondary electrons due to interaction of the negative charge with the magnetic field, which leads to a distortion of the image. But a crucial point in magnetic imaging is the application of magnetic fields during imaging. At the BESSY II synchrotron in Berlin, Germany, Kronast et. al. developed a spin-resolved photoelectron emission microscope (S-PEEM). With this setup they were able to apply magnetic fields up to $\pm 33 \text{ mT}$ without significant distortion or reduction of the lateral resolution of the S-PEEM [10]. For the SIM beamline, we developed a similar PEEM sample holder as shown in Appendix A.1. With this novel PEEM sample holder a magnetic field of $\pm 40 \text{ mT}$ could be applied to the sample space. It turned out that the gap between the pole

pieces were in the range where deflections of secondary electrons could not be reduced enough. For this reason only magnetic states at zero applied magnetic field can be imaged using the PEEM at the SIM beamline. The nanoscale superconducting ring with the two weak links in the form of Dayem bridges in the gap regions between the leads at the end of the apex of the SOT enables that the superconductivity in this device is only suppressed at impressive ± 1.2 T if the magnetic field is pointing perpendicular to the superconducting ring in \hat{e}_z -direction and up to ± 0.4 T if the magnetic field is pointing parallel to the ring in \hat{e}_x -direction. Compared to conventional SQUIDs both values are rather high, especially in \hat{e}_z -direction. The reason is that the SOT consists of two nanometric Dayem bridges. The small dimension of the bridges leads to such impressive high critical fields.

Another important physical quantity is the time which is needed to get magnetic images, which have the appropriate quality. In the case of PEEM the time needed is mainly depending on the number of images taken using x-rays with opposite helicity σ^+ and σ^- , which allows to obtain the characteristic PEEM image. To get a sequence of PEEM images the time required is often in the range of few minutes. For measurements taken with scanning SOT it mainly depends on the amount of data points used in x - and y -direction and is usually several minutes.

In summary both imaging techniques have their outstanding advantages. Direct measurements of magnetization, as PEEM does, are especially attractive for the investigation of magnetic domains and spin textures, because magnetization configurations cannot be uniquely deduced from stray field measurements alone. On the other hand, the generality of stray field measurements makes SOTs applicable to a wider set of phenomena than magnetization measurements, with the lack of the low temperature range. Stray fields are produced not only by magnetization patterns, but also by current distributions. Furthermore, target samples span across conductors, insulators, and soft biological matter; the only requirement is that they produce a magnetic field.

Physical quantities	PEEM	SQUID-on-tip
Operation temperature	120 K [8] - ambient temperature	300 mK - 7.2 K (Pb)
Spatial resolution	~ 100 nm, record 5.4 nm [17]	~ 150 nm, record 56 nm [38]
Magnetic Field ($\mu_0 H_{\text{ex}}$)	zero	1.2 T \hat{e}_z , 0.25 T \hat{e}_x
Sensitive to	surface net magnetization	stray field component in \hat{e}_z
Acquisition time	few minutes	several minutes

Table 1.1. | Comparison of the relevant technical data of PEEM vs SQUID-on-tip technique.

2. Ferromagnetic Nanotubes

This chapter provides a brief introduction into how tubular shaped ferromagnetic nanotubes are fabricated and how the magnetization behaves depending on the length and diameter of such a three-dimensional architecture. Furthermore, I would like to show possible future applications in modern information technology in relation to the dimension and the magnetic properties of such tubular shaped ferromagnetic nanotubes.

2.1. Introduction

Since the development of the first modern computer a functional digital computer in 1941 by Konrad Zuse in cooperation with Helmut Schreyer, the data storage as well as the rapid access to it plays a key role for modern information technology. In the last decades scientists all over the world put a lot of effort to find ways to steadily reduce the area of a magnetic bit in size towards the fundamental limitation. That led over the past 50 years to a decrease of the area in size by about around nine orders of magnitude [66]. A prominent example which fulfilled the requirements over the last decades is the magnetic hard disc drives but the device face now limitations, because a purely mechanical guidance is no longer possible with a higher track density. An interesting alternative proposed by Stuart Parkin ten years ago is the so-called racetrack memory [67]. The racetrack memory consists of a ferromagnetic nanowire in which a pattern of domains as bits with opposite directions separated by domain walls are located along a portion of the wire. The domains can be moved by an electrical current, while moving the bits, they could be written or read. This memory device gives promise with the performance and reliability of conventional solid-state memory but at the low cost of conventional magnetic disk drive storage. Another approach to obtain dense magnetic storage technologies is the engineering of magnetic elements with both well-defined remnant states and reproducible reversal processes. Nanometer-scale magnets have intrinsically large surface-to-volume ratios, making their magnetization configurations especially susceptible to roughness and exterior imperfections. Furthermore, poor control of surface and edge domains can lead to complicated switching processes that are slow and not reproducible [68, 69]. To address these challenges one approach is to use nanomagnets that support remnant flux-closure configurations. The three dimensionality of the nanomagnets and the resulting absence of magnetic charge at the surface reduce its role in determining the magnetic state and can yield stable remnant configurations with both fast and reproducible reversal processes. In addition, the lack of stray field produced by flux-closure configurations suppresses interactions between nearby nanomagnets. Although the stability of such configurations requires dimensions significantly larger than the dipolar exchange length, the absence of dipolar interactions favors closely packed elements and thus high-density arrays [90].

Here, the study of magnetic nanostructures enter the game and is motivated by their potential as elements in dense magnetic memories, in networks used to perform logic operations [70], magnetic sensors [71], and as probes in high-resolution imaging applications [72–74]. For these reasons, a number of nanometer-scale geometries have been investigated both theoretically

and experimentally, including magnetic dots, rings, wires, and tubes. Of particular interest are nanomagnets with stable flux-closure magnetization configurations and both fast and reproducible reversal processes. In the context of magnetic memory, speed and reliability are determined by the latter, while ultimate density can be enhanced by the former. Although flux-closure configurations require dimensions significantly larger than the dipolar exchange length, they favor high density, because they produce minimal stray fields, thereby minimizing interactions between nearby memory elements [90]. Ferromagnetic nanotubes (FNT) are a particularly promising morphology, given their lack of a magnetic core. At equilibrium, the hollow magnetic geometry is expected to stabilize vortex-like flux-closure configurations with magnetization pointing along the FNT circumference. Although vortex ends states have been observed in ferromagnetic nanowires (NWs) [91], the exchange energy penalty for the magnetic singularity along the vortex axis tends to favor non-flux closure states. In a FNT, the lack of this axial Bloch point structure [92] is also expected to allow for fast magnetization reversal that begins with vortices nucleating at its ends and propagating along its length [75, 93, 95]. Due to their tubular geometry, FNT may reveal curvature-induced effects [98, 99], such as asymmetric spin-wave dispersion [100] or Cherenkov-type emission of magnons by certain types of domain walls [101].

The dependence of the FNTs equilibrium magnetization configuration on geometry, as well as details such as the relative sense of circulation of the end-vortices, has been recently considered both analytically and numerically [80–82]. In particular, it has been predicted that the global vortex state can be programmed as the stable remnant configuration by a small NT length-to-diameter ratio. Experimental evidence for vortex configurations in FNTs has so far been limited to magnetic force microscopy images of single NTs reported by Li et al. [83]. There, the authors interpret a nearly vanishing MFM contrast and a small remnant magnetization as an indication of a global vortex state. Magnetotransport [84] and dynamic cantilever magnetometry (DCM) [85] of Ni NTs suggest the presence of vortex configurations; however, the considerable roughness of these NTs likely makes them different enough from idealized ferromagnetic NTs to affect their equilibrium configurations. Magnetization configurations in rolled-up ferromagnetic membranes between 2 and 16 μm in diameter have been imaged using magneto-optical Kerr effect [86], x-ray transmission microscopy [86], x-ray magnetic dichroism photoemission electron microscopy (XMCD-PEEM) [87], and magnetic soft x-ray tomography [88].

2.2. Fabrication of ferromagnetic nanotubes

In the following the fabrication of the ferromagnetic nanotubes (FNT), used in this thesis, will be described. Several fabrication methods for magnetic nanotubes are known, for example, hydrogen reduction [102], electrodeposition [103] and atomic layer deposition (ALD) into porous membranes [76], to name the most important. The ferromagnetic nanotubes measured in this thesis were fabricated using a completely different method. Here, the FNTs are made by depositing a thin magnetic film on non-magnetic GaAs nanowires (NWs) having hexagonal cross-sections and acting as templates. These non-magnetic GaAs NWs are grown by molecular beam epitaxy on a Si (111) substrate using Ga droplets as catalysts [58]. Two ferromagnetic alloys are then deposited on top of the GaAs template to form the ferromagnetic nanotubes. The deposited ferromagnetic alloys consist of Cobalt-Iron-Boron ($\text{Co}_{20}\text{Fe}_{60}\text{B}_{20}$) or Permalloy ($\text{Ni}_{80}\text{Fe}_{20}$) also called Py. For the CoFeB nanotubes, CoFeB is magnetron-sputtered on the

NWs, producing an amorphous and homogeneous 30 ± 2 nm thick shell [59]. For the Py nanotubes, a 30 ± 2 nm thick polycrystalline shell of Py is deposited by thermal evaporation [64]. During both depositions, the wafers of upright and well-separated GaAs NWs are mounted with a 35° angle between the long axis of the NWs and the deposition direction. The wafers are then continuously rotated to achieve a conformal coating. Figure 2.1 (a) shows an image of the general structure of the investigated nanotubes consisting of the before mentioned GaAs core (dyed gray) surrounded by a ferromagnetic shell out of CoFeB or Py (dyed blue). At the upper end, a Ga droplet is visible. The resulting FNT had lengths between 10 and 20 μm and outer diameters of 150 to 400 nm [97].

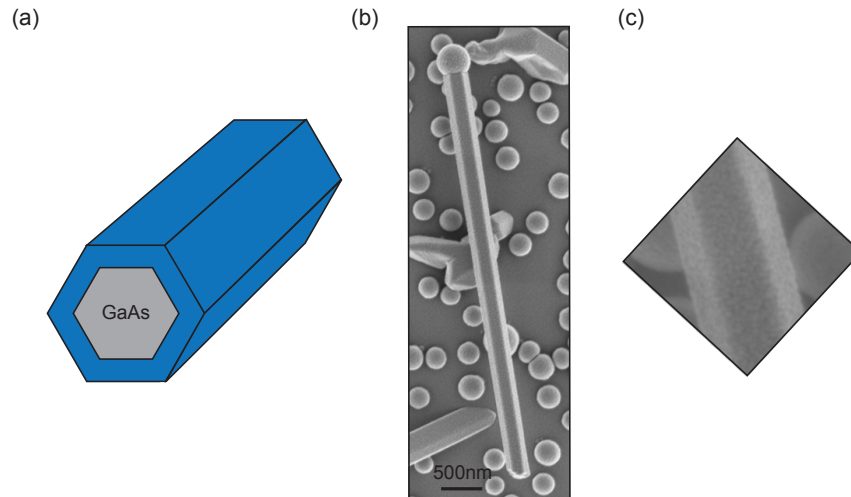


Figure 2.1. | (a) Image of the general structure of a nanotube investigated consisting of a non-magnetic GaAs core (gray) and a ferromagnetic shell (blue) with a hexagonal cross-section. (b) SEM image of a CoFeB NT from the same batch used in this thesis, showing nicely the hexagonal structure. At the upper end, a Ga droplet is visible. (c), Shows a bigger view of the CoFeB NT surface, which is free of detectable defects and whose roughness is less than 5 nm.

The fabrication process and choice of materials avoids magneto-crystalline anisotropy [58, 104, 105], although recent magnetotransport experiments suggest that a growth-induced magnetic anisotropy may be present in the CoFeB NTs [106]. Previous dynamic cantilever magnetometry (DCM) measurements of FNT from the same growth wafers as used for this thesis provide $\mu_0 M_s = 1.3 \pm 0.1$ T and 0.8 ± 0.1 T for the CoFeB [59] and Py NTs [64], respectively, where μ_0 is the permeability of free space. The magnetic shell material is covered by a few-nanometer-thick native oxide, which affects the NT magnetization only at cryogenic temperatures through antiferromagnetic exchange coupling. We observed such coupling below a blocking temperature of 18 K in Py NTs [64]. Further we investigated the nature of the native oxide layer using spatially resolved x-ray absorption spectroscopy (XAS) by means of x-ray photo-emission electron microscopy (PEEM). PEEM provides a spatial map of the local x-ray absorption cross section. From the recorded x-ray absorption spectra taken at different positions on top of the CoFeB and Py NTs, after the superposition with reference data it turned out that the native oxide layer of CoFeB and Py NTs mainly consists of FeO, $\alpha\text{-Fe}_2\text{O}_3$ and NiO. The overall thickness of the oxide layer was estimated to be in the range of 2 - 5 nm [64, 65].

2.3. Equilibrium states in ferromagnetic nanotubes

To understand the fundamental physics that govern magnetic behavior in individual ferromagnetic nanotubes, the effects of tubular geometry plays an essential role on the possible equilibrium magnetic configurations of them. Two main equilibrium states has been identified experimental by magnetic measurements [76] or theoretical by numerical simulations [77] and analytical calculations [78, 79]. Namely, an axial state where the magnetic moments uniformly pointing parallel to the long axes of the tube as depicted in figure 2.2 (a). The parallel alignment minimizes the gradient in magnetization at the cost of dipolar energy due to the stray field at the ends [97]. Further a flux-closure vortex state depicted in (c), in which the magnetization points circumferentially around the tube axis. Between those two magnetic configurations, which are uniform over the entire length of the ferromagnetic nanotubes, micro-magnetic simulations have demonstrated the existence of a mixed state [77, 80, 89]. A mixed state is a mixture of the axial and vortex state. In the middle region, the magnetization is pointing uniformly towards the long axes like in the axial state, whereas near the tube ends curling states of various circular polarities occur [75] as depicted in 2.2 (b).

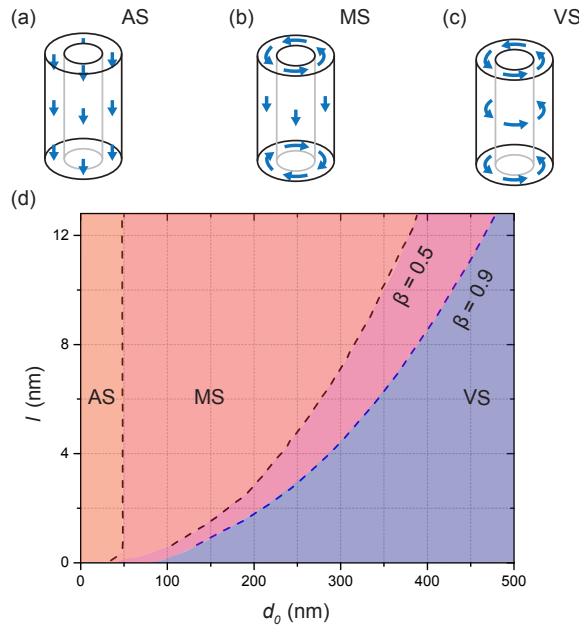


Figure 2.2. | Possible equilibrium magnetic states are illustrated: (a) axial state (AS), (b) mixed state (MS) and in (c) vortex state (VS). Magnetic phase diagrams for the transition from axial (AS) to mixed (MS) and finally vortex (VS) state as a function of the outer diameter d_0 and tube length l . The thin dashed lines depicts the transition between AS and V, which splits into two lines corresponding to the transition AS - MS and MS - V. The MS - V transition is shown for two different shape factors $\beta = 0.5$ and $\beta = 0.9$ adapted from [75].

This magnetization deviation from the uniformity is most likely an incomplete vortex domain wall structure [80, 89] and minimizes the stray- as well as the dipolar fields. Which of these dominates depends on the specific geometry of the nanotube and what magnetic material it consists of. The phenomenology of nucleation and subsequent reversal process of the magnetization is closely related to the existence of the mixed state [95]. In summary, one can say that long and thin nanotubes will have an axial alignment as equilibrium configuration and thick and short nanotubes a vortex state. A vortex state owes their stability to the minimization

of magnetostatic energy at the expense of exchange energy [94]. Nanotubes are geometrically characterized by their outer d_0 and inner d_1 diameter and their length l . The ratio of this two diameters is called the topological form factor and is defined as $\beta = d_1/d_0$, so that $\beta = 0$ represents a solid cylinder and $\beta = 1$ corresponds to a very narrow tube [95].

Figure 2.2 (d) shows the analytical calculated magnetic phase diagram for the transition from axial (AS) to mixed (MS) and finally vortex (VS) state as function of the outer diameter d_0 and the tube length l . A tube which has a small diameter, which means less than $d_0 < 50$ nm, the assumed equilibrium state will be the AS, where all magnetic moments pointing towards the long axes of the tube. The length of the tube plays thereby no role. Two different shape factors are depicted by thin dashed lines, namely $\beta = 0.5$ and $\beta = 0.9$. They show the influence of the topological form factor on the MS - V transition. A higher β increases the MS region and shifts the transition to higher outer diameters. A topological form factor of $\beta = 0.9$ stands for a difference about 30 nm between inner and outer diameter and corresponds approximately to the thickness of the measured FNT in this thesis without taking into account the few-nanometer-thick native oxide layer surrounding them.

2.4. Sample Preparation for the XMCD-PEEM experiments

The magnetic behavior of individual ferromagnetic nanotubes can be manipulated by means of ion irradiation. To obtain specific lengths and well-defined ends, nanotubes were cut into segments by local irradiation with a 30 kV focused ion beam (FIB) under the use of gallium-ions (Ga^+). FIB has the advantage that it gives the opportunity to cut the FNT into well-defined lengths. The disadvantage is that the Ga-ions damage the surface locally in the irradiated area, further the cut leads to geometrical imperfections, such as slanted rather than flat ends.

After cutting, we use an optical microscope (Nikon Eclipse FN1), equipped with hydraulic precision micromanipulators (Narishige MMO-202ND) sitting on an optical table to reduce vibrations during the sample fabrication process, to pick up the NT segments and align them horizontally onto a Si substrate as shown in the optical microscope image in figure 2.3. 19 CoFeB NTs and 25 Permalloy (Py) nanotubes were placed using this manipulation method. SEM images reveal continuous surfaces, which are free of detectable defects and whose roughness is less than 5 nm, as shown previous in figure 2.1 (c). As an example two SEM images of two individual FNT with different lengths are shown. Clearly visible are the slanted ends as a result of the FIB cutting process, especially visible on the shorter nanotube. In Appendix A all SEM as well as the corresponding XMCD-PEEM images of the measured FNT are shown.

To find the positions of the placed nanotubes with the PEEM, Au-markers were deposited for guidance onto the Si substrate. The precise alignment of the PEEM is the key to obtain images with a high spatial resolution in the range of 100 nm or even better. The three-dimensional structure of the FNT is not ideal for PEEM alignment, because topographical contrast appears at non flat surfaces and is the result of the curvature of the accelerating field around topographic features. Well-defined flat structures are well-suited for PEEM alignment. For this reason, previously four nanoscale cubes positioned close to each other were deposited using FIB in combination with platinum deposition at a reasonable distance to the FNT. The nanoscale cubes possess an almost flat surface and a well-defined geometry with a clear edge, which enables an optimal focusing of the magnetic lenses in the PEEM.

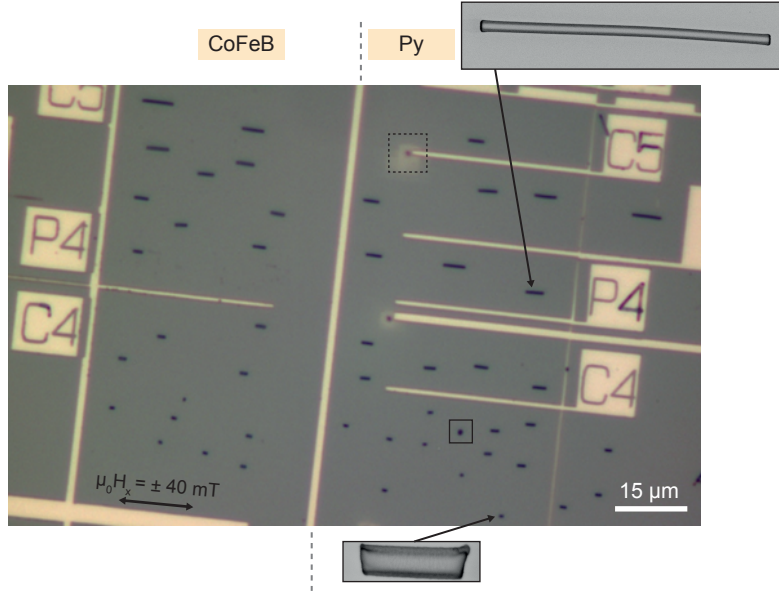


Figure 2.3. | Optical microscope image showing the with precision micromanipulators aligned CoFeB NTs on the left and Py NTs on the right side, with a length range from $11.3 \mu\text{m}$ to 540 nm onto a Si-substrate. More details about the individual NTs could be found in Appendix A. The major NT on the right side has the following dimensions, determined from the SEM image: $l = 6.9 \mu\text{m}$ and $b = 243 \text{ nm}$ and the minor: $l = 0.77 \mu\text{m}$ and $b = 237 \text{ nm}$. The dashed square in the upper part shows an example, where four well-defined nanoscale Pb cubes were deposited using FIB for the PEEM alignment. The smaller square indicates dirt and not a nanotube. A homogeneous magnetic field of $\mu_0 H_x = \pm 40 \text{ mT}$ can be applied to the sample space at room temperature and under ultra-high vacuum (UHV) conditions. The direction is shown by a black arrow.

2.5. Sample Preparation for scanning SQUID-on-tip experiments

For scanning SQUID-on-tip (SOT) experiments, the sample needs special properties due to the fragility of the tip and its limitations in what signals are detectable. In this thesis two types of magnetic nanostructures were imaged using SOT. First, the magnetic stray field of individual FNT and second the magnetic stray field of a chiral artificial spin ice system as a function of applied magnetic field. In the case of the chiral artificial spin ice system, the array of the patterned nanomagnets was big enough to align the tip above them, furthermore the expected strength of the magnetic stray field coming from nanomagnets at a safe distance of $> 1 \mu\text{m}$ was simulated and from there determined to be big enough to approach safely while detecting the DC signal.

In the case of the FNT it was not sufficient to place them on top of a blank silicon substrate as we did for the PEEM measurements. Because it is impossible to place the tip exactly above a magnetic nanostructure using a light microscope for the alignment and approach afterwards on them, another way had to be found. Typically, such problems are solved by using topographic markers to locate the samples. Our scanning probe is not sensitive to sample topography and the use of magnetic markers could cause unwanted interactions with the FNTs. Fortunately, as mentioned previous in chapter 1.3.1, the SOT devices are extremely sensitive to the AC magnetic field [39] as well as heat [40], which can both be used for navigation. For this reason a continuous Au wire was pattern on the substrate as shown in figure 2.4.

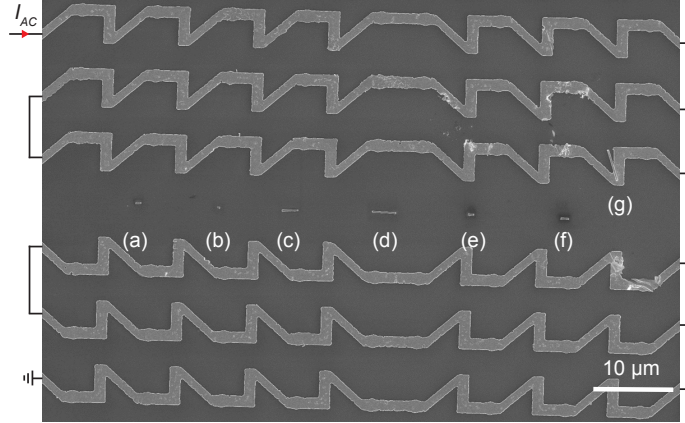


Figure 2.4. | SEM image of the sample for the scanning SQUID-on-tip measurements showing the patterned continuous Au wire for navigation and the placed FNTs labeled from (a) - (f). The SEM was taken after the experiment, before the FNT labeled with (g) was placed as the others between the close wires but was most likely removed while the tip scanned too close over the surface.

The structure of the wire is asymmetric and its varying width (not visible with this magnification) creates a temperature gradient between the hot middle area, where the FNT are located and the cold surrounding by passing an AC current through the wire. Seven FNT with different lengths are transferred with the aid of the aforementioned micromanipulators and aligned horizontally in the center of the patterned Si substrate in that way that all pointing in the same direction. The lengths of the FNT ranges from $0.7 \mu\text{m}$ to $4 \mu\text{m}$ and are obtained by cutting individual FNTs into segments using a focused ion beam (FIB). The FNTs are labeled chronologically from (a) - (g). The FNT labeled with (g) most likely removed while the tip scanned too close over the surface. The thermal signal is used for rough navigation a few hundred μm above. During the approach process, which is in detail described in chapter 1.3.4, close to the wire the geometry of the wire become visible in the magnetic and thermal signal and can be used as a marker of position. The geometry of the wire helps to find the location of the FNT. In fact, the wire serves two purposes: 1) we use it to locate the individual FNT and navigate above them at a safe distance $> 1 \mu\text{m}$; 2) by comparing the measured AC magnetic field produced by the wire with simulations of the Biot-Savart field, we use the wire to determine the distance between the substrate and the SOT. Once navigation is complete and the tip is positioned above the FNT and the distance has been determined from simulations the thermal as well as the magnetic signal from the wire is not needed anymore. The AC current can then be turned off, removing any disturbance to the measurements of the FNT magnetism.

3. Imaging of magnetic configurations in ferromagnetic nanotubes

This chapter shows the experimental results obtained by imaging the remnant magnetization configurations of ferromagnetic nanotubes (FNTs) consisting of CoFeB and Py using x-ray magnetic circular dichroism photoemission electron microscopy (XMCD-PEEM). The measurements are performed using the synchrotron radiation facilities at the Paul Scherrer Institut (PSI) in Villigen, Switzerland [8]. The obtained magnetic images of the FNTs provide direct evidence for flux-closure configurations, including a global vortex state, in which magnetization points circumferentially around the tube axis. Micromagnetic simulations predict and measurements confirm that vortex states can be programmed as the equilibrium remnant magnetization configurations by reducing the ratio of the FNTs length and diameter. The scanning SQUID-on-tip technique is used to image the magnetic stray field distribution $B_z(x, y)$ from similar FNTs, having different aspect ratios. These FNTs are imaged at cryogenic temperatures in series of applied magnetic fields perpendicular to the long axes of them. Both magnetic imaging tools show the promise of using geometry to program both the overall equilibrium magnetization configurations and the reversal process in nanomagnets.

3.1. Magnetic configurations of ferromagnetic nanotubes studied with PEEM in remanence

Adapted from:

M. Wyss, A. Mehlin, B. Gross, A. Buchter, A. Farhan, M. Buzzi, A. Kleibert, G. Tütüncüoğlu, F. Heimbach, A. Fontcuberta i Morral, D. Grundler, and M. Poggio
'Imaging magnetic vortex configurations in ferromagnetic nanotubes',
Phys. Rev. B **96**, 024423 (2017)

To image magnetic configurations of ferromagnetic nanotubes (FNTs), XMCD-PEEM measurements were performed at the Surface/Interface: Microscopy (SIM) beamline of the Swiss Light Source (SLS) at the Paul Scherrer Institut (PSI) [8]. The experiments are carried out at room temperature and under ultra-high vacuum (UHV) conditions as well as in remanence. Circularly polarized x-rays tuned to the L_3 -edge of Fe propagating along the wave vector \hat{k} impinge on the Si sample substrate with an incident angle of 16° , as shown schematically in 3.1. As mentioned in the previous subchapter 1.1.1 the obtained XMCD-PEEM image includes information about the direction of the local net magnetization of the sample under illumination to a certain depth. In the schematic drawing of a NT cross-section, the direction of the magnetization in the magnetic shell surrounding the hexagonal non-magnetic GaAs core is shown with black arrows in each facet. The magnetization points circumferentially around the NT

axis and depicts a vortex state. The used diameter of about 250 nm corresponds to the average diameter of the imaged FNT in this thesis. Direct photoemission provides as mentioned previous magnetic contrast on the FNT. I_{σ}^{\pm} at any location is proportional to both on the intensity of the incident σ^{\pm} x-rays and their absorption at that location. Absorption of σ^{\pm} x-rays is proportional to the projection of the magnetic moment along \hat{k} . Therefore, positive (red) or negative (blue) I_{XMCD} represents near surface magnetization either parallel or anti-parallel with \hat{k} , respectively. For photoemission excited by x-rays that have previously passed through magnetic material, however, the absorption in the traversed volume must also be considered [91, 92, 107]. In our images, such magnetic contrast appears in the x-ray shadow of the FNT on the non-magnetic Si substrate. Since the absorption of σ^{\pm} x-rays is proportional to the projection of the magnetic moment along \hat{k} , there is also a proportional attenuation of σ^{\pm} x-rays transmitted through the FNT and incident in the shadow. The resulting I_{σ}^{\pm} is therefore proportional to the magnetization of the volume traversed by the x-rays. This proportionality has opposite sign compared to that at a magnetic surface, i.e. positive (red) or negative (blue) I_{XMCD} results from volume magnetization either anti-parallel or parallel to \hat{k} , respectively. The expected length of the shadow depends on the incident angle α of the x-rays and can be calculated with the following rather simple equation:

$$l_{\text{shadow}} = d \cdot \frac{1}{\sin(\alpha)} \quad (3.1)$$

With an incident angle of 16° and an averaged FNT diameter of 250 nm the expected length of the shadow is $l_{\text{shadow}} = 900$ nm. Combining these two types of contrast, we extract information about both the surface and volume magnetization of the measured NTs [107]. The magnetization in the top facet is aligned parallel to the incoming wave vector and points in propagation direction of the incoming wave vector \hat{k} . The expected XMCD-PEEM contrast is shown as a color strip above the FNT and stands for the positive dichroic signal which is red (normalized difference with photons of opposite helicity). At the corresponding position in the shadow the transmitted electrons leading to negative dichroic signal which is blue. The three-dimensionality of the FNT leads to a slightly broader dichroic signal compared to the effective diameter of the FNT due to topographical surface features. This effect is known and called topographical contrast in PEEM [9]. Because of the three-dimensionality of the FNT, there is an additional contribution of photo-excited electrons into the positive dichroic signal from the two side facets flanking the top one. In the left facet, the overall magnetization points at an angle of 60° up, while on the right side, it points at an angle of 60° down as shown in figure 3.1.

The slightly larger dichroic signal is clearly visible in the XMCD-PEEM image at both ends of the FNT in figure 3.2 (c) compared to the dashed black line, which shows the position and the dimension of the FNT. The obtained XMCD-PEEM images have a spatial resolution of ~ 100 nm, depending on the quality of the focus and properties of the sample, including morphology and cleanliness. Figure 3.2 (a) shows a SEM of a representative $11.3\text{-}\mu\text{m}$ -long CoFeB nanotube aligned close to an Au-marker on top of a silicon substrate. A PEEM image of the same FNT in figure 3.2 (b) shows the $I_{\text{PEEM}} = (I_{\sigma} + I_{\sigma'})/2$ with the FNT long axis \hat{n} aligned perpendicular to the x-ray beam appears. Due to the resonant excitation of the Fe L_3 -edge, PEEM contrast from the FNT surface appears as the brightest feature. The dark stripe on the right of the NT is a shadow effect resulting from the grazing incidence of the incident x-rays and their partial attenuation by the FNT. A bright region to the left of the FNT appears due to x-rays

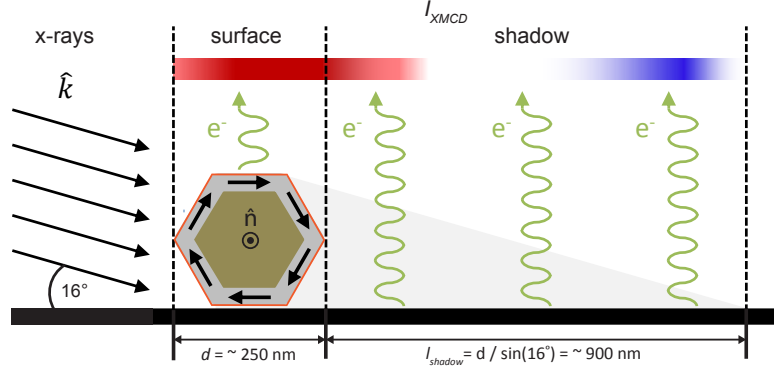


Figure 3.1. | Schematic drawing of a nanotube cross-section with incident x-rays, photoexcited electrons, and expected XMCD-PEEM contrast for the depicted vortex configuration. The brown central region depicts the non-magnetic GaAs template material, the gray region the magnetic NT, and the red region the native oxide layer.

reflected by the smooth surface of the FNT. A dotted outline shows the position of the FNT in the corresponding XMCD-PEEM image in figure 3.2 (c), as determined by overlaying SEM, PEEM, and XMCD-PEEM images of the same FNT, more details you find in Appendix A. I_{XMCD} within the outline stems from a region on top of the FNT within 3 to 5 nm of the surface and is proportional to the projection of its local magnetization along \hat{k} . I_{XMCD} in the shadow on the right of the outline — on the non-magnetic Si surface — depends on the imbalance in the intensity of σ_{\pm} x-rays transmitted through the magnetic material, rather than any surface magnetization [92]. The contrast in the shadow region is therefore sensitive to the average magnetization of the volume traversed by the x-rays, with opposite sign compared to surface contrast as mentioned before. The lack of surface and shadow I_{XMCD} contrast corresponding to the central part of the FNT in figure 3.2 (c) indicates negligible magnetization oriented parallel to \hat{k} (perpendicular to \hat{n}). On the other hand, at the NT ends, strong surface and shadow contrast indicates magnetization oriented parallel to \hat{k} (perpendicular to \hat{n}), indicating that the magnetic state of this FNT is a mixed state.

XMCD-PEEM images with $\hat{k} \perp \hat{n}$ (perpendicular XMCD-PEEM contrast) are shown in figures 3.3 (a) and (c) for Py and CoFeB NTs with lengths of 6.9 and 7.2 μm , respectively. Contrast similar to that of figure 3.2 (c) shows magnetization oriented perpendicular to \hat{n} near the ends of the FNTs. Further information is gleaned by rotating the sample stage relative to \hat{k} and performing the same measurements with $\hat{k} \parallel \hat{n}$ (parallel XMCD-PEEM contrast), as shown in figures 3.3 (b) and (d). In this case, strong surface contrast in the central part of the FNT indicates magnetization parallel to \hat{n} . Decreased contrast at the FNT ends confirms a magnetization oriented perpendicular to \hat{n} , as suggested by the measurements with $\hat{k} \parallel \hat{n}$. In figures 3.3 (a) and (c), residual surface and shadow contrast corresponding to the central parts of the FNTs may be due to a slightly tilted axial magnetization or an imperfect perpendicular alignment of the x-rays with respect to the FNTs.

The latter explanation may also account for the tilt in the opposing surface and shadow contrast at the end of the NT with respect to \hat{k} indicated in figure 3.3 (a). Also, despite the strong shadows contrast from the ends in figure 3.3 (c), the corresponding surface contrast is weak. This lack of contrast is likely due to oxidation of the NT surface. Given the limited probing depth related to the surface contrast and the fact that the shadow contrast originates from the magnetization within the FNT, in such cases, we rely on I_{XMCD} in the shadow to

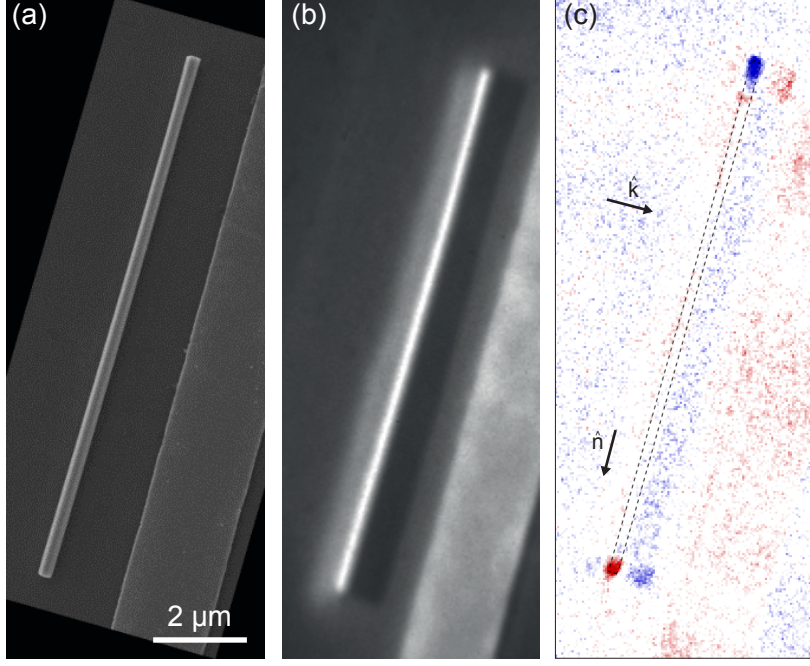


Figure 3.2. | (a) SEM of an 11.3- μm -long CoFeB NT with an Au alignment marker visible on the right of the image. (b) PEEM image with grayscale contrast corresponding to I_{PEEM} and (c) XMCD-PEEM image with red (blue) contrast representing positive (negative) I_{XMCD} . The dashed line shows the position and the dimension of the FNT.

determine the NT's magnetic configuration. As mentioned previous specific magnetization configurations in a magnetic nanostructure produce characteristic XMCD-PEEM signatures for a given orientation of \hat{k} . This contrast is characterized by both strong surface and shadow contrast (due to the component of the magnetization aligned parallel to \hat{k}) and a change of sign in the x-ray shadow. Figures 3.3 (e) and (g) show linecuts through the perpendicular XMCD-PEEM image at the FNT ends consistent with this expectation. However, since the FNTs lie directly on the substrate and are not suspended as in Jamet et al. [91], part of the shadow is occluded. As a result, surface and shadow contrasts partially merge, making it difficult to distinguish the sign reversal in the shadow. As a result, although the presence of remnant vortex domains is strongly supported by simulations discussed in chapter 3.2 and shown in figures 3.3 (i) and (j), their unambiguous identification is not possible on the basis of these images alone. Figures 3.3 (f) and (h) show linecuts of parallel XMCD-PEEM images through the same region along \hat{n} .

The reduction in the surface contrast near the end of the NT relative to the central region is also consistent with decreasing on-axis magnetization due to a vortex end state. The complementarity of vanishing and strong contrast in the central part of the FNT in the perpendicular and parallel XMCD-PEEM images, respectively, provides strong evidence for an axially aligned central region. Taken together, these images point to a mixed state configuration, where magnetic moments in the central part of the NT align along its long axis and curl into vortices at the ends. The relative sign of the perpendicular XMCD-PEEM contrast at the ends of the NTs shown in figures 3.3 (a) and (c) indicates that they are in mixed states with end vortices of opposing and matching circulation, respectively. For FNTs of either material longer than 2

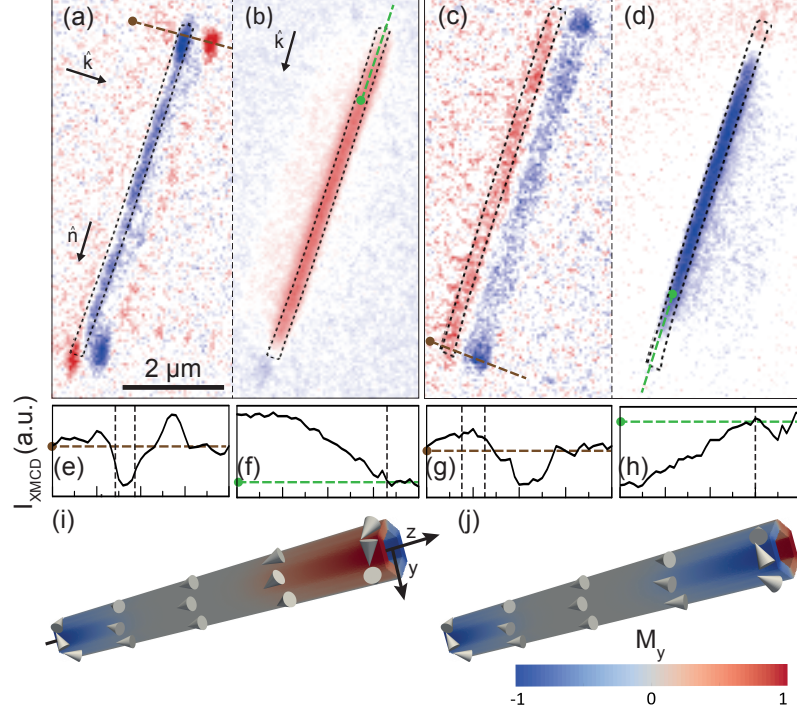


Figure 3.3. | XMCD-PEEM images of a 6.9- μm -long Py NT with (a) $\hat{k} \perp \hat{n}$ and (b) $\hat{k} \parallel \hat{n}$ and of a 7.2- μm -long CoFeB NT with (c) $\hat{k} \perp \hat{n}$ and (d) $\hat{k} \parallel \hat{n}$. Dashed outlines indicate the positions of the NTs. (e) - (h) represent 2- μm -long I_{XMCD} linecuts along the corresponding colored dashed lines in (a) - (d). In the linecuts, the background intensity is indicated by the level of the horizontal dashed lines and vertical dashed lines delineate the boundaries of the NT. (i) and (j) show simulated remnant magnetic states for a NT with $l = 2.1 \mu\text{m}$ and $d = 245 \text{ nm}$. Both configurations are mixed states with an axial central domain and vortex ends of either (i) opposing circulation – consistent with (a) and (b) – or (j) matching circulation – consistent with (c) and (d). The color-scale corresponds to normalized magnetization along \hat{y} . Arrow heads indicate the local magnetization direction.

μm , we find remnant mixed states with vortices of both opposing and matching circulation, as shown in figure 3.3.

For NTs shorter than 2 μm , different magnetization configurations emerge. Figure 3.4 (a) shows both perpendicular and parallel XMCD-PEEM images of a 1.30- μm -long Py nanotube. In the perpendicular image, nearly all magnetic moments point perpendicular to \hat{n} and show the signature of a global vortex state with a single sense of circulation. In the parallel image, a small area of axial moments is visible in the surface contrast, indicating either a slightly tilted vortex configuration or imperfections at the surface of the magnetic shell. Figure 3.4 (b) shows XMCD-PEEM contrast from a 0.73- μm -long Py NT, in which the magnetization points mostly perpendicular to the NT axis. The remnant magnetization configuration, however, does not display a vortex with a single circulation sense, but rather two vortices of opposing circulations separated by an axial Néel domain wall. This central wall produces vanishing shadow contrast (white) in the perpendicular image, while showing strong positive (red) surface and negative (blue) shadow contrast in the parallel image, as expected for magnetization aligned along \hat{n} . We therefore conclude that this FNT is in an opposing vortex state. Results for CoFeB NTs of similar sizes are shown in figures 3.4 (c) and (d). Figure 3.4 (c) shows contrast from a 1.06-

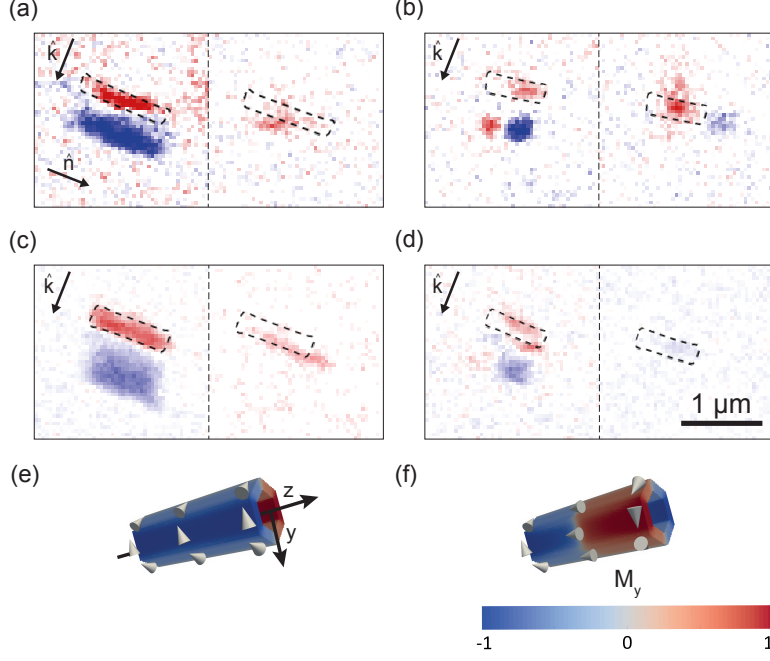


Figure 3.4. | XMCD-PEEM images with $\hat{k} \perp \hat{n}$ and $\hat{k} \parallel \hat{n}$ of short NTs. (a) 1.3- μm -long Py NT found in a global vortex state. (b) 0.73- μm -long Py NT in an opposing vortex state. (c) 1.06- μm -long CoFeB NT in a global vortex state. (d) 0.83- μm -long CoFeB NT in an opposing vortex state. Simulated equilibrium states of ferromagnetic NTs ($l = 610$ nm, $d = 245$ nm) in (e) a global vortex state and in (f) an opposing vortex state. The color-scale corresponds to the normalized magnetization along \hat{y} . Arrow heads indicate the local magnetization direction.

μm -long FNT in a remnant global vortex state, whereas figure 3.4 (d) shows a 0.83- μm -long FNT in a remnant opposing vortex state.

3.2. Numerical Micromagnetic Simulations

To corroborate the XMCD-PEEM measurements, numerical simulations of FNT magnetization using the software package Mumax3 [108], were carried out. This package employs the Landau-Lifshitz micromagnetic formalism using a finite-difference discretization. In the simulations the saturation magnetization $\mu_0 M_s$ was set to its measured value of 1.3 T [59] and 0.8 T [64] and the exchange stiffness to $A_{\text{ex}} = 28$ pJ/m and 13 pJ/m for CoFeB and Py, respectively. In our model no magneto-crystalline or growth-induced anisotropies are included. Further in the simulations no thermal fluctuations are included and space is discretized to 5 nm. The dipolar exchange length could be calculated using the following equation:

$$\Delta d = \sqrt{\frac{2A_{\text{ex}}}{\mu_0 M_s}} \quad (3.2)$$

Under the use of the aforementioned values for the exchange stiffness and the saturation magnetization, a dipolar exchange length of $\Delta d \simeq 10$ nm is calculated. Numerical artifacts in the calculations of the energy difference between configurations showing vortices with matching or

opposing circulation sense were found for cell sizes of 1 nm or larger. In particular, insufficient discretization leads to a spurious region in the parameter space, where the opposing vortex configuration is the lowest energy state. Reducing the cell-size from 10 nm down to 1 nm, this region disappears. It turns out that, in fact, there is no region in the diameter versus length phase diagram where the opposing configuration is the lowest energy state. For short tubes, the matching vortex configuration (global vortex state) is the lowest energy state; for long tubes, both matching and opposing vortex configurations have the same energy.

3.3. Comparison to micromagnetic simulations

Numerically expected equilibrium configurations and the experimentally observed remnant configurations as a function of the diameter d and length l are compared in the following. Experimental results are extracted from perpendicular and parallel XMCD-PEEM images of each measured FNT (for details, see Appendix A). Simulations are consistent with our XMCD-PEEM measurements in that long NTs are calculated to have remnant mixed state configurations, as depicted in figures 3.3 (i) and (j), and short NTs remnant global vortex or opposing vortex states, as depicted in figures 3.4 (e) and (f) in the previous chapter 3.1. The simulations also reproduce subtleties of the magnetization configurations in the FNTs, including the length of the vortex ends and its dependence on d . The average length of the vortices along \hat{n} is measured to be 320 ± 50 nm for CoFeB NTs and 360 ± 50 nm for Py NTs. Despite the agreement, the relative circulation sense of the end vortices predicted by the simulations does not exactly match our observations. For long NTs in remnant mixed state configurations, the energy difference between a configuration with matching or opposing circulation vortices is calculated to be small compared to the precision of the simulation; therefore, each is predicted to be equally likely. Furthermore our simulations show no combination of length and diameter, for which opposing circulation is energetically favored over matching circulation. However, we find that insufficient discretization of the numerical cells can lead to this erroneous result. It is likely that earlier numerical simulations [77, 89], showing the mixed state with end vortices of opposing circulation as the low-field equilibrium configuration, are affected by this artifact and are therefore incorrect.

In the real FNTs, although the distribution is equal across all FNTs, it is unequal for a single material: three opposing and eight matching mixed states appear in CoFeB NTs, while nine opposing and four matching appear in Py NTs. As the length-to-diameter ratio is reduced, simulations indicate that the relative circulation of the end vortices leads to energy differences larger than the thermal energy. As the central region of axial magnetization disappears, matching circulation is eventually favored, resulting in a stable global vortex state. For NTs of both CoFeB and Py short enough to favor matching circulation and therefore a global vortex configuration ($l \lesssim 2.2 \mu\text{m}$ for CoFeB and $l \lesssim 1.6 \mu\text{m}$ for Py), we observe seven global and two opposing vortex states in CoFeB NTs and six global, two opposing vortex, and three states that switch configuration upon a second measurement in Py NTs. Although the overall trend confirms the numerical predictions, the discrepancies suggest that imperfections may still be decisive in energetically favoring one configuration over another. Simulations show that in equilibrium the relative circulation sense is sensitive to variations in NT thickness as well as geometrical imperfections, such as slanted rather than flat ends introduced by the FIB cutting process. Given that such imperfections are known to be present, we assume that they play a role in determining the relative circulation of the end vortices.

If we consider FNTs measured to have vortices with equal circulation sense, we find that the NT length-to-diameter ratio dictates whether the remnant state is a global vortex state, consistent with the simulations. In figures 3.5 (a) and (b), FNTs measured to be in either a mixed or global vortex state are plotted as a function of l and d together with the numerical expectation. We distinguish between a global vortex state and a mixed state with an axially aligned central domain and vortices with equal circulation sense. The presence of the central domain can be quantified by an order parameter $M_n/|M|$ corresponding to the relative amount of magnetization that is axially aligned.

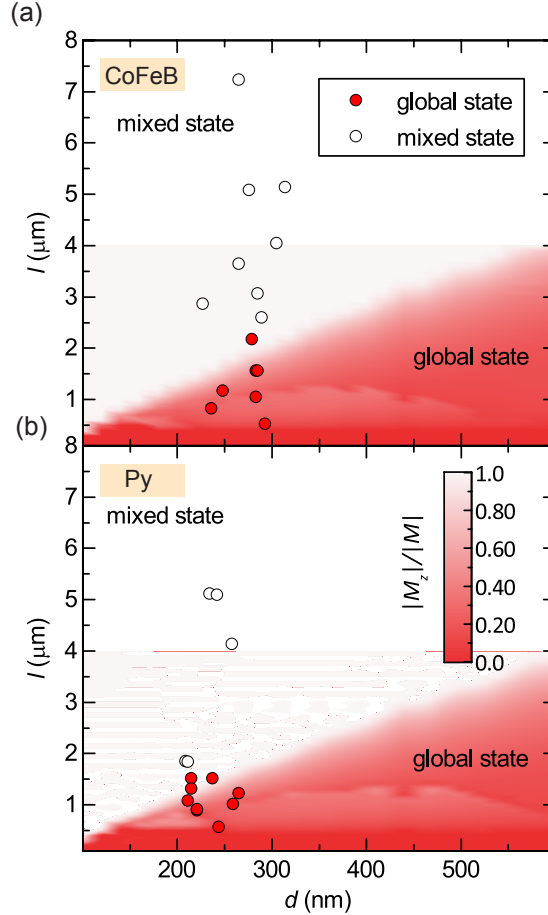


Figure 3.5. | Phase diagrams for (a) CoFeB and (b) Py NTs as a function of l and d considering only magnetization configurations with equal circulation sense. The numerically calculated order parameter $M_n/|M|$ is plotted in the color scale and defines the boundary between the mixed and global vortex state. Red (white) points show measurements of real NTs in global vortex (mixed) states as measured by XMCD-PEEM (see Appendix A).

By plotting this order parameter for numerical simulations of FNTs with different lengths and diameters, a clear boundary between the mixed state and global vortex state emerges, as shown in figures 3.5 (a) and (b). The same classification is carried out on the measurements, with the global vortex state determined by the absence of a well-resolved axial domain in the XMCD-PEEM images. The measured dependence of magnetic configuration on geometry not

only agrees closely with the numerical simulations, but is also qualitatively consistent with analytical predictions for cylindrical ferromagnetic nanotubes by Landeros et al. [75]. If we consider NTs having end vortices of opposing circulation sense, a similar phase boundary can be defined between a mixed state configuration with opposing end vortices and an opposing vortex state incorporating a Néel wall. The transition from an axial central domain, found in the mixed state, to the Néel domain wall can be quantified by the presence of inflection points in plots of $M_n/|\mathbf{M}|$ along \hat{n} . Unfortunately, the available spatial resolution of XMCD-PEEM, which was in this measurement period 100 nm, is not sufficient to clearly determine the inflection points and therefore to distinguish between these two states. To test the robustness of the remnant magnetization configurations, for some FNTs, we take a second set of XMCD-PEEM images in remanence after applying a magnetic field of 40 mT along \hat{n} to saturate the FNTs in situ. The extra developed design of the XPEEM holder, which allows to apply a magnetic field along \hat{n} to saturate the FNTs in situ is shown in Appendix A.1. In eleven cases, the measured remnant configuration is observed to be identical to the one initially measured, while in six cases the relative circulation sense of the end vortices changes. According to the simulations, in these six cases, the dimensions of the FNTs are such that a matching or opposing circulation sense does not significantly affect its magnetic energy. These include long FNTs in mixed states and FNTs calculated to be close to the phase boundary between where equal circulation sense begins to be favored. Sample imperfections may trigger the change in relative circulation sense in such FNTs.

3.4. Conclusion to magnetic configurations in FNTs imaged with XMCD-PEEM

The remnant equilibrium magnetization configuration of CoFeB and Py NTs of a variety of lengths at room-temperature was imaged using XMCD-PEEM. The study reveals, that short FNTs can occupy a stable global vortex state in remanence. Consistent with an analytical theory by Landeros et al. [75] and our own numerical simulations, the NT length-to-diameter ratio is found to play a crucial role in stabilizing the global vortex state. XMCD-PEEM images of the equilibrium magnetization configurations show that the relative circulation sense of vortex ends in real FNTs is less controlled than expected from simulations. As a result, short FNTs are found not only in remnant global vortex states, but also in opposing vortex states, which include a Néel wall between two opposing vortices. Additional simulations suggest that sample imperfections including variations in thickness and deviations from a perfect geometry are responsible for this discrepancy. Still, our magnetic images of global vortex states show that the most important properties predicted for idealized FNTs, have been realized in real structures. They also demonstrate the programming of the equilibrium magnetic configuration of a FNT via geometry, a result consistent with long-standing theoretical predictions.

3.5. Imaging stray magnetic field of individual ferromagnetic nanotubes using scanning SQUID-on-tip

Adapted from:

D. Vasyukov, L. Ceccarelli, M. Wyss, B. Gross, A. Schwarb, A. Mehlin, N. Rossi, G. Tütüncüoğlu, F. Heimbach, R. R. Zamani, A. Kovács, A. Fontcuberta i Morral, D. Grundler, M. Poggio 'Imaging stray magnetic field of individual ferromagnetic nanotubes', Nano Lett. **18**, 964 (2018)

In the previous chapter 3.1 the imaging of the magnetic configuration of individual ferromagnetic nanotubes (FNT) having different lengths and therefore different aspect ratios studied with PEEM were described. Under the use of this magnetic imaging method it was only possible to map the remnant magnetic configuration of the FNT and not as function of applied magnetic field. The reason is that an external applied magnetic field has a strong influence on the trajectory of the secondary electrons, which causes a large distortion of the image as mentioned in chapter 1.4. The SQUID-on-tip technique on the other hand offers the unique opportunity to map the magnetic stray field component pointing in z -direction above the FNT at different applied out-of plane magnetic fields as well as close to zero. The possible measurement range depends on the specific current-to-voltage-characteristics (IVC) of the used SQUID-on-tip.

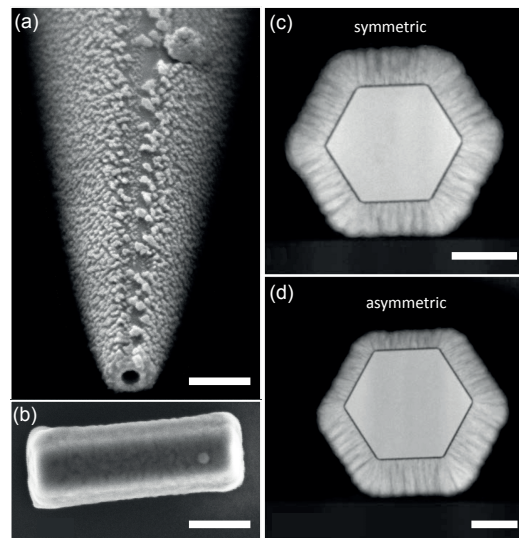


Figure 3.6. | (a) SEM image of the SQUID-on-tip, which has an effective diameter of 150 nm. (b) SEM image of the 0.7- μm -long FNTs. (c,d) Cross-sectional high-angle annular dark-field (HAADF) scanning transmission micrographs (STEMs) of two FNTs from a similar growth batch as those measured. The scalebars represents 200 nm in (a,b) and 50 nm in (c,d).

Driven by these advantages, a similar experiment was carried out using a scanning SQUID-on-tip to map the magnetic stray field distribution $B_z(x, y)$, produced by FNTs as a function of position and applied magnetic field. The images show the extent to which flux closure is

achieved in FNTs of different lengths as they are driven through magnetic reversal. Figure 3.6 (a) shows a SEM image of the SQUID-on-tip, which has an effective diameter of 150 nm. This value is extracted from measurements of the critical current I_{SOT} as a function of a uniform magnetic field H_z applied perpendicular to the SQUID loop (more details about the SQUID-on-tip characterization is described in chapter 1.3.3). Maps of the magnetic stray field produced by individual FNTs are made by scanning the FNTs lying on the substrate in the xy -plane 300 nm below the SQUID-on-tip sensor. For each value of the externally applied field H_z , a factor is extracted from the current-field interference pattern to convert the measured current I_{SOT} to the flux. The measured flux then represents the integral of the z -component of the total magnetic field over the area of the SQUID loop. By subtracting the contribution of H_z , we isolate the z -component of stray field, H_{DC} integrated over the area of the SQUID-on-tip at each spatial position.

Figure 3.7 (a) shows the magnetic stray field distribution $B_z(x, y)$ of a 4- μm -long FNT for a series of applied magnetic fields increased from -0.6 to 0.6 T. The maps reveal a reversal process roughly consistent with a rotation of the net FNT magnetization. At $H_z = -249$ mT and more negative fields, B_z is nearly uniform above the FNT, indicating that its magnetization is initially aligned along the applied field and thus parallel to $-\hat{z}$. As the field is increased toward positive values, maps of B_z show an average magnetization $\langle \mathbf{M} \rangle$, which rotates toward the long axis of the FNT. With increasing positive H_z , the reversal proceeds until the magnetization aligns along \hat{z} .

Figure 3.7 (b) shows the corresponding simulated stray field distributions, which are generated by a numerical micromagnetic model of the equilibrium magnetization configuration. For the numerical micromagnetic simulations the same Mumax3 package as for the XMCD-PEEM measurements, described in chapter 3.2, is used [108]. The length $l = 4.08$ μm and diameter $d = 260$ nm of the FNT are determined by SEMs of the sample, while the thickness $t = 30$ nm is taken from cross-sectional TEMs of samples from the same batch. The simulated stray-field distributions closely match the measurements. The magnetization configurations extracted from the simulations are nonuniform, as shown in Figure 3.7 (c). In the central part of the FNT, the magnetization of the different facets in the hexagonal FNT rotates separately as a function of H_z , due to their shape anisotropy and their different orientations. As H_z approaches zero, vortices nucleate at the FNT ends, resulting in a low-field mixed state, in which magnetization in the central part of the FNT aligns along its long axis and curls into azimuthally aligned vortex domains at the ends. The same result was obtained using XMCD-PEEM, which is described more in detail in chapter 3.1 and dynamic cantilever magnetometry (DCM) measurements [60] of similar FNTs at room-temperature.

FNTs shorter than 2 μm exhibit qualitatively different stray-field progressions. Figure 3.8 (a) shows the magnetic stray field distribution $B_z(x, y)$ of a 0.7- μm -long FNT for a series of applied magnetic fields H_z applied perpendicular to its long axes.

A stray-field pattern with a single lobe persists from large negative field to $H_z = 15$ mT without an indication of $\langle M \rangle$ rotating toward the long axis. Near zero field, a stray-field map characterized by an ‘‘S’’-like zero-field line appears (white contrast in 3.8 (a)). At more positive fields, a single lobe again dominates. A similar progression of stray field images is also observed upon the reversal of a 1- μm -long FNT, which is not shown in this thesis. In order to infer the magnetic configuration of the FNT, we simulate its equilibrium configuration as a function of H_z using the sample’s measured parameters: $l = 0.7$ μm , $d = 250$ nm, and $t = 30$ nm. For a perfectly hexagonal FNT with flat ends, the simulated reversal proceeds through different, slightly distorted global vortex states, which depend on the initial conditions of the

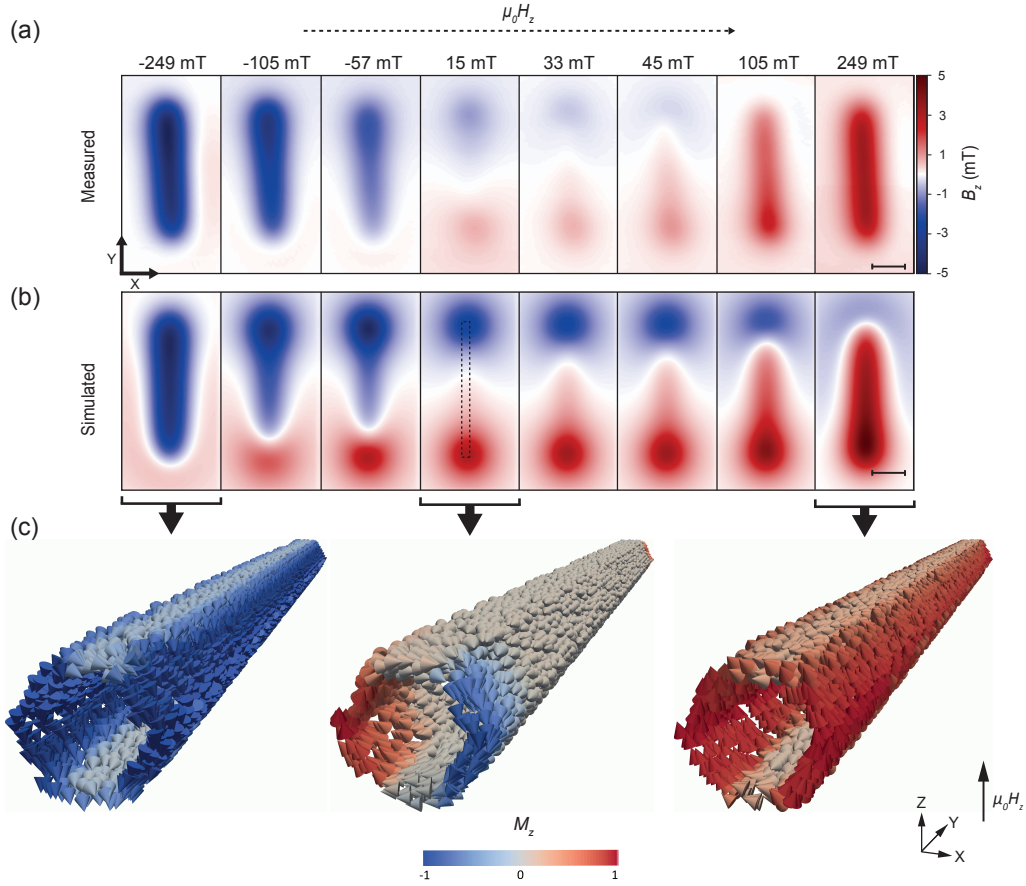


Figure 3.7. | (a) Series of measured magnetic stray field distributions $B_z(x,y)$ of a 4- μm -long FNT ($l = 4.08 \mu\text{m}$, $d = 260 \text{ nm}$) at different magnetic fields H_z applied perpendicular to its long axes. The probe-to-sample distance is thereby 300 nm. (b) Numerical simulations of the equilibrium magnetization configuration. The dashed line deliniates the position of the FNT. The scalebar corresponds to 1 μm . (c) Simulated configurations corresponding to three values of H_z . The middle configuration, nearest to zero field, shows a mixed state with vortex end domains of opposing circulation sense.

magnetization. As shown in figure 3.8 (b), such simulations do not reproduce the “S”- like zero-field line observed in the measured magnetic stray field distributions. However, when we consider defects and structural asymmetries likely to be present in the measured FNT, the simulated and measured images come into agreement, as shown in figure 3.8 (c). In these simulations, first a magnetic “dead-layer” induced by the FIB cutting of the FNT ends is considered as previously reported [61–63]. Therefore the length of the simulated FNT is reduced by 100 nm on either side. Second, a not perfectly perpendicular FIB-cut of the FNT ends to its long axes is taken into account. SEMs of the investigated FNT show that the FIB cutting process results in ends slanted by 10° with respect to \hat{z} . Finally, the 30 nm thick hexagonal magnetic shell is considered to be asymmetric, which means that one side of the FNT is slightly thicker due to inhomogeneous deposition as shown in the cross-sectional high-angle annular dark-field (HAADF) scanning transmission micrographs (STEMs) in figure 3.6 (e). With these modifications, the simulated reversal proceeds through at least four different possible stray-field progressions depending on the initial conditions. Only two of these, shown

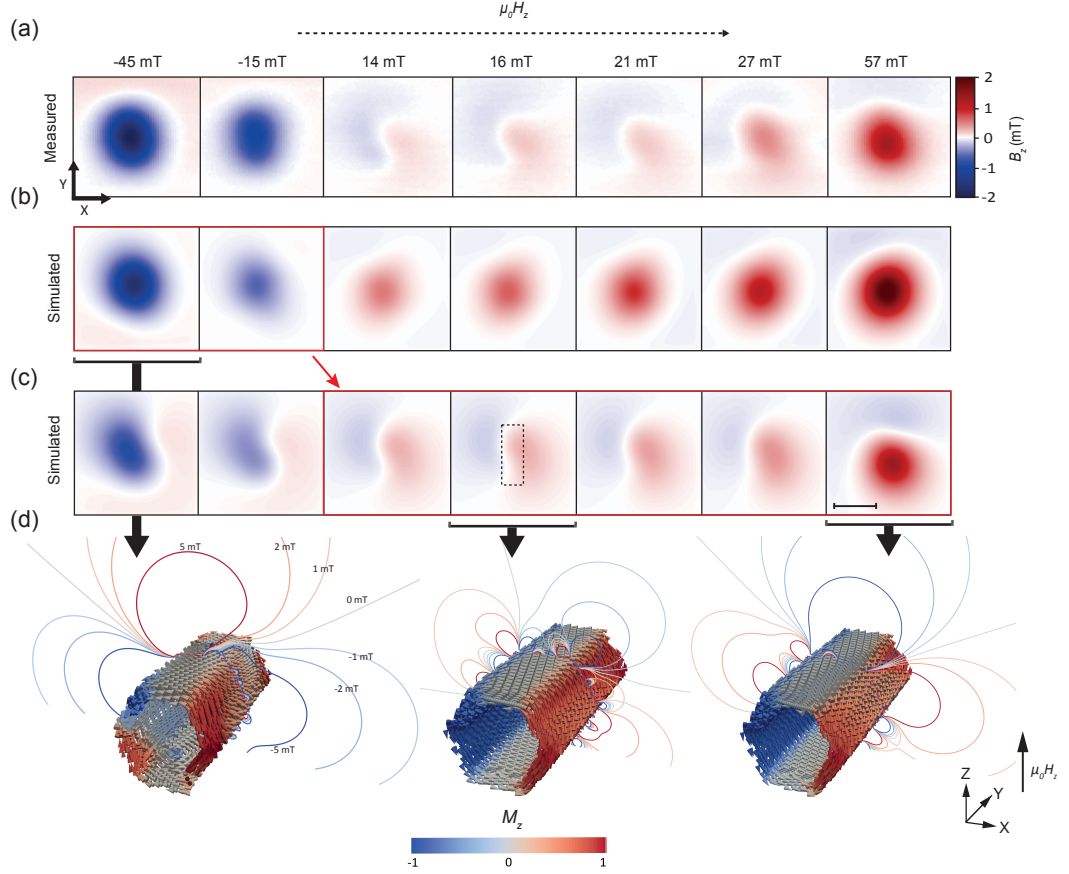


Figure 3.8. | (a) Series of measured magnetic stray field distributions $B_z(x, y)$ of a $0.7\text{-}\mu\text{m}$ -long FNT ($l = 0.69\ \mu\text{m}$, $d = 250\ \text{nm}$) at different magnetic fields H_z applied perpendicular to its long axes. The probe-to-sample distance is thereby $300\ \text{nm}$. (b,c) Numerical simulations of the equilibrium magnetization configuration with different initial conditions. The dashed line delineates the position of the FNT. The scalebar corresponds to $0.5\ \mu\text{m}$. (d) Magnetization configurations and contours of the magnetic stray field corresponding to three values of H_z . The configuration on the left is characterized by two vortices in the top and bottom facets, respectively. The middle and right configurations are distorted global vortex states.

in figure 3.8 (b,c), produced stray-field maps which resemble the measurement. The measured stray-field images are consistent with the series shown in 3.8 (b) for negative fields ($H_z = -45, -15\ \text{mT}$). As the applied field crosses zero ($15\ \text{mT} \leq H_z \leq 14\ \text{mT}$), the FNT appears to change stray-field progressions. The images taken at positive fields ($14\ \text{mT} \leq H_z$) show patterns consistent with the series shown in figure 3.8 (c). The magnetic configurations corresponding to these simulated stray-field maps suggest that the FNT occupies a slightly distorted global vortex state. Before entering this state, for example, at $H_z = 45\ \text{mT}$, the simulations show a more complex configuration with magnetic vortices in the top and bottom facets, rather than at the FNT ends. On the other hand, at similar reverse fields, for example, $H_z = 57\ \text{mT}$, the FNT is shown to occupy a distortion of the global vortex state with a tilt of the magnetization toward the FNT long axis in some of the hexagonal facets.

3.6. Conclusion to the magnetic imaging under the use of two different magnetic imaging techniques

The XMCD-PEEM measurements performed at room-temperature, discussed in chapter 3.1, showed that the types of remnant states that emerge in FNTs depend on their length. For FNTs of these cross-sectional dimensions longer than $2 \mu\text{m}$, the equilibrium remnant state at room-temperature is the mixed state, while shorter FNTs favor global or opposing vortex states. The scanning SQUID-on-tip measurements confirm these observations at cryogenic temperatures by mapping the magnetic stray-field produced by the FNTs rather than their magnetization. The defining property of flux-closure configurations, which is when their stray-field vanishes, is directly imaged. It was found, that the imperfect geometry of the FNTs causes even the global vortex state to produce stray fields on the order of $100 \mu\text{T}$ at a probe-sample distance of 300 nm. Finer control of the sample geometry is required in order to reduce this stray field and for such devices to be considered as elements in ultrahigh density magnetic storage. Nevertheless, the global vortex is shown to be robust to the imperfections of real samples; despite slight distortions, it continues to be dominated by a single azimuthally aligned vortex.

Using the scanning SQUID's ability to make images as a function of applied magnetic field, we also reveal the progression of stray-field patterns produced by the FNTs as they reverse their magnetization. Future scanning SQUID-on-tip experiments in parallel applied fields could further test the applicability of established theory to real FNTs [75, 93, 95, 96]. While the incomplete flux closure and the presence of magnetization configurations not predicted by simulation indicate that FNT samples still cannot be considered ideal, scanning SQUID-on-tip images show the promise of using geometry to program both the overall equilibrium magnetization configurations and the reversal process in nanomagnets.

4. Introduction to Artificial Spin Ices

This chapter provides an introduction to artificial spin ice systems. In particular a novel geometry, the “chiral ice” will be introduced. Furthermore the design as well as the fabrication of this system, which consists of magnetostatically-coupled nanomagnets, will be described. Recent experimental measurements will be discussed, which have shown that the magnetostatic field at the edges of the array is responsible for an observed collective rotation of the average magnetization in a unique sense during thermal relaxation at room temperature, analogous to a ratchet. In thicker samples, two energetically stable edge states exist due to the bending of the magnetization at the edges of the nanomagnets. Furthermore, I show that the edge bending increases the number of degrees of freedom of the magnetization in artificial spin ice and that these additional degrees of freedom are not captured in dipolar models, which are typically used in studies of artificial spin ice systems.

4.1. From water ice to artificial spin ice

Frustration is a phenomenon found in many condensed matter systems. Frustration arises when all interactions cannot be satisfied at the same time, leading to highly degenerate low-energy states. If frustration arises in a system the substance can never be completely frozen, because the structure which builds it cannot reach a single low-energy state and a non-zero entropy at 0 K. Such residual or zero-point entropy has first been measured in crystalline ice by Giauque and co-workers [109, 110]. The measured crystalline ice displayed disorder down to extremely low temperatures. Shortly before this experimental discovery, L. Pauling introduced the concept of macroscopically degenerate ground state, which played an important role in understanding this observation [111]. Pauling describes proton disorder in terms of the mismatch between the crystal symmetry and the local requirements in water ice. This special type of disorder obeys the so-called “ice rules.” These were previously proposed by Bernal and Fowler and describe how two protons are closer to and two are further away from each oxide ion, such that the crystal structure consists of hydrogen-bonded water molecules [112] as shown in figure 4.1 (a). Remarkably, the ice rules are not unique to water ice: they are equally found in a particular type of frustrated ferromagnetic material, in which they arise from the collective behavior of the material. It has long been thought that geometric frustration could not occur in ferromagnetic systems until the discovery of the pyrochlore $\text{Ho}_2\text{Ti}_2\text{O}_7$ in 1997 [113]. In pyrochlore, the spins are located at the corners of tetrahedra. In addition to ferromagnetic coupling between the spins, the crystal field forces the spins to point along $\langle 111 \rangle$ -directions. This causes the ferromagnetically coupled Ising-spins to point either towards or away from the center of the tetrahedra, leading to a 2-spin in/2-spin out ice rule for each tetrahedron as shown in figure 4.1 (b). This spin configuration is analogue to the proton ordering in water ice, hence the term “spin ice.” Over the past decade, extensive effort has been directed towards the investigation of artificial spin ice systems, which consist of dipolar coupled ferromagnetic nanomagnets arranged in two-dimensional frustrated geometries, fabricated by electron beam lithography

[114]. The dipolar interactions favor a head-to-tail arrangement of the moments and the two-in/two-out ice rule is therefore obeyed at each vertex, equivalent to the proton ordering in water ice. Figure 4.1 (c) shows an artificial spin ice system consisting of ferromagnetic nanomagnets arranged in a two-dimensional geometry, where the nanomagnets occupy the sites of a square lattice, called artificial square ice [114, 118].

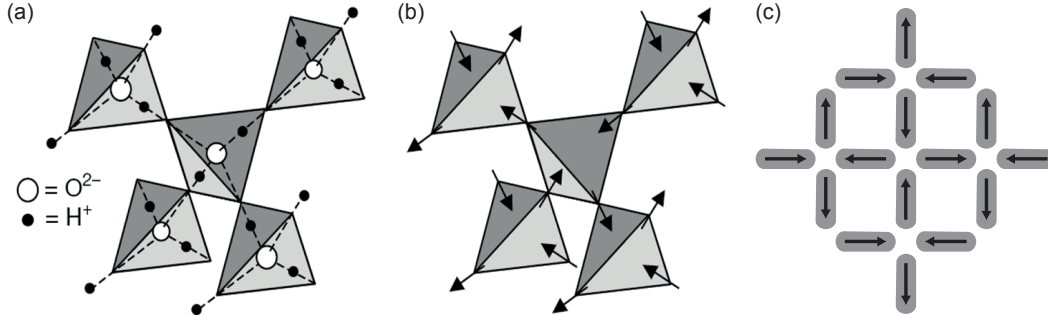


Figure 4.1. | (a) Proton ordering in water ice, obeying the so-called “ice rules” [111]. (b) Geometrical frustration discovered in the rare-earth titanate pyrochlore $\text{Ho}_2\text{Ti}_2\text{O}_7$ called spin ice [113]. The spins to point towards or away from the center of the tetrahedra, giving us a two-spins-in and two-spins-out „ice rule.“ This is equivalent to the geometrical frustration in ice. (c) Lithographically patterned single-domain nanomagnets arranged on a two-dimensional geometrically frustrated square lattice [114], fabricated by electron beam lithography, called artificial spin ice.

The lithographically patterned nanomagnets are a few nanometers thick and small enough to be single-domain. They have an elongated shape and due to the shape anisotropy the magnetization is forced to point towards the long axes, mimicking an Ising-like magnetic spin [114]. Four nanomagnets neighboring each other at a vertex are magnetostatically coupled. The strength of the coupling depends strongly on the distance between the neighboring nanomagnets, which is defined by the lattice constant. An increasing lattice constant leads to a decreasing dipolar coupling [20]. An advantage of these planar two-dimensional geometries is, compared to three-dimensional system like pyrochlore, that their magnetic configuration can be directly visualized using conventional scanning probe methods like for instance magnetic force microscopy (MFM) [114, 119], optical methods like high-resolution aberration-corrected Lorentz transmission electron microscopy (LTEM) [120] or photoemission electron microscopy (PEEM) [18, 19]. Another advantage is that the geometric arrangement, as well as the shape of the nanomagnets can be controlled. Therefore two-dimensional spin ice systems constitute a rich playground for exotic geometries like for instance the Tetris ice [115], which is maximally frustrated, or the Santa Fe ice [116, 117], which can support both frustrated and unfrustrated loops, to only mention two examples.

Despite the fact that the artificial square ice reproduces some of the properties of atomic spin ices, such as obeying the ice rules in the ground state, it is fundamentally different from atomic spin ices due to its doubly degenerated ground state (i.e. it is not frustrated) and the additional degrees of freedom due to the edge bending of the magnetization [124]. In theoretical models, individual nanomagnets are typically treated as single Ising-spins with two degrees of freedom. This is, however, in certain cases an inadequate description as it has been shown that this edge bending of the magnetization can lead to the breaking of magnetic symmetry at the vertices and to a highly degenerate ground state with finite zero-point entropy [124], similar to that of the pyrochlore spin ices. To take the edge bending into account in theoretical

models, the nanomagnet has at least to be divided into three segments (three-spin model), as shown in Figure 4.2 (a) and (b). It has been shown that edge states have two energetically stable configurations called “S”- and “C”-states [126]. In both of these stable states the net magnetization in the middle segment is pointing along the long axes of the nanomagnet, while the local magnetization at both ends is bending in different directions. Figure 4.2 (a) shows the “S”-state. In the S”-state the magnetization at the edges is pointing in the same direction, leading to an “S”-like magnetization distribution within a single nanomagnet. (b), Shows the “C”-state. In the “C”-state the magnetization at the two edges is pointing in different directions, leading to a C-like distribution of the magnetization in a single nanomagnet.

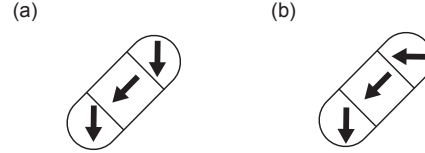


Figure 4.2. | Two energetically equivalent configuration of edge states exist: (a) shows the “S”- and in (b) the “C”-state [126].

As a consequence of this bending of the magnetization, artificial square ice can undergo a transition from a twofold degenerate ground state to a broken-symmetry, highly degenerate ground state induced by increasing the film thickness of the nanomagnets, increasing the saturation magnetization or decreasing the lattice constant [124].

4.2. “Chiral ice” - an artificial spin ice system

The “chiral ice” consists of a two-dimensional arrangement of lithographically patterned ferromagnetic nanomagnets. Figure 4.3 (a) shows schematic the arrangement of the nanomagnets of a “chiral ice” as a finite array. In this work, nanomagnets consist of Py ($\text{Ni}_{83}\text{Fe}_{17}$) and the length and width of each element is $1.55 \mu\text{m}$ and 560 nm , respectively. The centre-to-centre distance of neighboring nanomagnets is $1.5 \mu\text{m}$, which is the lattice constant. Each vertex consists of four nanomagnets oriented at an angle of 90° with respect to each other [121], as shown in figure 4.3 (b) in the form of a single vertex. On this figure, in the upper part, the general direction of the magnetization within each nanomagnet is schematically represented by a black arrow and corresponds to a single-spin representation. In the lower part the magnetization of the nanomagnets are shown using the more realistic three-spin-model. In both models the ground state is depicted, where the ice rules are obeyed. The vertex magnetization M_v is the sum of the magnetization M of the individual nanomagnets at a vertex and is represented by a green arrow, visible in the center of the vertices and points in both cases in the same direction. Figure 4.3 (c) shows a SEM image taken from a segment of the measured chiral artificial spin ice sample. The SEM image shows that each nanomagnet has a homogeneous surface and that the general shape displays a high quality. Both are important factors to avoid a multi-domain state, which is not desirable in a spin ice system.

It is the geometrical arrangement of the nanomagnets, which defines the chiral ice. Chirality is a universal property present in nature and exists in a variety of systems. It exists in three-dimensional systems, like biomolecules whose function is defined by their handedness, but also in two-dimensional systems, such as the chiral ice. Chirality, in general, illustrates the concepts

of symmetry in two dimensions. The most recognized example of chirality are human hands, where the left-hand is a non-superimposable mirror image of the right hand. This means that it is impossible for all major features of both hands to coincide across all axes, no matter how the two hands are oriented. In two dimensions chirality means that no translation or rotation within the plane can bring an object into coincidence with its mirror image. Figure 4.3 (a) shows a finite array of the chiral ice. An infinite array would be achiral, but the finite system remains chiral because of its boundaries [122]. It follows that the edges of the array and the two-dimensional character, due to the shape anisotropy induced by the low thickness, which ensures that the magnetization is confined to the plane of the sample [121], are together responsible for the fact that the finite array is chiral. Other well-known artificial spin ice geometries, like square ice [114] or kagome spin ice [123] are non-chiral.

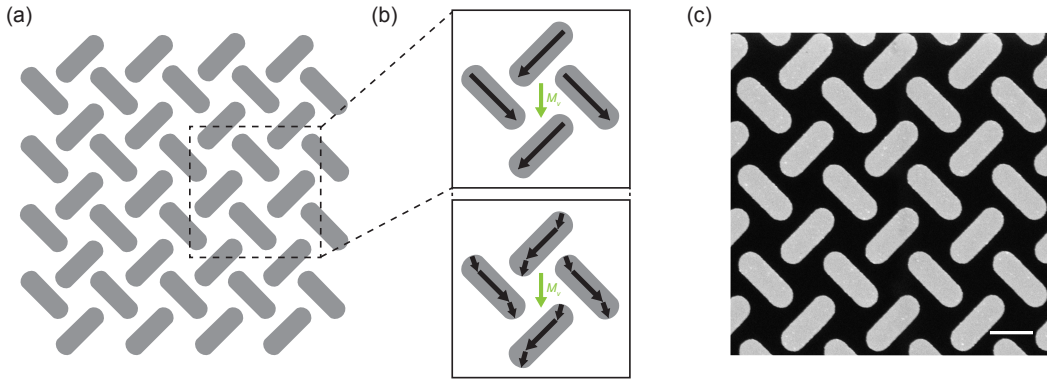


Figure 4.3. | (a) Schematic representation of a finite array of the chiral ice system. (b) Schematic block diagram of a single vertex, where four nanomagnets are patterned at an angle of 90° with respect to each other. The general direction of the magnetization of the nanomagnets are drawn in the upper part as single black arrows, which corresponds to the conventional Ising-like macrospin approximation. Below is the more realistic three-spin-model shown. In both models the ice rules are obeyed. The direction of the net vertex magnetization M_v is drawn as a green arrow in the center of the vertex and shows in both cases in the same direction. (c), Shows a SEM image from a segment of the measured chiral ice sample. The homogeneous surface of each nanomagnet is visible. The nanomagnets consist of Py ($\text{Ni}_{83}\text{Fe}_{17}$) and the length and width of each is $1.55 \mu\text{m}$, and 560 nm , respectively, with a lattice constant of $1.5 \mu\text{m}$ (centre-to-centre distance of neighboring nanomagnets). The scale bar represents $1 \mu\text{m}$.

Recently, experimental measurements using PEEM at room temperature have imaged the thermally-induced relaxation of such a system following saturation by an external field. The measurements show a collective rotation of the average magnetization in a unique sense, which means that energy is converted into unidirectional dynamics, thus defining a ratchet. Micromagnetic simulations showed that the collective rotation is driven by the topology of the magnetostatic field at the edges of the array [121]. Using PEEM one is able to map the magnetic configurations close to zero field. Our scanning SQUID-on-tip technique on the other hand is a suitable method to image the static magnetic configuration of an artificial spin ice, while, for instance, an in-plane magnetic field is applied. In the PEEM measurements no edge bending was observed. The reason is that the studied nanomagnets of the chiral ice were smaller and thinner (about 2 nm), therefore no edge bending occurs due to the shape anisotropy. In our case the nanomagnets are larger and thicker. Another difference is that during the PEEM measurements the system was thermally active, while the scanning SQUID-on-tip experiment is performed at 4.2 K . The mentioned differences this make it almost impossible to compare

the two experiments. We have investigated this geometry owing its particular in-plane stray field pattern, which has only been simulated in Ref. [121]. We have investigated this pattern because its field-induced behavior was unexplored and its (in-plane) stray field pattern had been predicted by micromagnetic simulations, but not directly measured. Furthermore, given to the size of the nanomagnets, we expect edge bending to play an important role in the static configuration as well as in the behavior of the magnetization. With the scanning SQUID-on-tip we are able to measure experimentally its effects in the magnetic stray field of the spin ice system. These measurements allow to get a deeper understanding of the complex dipolar coupling in this spin ice system.

Figure 4.4 (a) shows one possible configuration of the magnetization in magnetostatically coupled nanomagnets arranged in a square spin ice geometry due to the edge bending. The small arrows at the edges of the depicted nanomagnets represent the computed local magnetization. The direction of the magnetization (M) at the edges in the x-y-plane, is plotted using brown for a positive and blue for a negative direction of the magnetization. The axially aligned magnetization within the bulk of the nanomagnets is shown as a black arrow. Figure 4.4 (b) shows the equivalent possible configuration of the magnetization in strongly magnetostatically coupled nanomagnets arranged in a chiral spin ice geometry. The direction of the net vertex magnetization M_v is drawn as a green arrow in the center of the vertex. In both cases the ice rules are obeyed. In the case of the chiral ice the ground state is “ferromagnetic”, as opposed to the “antiferromagnetic” ground state of the square ice [128] - the ice rules are obeyed in both cases.

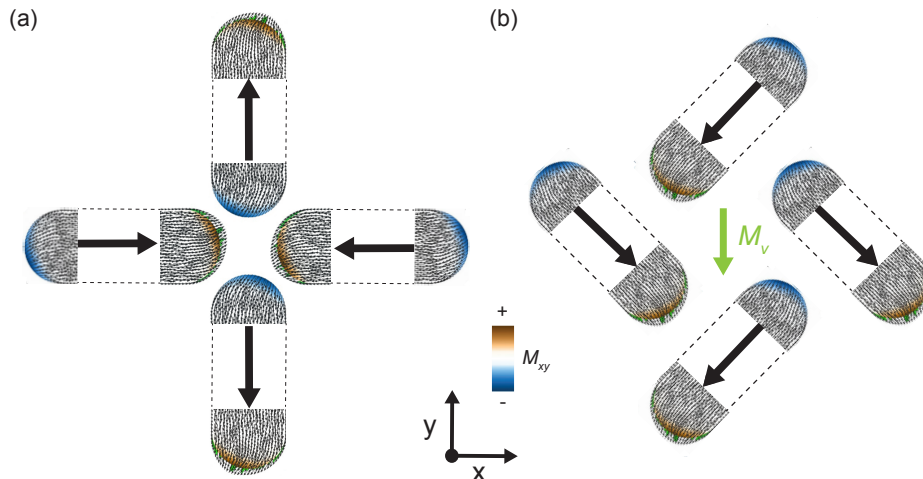


Figure 4.4. | (a) shows one possible configuration of the magnetization in magnetostatically coupled nanomagnets arranged in a square ice geometry due to the edge bending. The small arrows represent the computed local magnetization, while the large black arrows between the edges show the uniform direction of the magnetization. (b), Shows the equivalent configuration of a chiral spin ice. The net vertex magnetization M_v is drawn as a green arrow in the center of the vertex. The direction of the magnetization (M) at the edges in the x-y-plane is plotted using brown for a positive and blue for a negative direction of the magnetization. In (a) the ground state is „antiferromagnetic“, while in (b) the ground state is „ferromagnetic“.

4.3. Fabrication of a chiral artificial spin ice system

For the scanning SQUID-on-tip experiment four $500 \mu\text{m} \times 500 \mu\text{m}$ arrays consisting of Py ($\text{Ni}_{83}\text{Fe}_{17}$) nanomagnets arranged in the geometry of a chiral artificial spin ice system were fabricated in the center of a non-magnetic Si (100) substrate using electron beam lithography combined with thermal evaporation at room temperature and a base pressure of $2 \cdot 10^{-6}$ mbar followed by lift-off. The nanomagnets consist of Py ($\text{Ni}_{83}\text{Fe}_{17}$) and the length and width of each nanomagnet are $1.55 \mu\text{m}$ and 560 nm , respectively, and with a lattice constant of $1.5 \mu\text{m}$ (centre-to-centre distance of neighbouring nanomagnets). To prevent oxidation, a 2 nm thick aluminum capping layer was evaporated on top of the Py. Atomic force microscopy (AFM) was used to measure the thicknesses of the arrays, which is of 8 nm on average across the entire array, without taking the capping layer into account.

To image the magnetic configuration of a chiral ice system using the scanning SQUID-on-tip technique one limiting factor was given by the spatial resolution. The SQUID-on-tip has a spatial resolution given by the effective tip diameter and ranges usually from $50 - 250 \text{ nm}$. Due to this limitation the nanomagnets were substantially larger as compared to the published PEEM experiments [121]. Despite it is important that the nanomagnets are still in a single-domain state. To find an ideal size, we designed finite arrays with nanomagnets having different lateral dimension but the same aspect ratios and imaged the magnetic configurations using x-ray photoemission electron microscopy (XPEEM) [8], employing x-ray magnetic circular dichroism (XMCD) [14]. These measurements showed that the limit, when nanomagnets are still in a single-domain state, is given for a length and width not greater than $1.55 \mu\text{m}$ and 560 nm , respectively. XPEEM measurements with nanomagnets of larger dimensions showed that some of the nanomagnets were in a multi-domain state and thus not suitable for a spin ice system.

5. Imaging of a Chiral Artificial Spin Ice System

This chapter describes measurements of the magnetic stray field distribution of the “chiral ice” as a function of different applied magnetic in-plane and out-of-plane fields. The experiment is performed at cryogenic temperature and for the magnetic imaging the scanning SQUID-on-tip technique is used. Compared to PEEM, the strength of these measurements lies in the fact that the scanning SQUID-on-tip technique allows to image in a field and it has access to the magnetic stray field, which for this system is predicted to be complex and non-trivially connected to magnetization dynamics. The measured stray field distributions provide insight the influence of external applied magnetic fields on the system. To interpret the details of the measurements, micromagnetic simulations are performed to get a deeper understanding of how the magnetization behaves as a function of applied in-plane magnetic field strength. The measured stray field distributions at different magnetic field strengths are very well described by the micromagnetic simulations of the expected distributions. In particular, the simulations elucidate the stray field distribution at zero field. Indeed, the measurements show that successive regions of alternating stray field intensity are separated by a boundary that displays a meander pattern. The simulations demonstrate that this pronounced pattern is due to the bending of the magnetization at the edges of the nanostructures. The meander pattern is almost inexistent assuming simulations with uniformly magnetized nanomagnets. The presented measurements have shown that the SQUID-on-tip technique is sensitive enough to image the effects of the edge bending of the magnetization on the stray field pattern along the z -direction. These observations demonstrate that the number of degrees of freedom in artificial spin ice is in fact much larger than captured in dipolar models. Such degrees of freedom may find use in reprogrammable magnonic crystals, where the in-plane magnetic field has been shown to allow tuning of the band frequency.

5.1. Defining suitable working points for the magnetic reversal experiment

In order to map quantitatively the magnetic stray field distribution $B_z(x, y)$ of the chiral ice, as a function of applied in-plane- ($\mu_0 H_x$) and out-of-plane ($\mu_0 H_z$) fields, under the use of scanning SQUID-on-tip technique, one has to define suitable working points for all different magnetic field strengths. Figure 5.1 (a) shows a schematic drawing of the SQUID-on-tip experiment. The position of the SQUID-on-tip is fixed above the sample during the experiment. Underneath the SQUID-on-tip, the chiral ice is located in close proximity to a magnetic field sensor. The sample is mounted on top of a xyz -positioner. By scanning the sample in xy -direction, the z -component of the sample magnetic stray field distribution $B_z(x, y)$ can be measured.

The following criteria are applied to define suitable working points: The working points need to be stable during the entire scanning process, which means that the flux-locked feedback loop

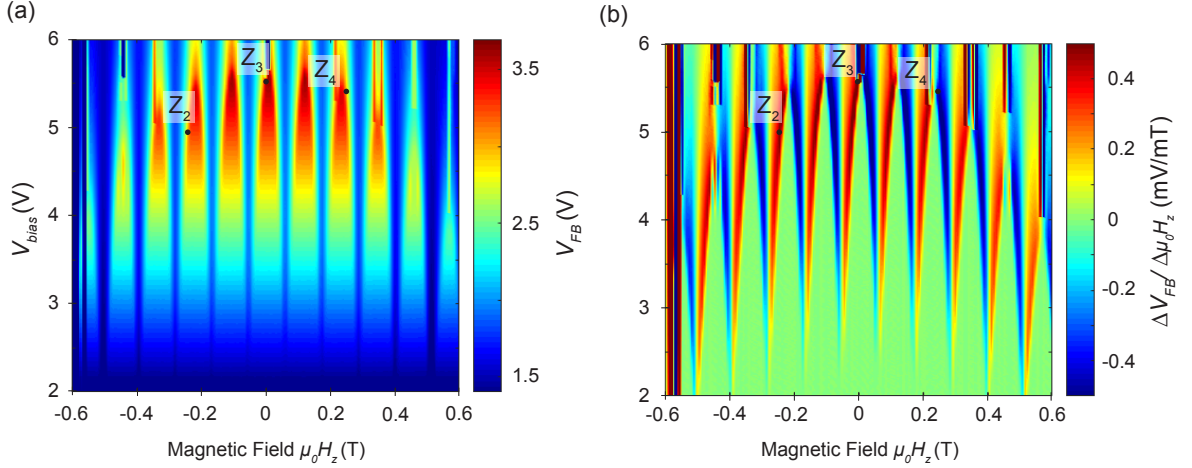


Figure 5.2. | (a) Current through the Pb SQUID-on-tip (colour coded) versus input voltage V_{bias} and applied magnetic field $\mu_0 H_z$ showing quantum interference oscillations with a period corresponding to an effective SQUID-on-tip diameter of $d_{\text{tip}} = 147\text{nm}$. (b), The to (a) corresponding voltage-to-flux ($V - \Phi$) SQUID transfer function of the SQUID-on-tip. The black circles show the defined SQUID-on-tip working points for the z -field reversal measurements. The working points have the following values: \mathbf{Z}_2 : $\mu_0 H_z = -250\text{ mT} / V_{\text{bias}} = 4.89\text{ V}$, \mathbf{Z}_3 : $\mu_0 H_z = -6\text{ mT} / V_{\text{bias}} = 5.475\text{ V}$, \mathbf{Z}_4 : $\mu_0 H_z = 250\text{ mT} / V_{\text{bias}} = 5.43\text{ V}$. Two working points are located outside the measuring range, with the following values: \mathbf{Z}_1 : $\mu_0 H_z = -684\text{ mT} / V_{\text{bias}} = 2.835\text{ V}$ and \mathbf{Z}_5 : $\mu_0 H_z = 708\text{ mT} / V_{\text{bias}} = 2.79\text{ V}$. The in (b) visible dark red and blue strips are regions where the FFL electronics lost for a short time the lock. The regions also correspond to the irregularities visible in (a) at the same positions.

reduces its normal component, which leads to a reduced critical current. Another effect is that the application of a magnetic field in the same direction as the superconducting loop and the Josephson junctions induces a phase shift in the supercurrent, thereby inducing a variation in the critical current [46, 47]. Further contributions, which causes a shift of the transfer function, are a not perfectly aligned SQUID-on-tip with respect to the in-plane field direction, plus that the projection of the x - and z -magnetic field components couples into the superconducting loop. Consequently, it follows, that for the working points one has to do an IVC measurement for all different applied in-plane field strengths. First one has to ramp the in-plane field to a desired strength and then measure the out-of-plane field dependency on the critical current flowing through the Pb SQUID-on-tip. Figure 5.3 shows three examples of measured voltage-to-flux ($V - \Phi$) SQUID transfer functions at various applied in-plane magnetic field strengths. In those examples the strong shift of the transfer functions and the corresponding change of the position of the minimum and maximum value of the critical current, depending on the in-plane magnetic field strength due to the above-mentioned factors, are visible.

Further it turns out that the IVC looks slightly different for positive and negative applied bias voltages. If the applied in-plane field is negative also the applied bias voltage should have a negative sign, because the sensitive region is mostly broader and shows therefore the better IVC to define a stable working point. This magnetic field dependency depends of course strongly on the respective SQUID-on-tip.

After characterization, the next step is to approach the sample in close proximity to the SQUID-on-tip in the microscope, without damaging the magnetic field sensor. To do so, the sample moves in z -direction as well as x -direction to increase the probability that magnetic flux, originating from the sample, is measured by the SQUID, at a small enough distance, before the

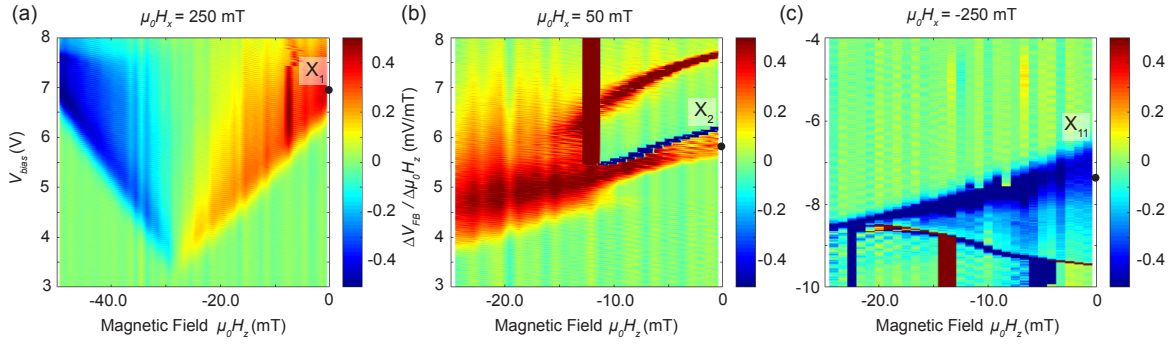


Figure 5.3. | Voltage-to-flux ($V - \Phi$) SQUID transfer function at different applied in-plane magnetic field strengths ($\mu_0 H_x$). The transfer functions show the strong influence of the applied in-plane field on the current-to-voltage characteristics (IVC). Characteristic working points are labeled with X_1 , X_2 and X_{11} and shown as black dots in (a,c). The exact values of the shown characteristic working points in (a,c) are listed below: \mathbf{X}_1 : $\mu_0 H_z = 0$ T / $V_{\text{bias}} = 6.88$ V, \mathbf{X}_2 : $\mu_0 H_z = -0.3$ mT / $V_{\text{bias}} = 5.48$ V, \mathbf{X}_{11} : $\mu_0 H_z = -0.1$ mT / $V_{\text{bias}} = -7.2$ V. In (b) a dark red line is visible in the center of the image, there the SSAA lost the lock for some sweeps.

sensor touches the sample. To ensure that the largest possible stray field can be measured by the nanomagnets, the working point of the SQUID-on-tip was used with an applied field strength of $\mu_0 H_z = 708$ mT (Z_5). At such a high magnetic field, the magnetization of the nanomagnets point out-of-plane, because the field strength is close to the saturation magnetization, which was measured to be $\mu_0 M_s = 0.8 \pm 0.1$ T for Py thin film coated nanotubes [64], thereby helping to increase the probability of a successful approach. Figure 5.4 (b) shows the measured z -component of the magnetic stray field (B_z) as a function of time during the approach of the sample towards the SQUID-on-tip. Plotted is the increasing amount of magnetic flux, coupling into the SQUID, originating from the nanomagnets of the chiral ice located underneath the magnetic field sensor. To avoid damage to the SQUID-on-tip, the movement is stopped, when a threshold value for the magnetic flux is reached. Subsequently, the approach is carried out manually in small steps to prevent to damage the magnetic field sensor.

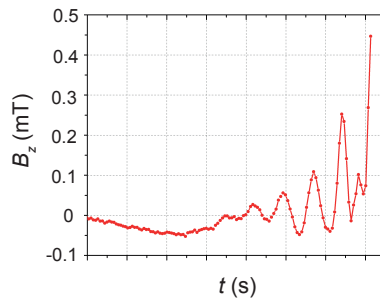


Figure 5.4. | Shows the measured z -component of the magnetic stray field (B_z) as a function of time during the approach of the sample towards the SQUID-on-tip. During the approach the sample is moved in z - as well as x -direction to increase the probability that magnetic flux from the sample couples into the SQUID at small enough tip-sample separations. Visible is the increasing amount of magnetic flux coupling into the SQUID coming from the nanomagnets of the chiral ice, which is located underneath the magnetic field sensor, till the set threshold is reached and the movement is stopped. For safety, the sample returns to its original position.

5.2. Magnetic reversal measurements with applied out-of-plane magnetic fields

During the approach of the SQUID-on-tip, a magnetic field of $\mu_0 H_z = 708$ mT was applied to the chiral ice. After successful approach, the magnetic stray field distribution $B_z(x, y)$, shown in Figure 5.5 (a), was measured at the same field strength using the scanning SQUID-on-tip technique. The SQUID-on-tip is sensitive to the z -field component of the magnetic stray field originating from the sample. The obtained images include information about the stray field distribution at a specific distance above the nanomagnets. In the following chapter, $\mu_0 H_{x,z}$ indicates the externally applied magnetic field used to bias the device or to change the magnetic configuration of the chiral ice, while $B_z(x, y)$ indicates the measured stray field distribution of the z -component due to the samples magnetization, as a function of the SQUID-on-tip position.

The measured stray field distribution in (a) shows, that the applied magnetic field causes all magnetic moments in the nanomagnets to point out-of-plane, as a result, the position of the nanomagnets underneath the scanning SQUID-on-tip sensor can be determined.

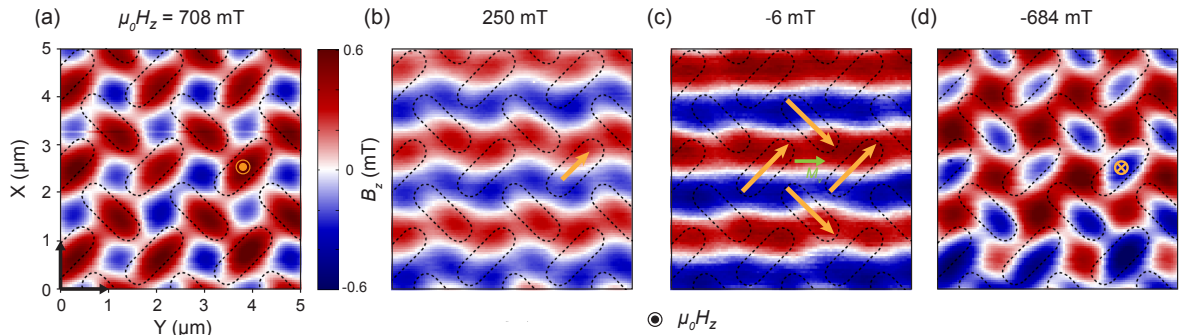


Figure 5.5. | (a,d), Shows a series of measured magnetic stray field distributions $B_z(x, y)$ of the studied chiral ice at different applied out-of-plane magnetic fields $\mu_0 H_z$. The direction of the $\mu_0 H_z$ is depicted as a black arrow below image (c). The dashed outlines indicate the position of the nanomagnets on top of the non-magnetic Si-substrate. The orange arrow in (a), (b) and (d) located in the centre of one nanomagnet depicts the general orientation of the magnetization represented as single-spin. In (c) four orange arrows at one vertex shows that the chiral ice is in a ground state, obeying the „ice rules.“ The net vertex magnetization (M_v) is depicted as a bright green arrow in the center of the vertex. The net vertex magnetization points in the same direction as the visible stray field lines in the magnetic stray field distribution. The color bar of (a) also corresponds to that of (b), (c) and (d).

This because if all magnetic moments point out-of-plane, the maximum of the stray field in the measured magnetic stray field distribution $B_z(x, y)$ should occur in the center of each nanomagnet, which is visible in figure 5.5 (a). There the maxima of the DC signal (red) are located in the centers of the nanomagnets and the minima (blue) between four neighboring nanomagnets, in the center of each single vertex. It is also visible that the stray field becomes weaker towards the ends of the nanomagnets. To understand this, a simple picture can be used, in which a nanomagnet is treated as magnetic dipole. In a magnetic dipole the magnetic stray field in z -direction is maximized in the center and decreases, if one goes far enough from the center. However, due to dipolar coupling the obtained magnetic stray field distribution of the chiral ice is much more complex than this simple picture, but it gives a rough idea.

The position of the nanomagnets are indicated as dashed outlines, each superimposed to the measured stray field distributions $B_z(x, y)$ in (a) - (d).

A reduction of the applied magnetic field strength to $\mu_0 M_z = 250$ mT causes a decrease in the stray field strength in z -direction as shown in figure 5.5 (b). The reduced applied magnetic field results in the rotation of the magnetization in the plane of the nanomagnets and along the easy axes due to the shape anisotropy. This leads to a net magnetization illustrated by the orange arrow in figure 5.5 (b), which is pointing at an angle with respect to the $x - y$ -plane, therefore the orange arrow is drawn shorter. Close to zero field, at $\mu_0 H_z = -6$ mT, the chiral ice ends up in the ground state, obeying the ice rules as shown in (c). The net vertex magnetization (M_v), depicted as a bright green arrow in the center of the vertex in (c), is aligned along the length of the visible stray field pattern. Reducing the applied magnetic field to $\mu_0 H_z = -684$ mT causes the magnetic moments to point down, as shown in figure 5.5 (d). There the minimums of the DC signal (blue) are located in the centers of the nanomagnets and the maximums (blue) between four neighboring nanomagnets, in the center of each single vertex. To get the full hysteresis the magnetic field was first reduced to $\mu_0 H_z = -708$ mT, before measurements were performed again at lower magnetic field strength. To complete the hysteresis loop the opposite direction of all measured stray field distributions $B_z(x, y)$ are shown in detail in Appendix E.2.

Figure 5.6 (a) and (b) show the similar working point of the scanning SQUID-on-tip at $\mu_0 M_z = -6$ mT, but the previously applied out-of-plane saturation magnetic field pointed in opposite direction. In both cases the chiral ice each ends up in a ground state, obeying the „ice rules“, but the net vertex magnetization is pointing in opposite direction, depending on the previous applied magnetic field direction. The reason for this observation will be described in detail in section 5.4.

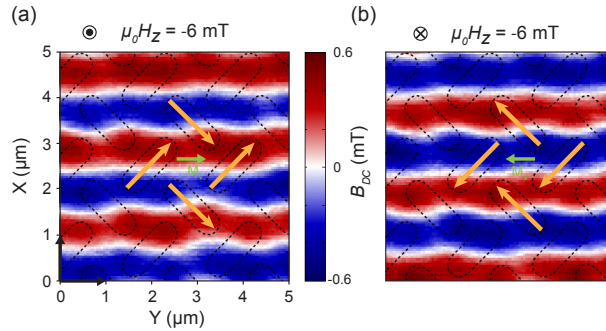


Figure 5.6. | (a) and (b) shows the measured magnetic stray field distribution $B_z(x, y)$ each at $\mu_0 H_z = -6$ mT, but the previously applied out-of-plane saturation magnetic field pointed in opposite directions. In (a) a magnetic field strength of $\mu_0 H_z = 708$ mT and in (b) of $\mu_0 H_z = -708$ mT was previous applied to the chiral ice to saturate the sample, before taking the images at $\mu_0 H_z = -6$ mT. The direction is thereby each depicted as black arrows, pointing out-of plane. Visible is that the chiral ice close to zero field each ends up in a ground state, obeying the „ice rules“, but net vertex magnetization, depicted with a green arrow, is pointing in opposite direction depending on the previous applied magnetic field direction.

5.3. Magnetic reversal measurements with applied in-plane magnetic fields

A similar reversal experiment was carried out, but instead of an out-of-plane magnetic field as in the previous section, a series of different in-plane magnetic fields are applied to the chiral ice under the same conditions. Figure 5.7 (a) shows a scanning SQUID-on-tip image of the magnetic stray field distribution $B_z(x, y)$, taken with a constantly applied in-plane field of $\mu_0 H_x = 250$ mT, which refers to working point X₁ discussed in the previous section 5.1. The field of view is the same as in section 5.2, therefore the position of the nanomagnets in figure 5.7 is already known and again indicated as dashed outlines from (a,d). In (a) the general orientation of the magnetization in the nanostructures are schematically indicated by orange arrows deduced from the measured stray field distribution $B_z(x, y)$, they point in (a) in the same direction as the applied field.

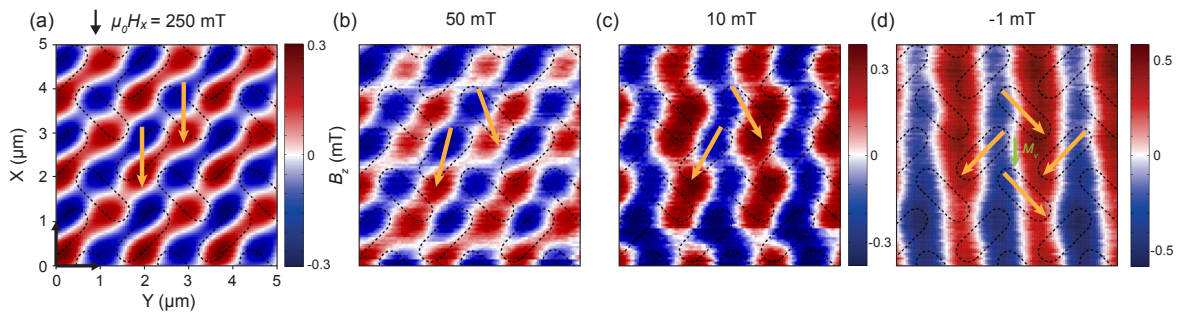


Figure 5.7. | (a,d), Shows a series of measured magnetic stray field distributions $B_z(x, y)$ of the studied chiral ice at different in-plane magnetic fields ($\mu_0 H_x$). The direction of $\mu_0 H_x$ is shown by a black arrow in (a). In the following for each image the applied out-of-plane magnetic field strength is given, which allowed us to measure in the most sensitive working point: (a) $\mu_0 H_z = 0$, (b) $\mu_0 H_z = -0.3$ mT, (c) $\mu_0 H_z = -0.25$ mT, (d) $\mu_0 H_z = -0.3$ mT. The dashed outlines indicate the positions of the nanomagnets on top of the non-magnetic Si substrate. In (a) - (c) orange arrows located in the centre of two nanomagnets depict the general direction of the average magnetization in the nanostructures deduced from the measured stray field distributions. In (d) four orange arrows indicate that the chiral ice is in a ground state obeying the „ice rules.“ The net vertex magnetization (M_v) is depicted as a bright green arrow in the center of the vertex. The color bar of (a) also corresponds to that of (b).

Reducing the in-plane field to $\mu_0 H_x = 50$ mT, the magnetization starts to orient itself along the easy axes of the nanomagnets due to the shape anisotropy as shown in (b). Reducing further the in-plane field allows the magnetization to align even more with the easy axis of the nanostructures as shown in (c). In zero field shown in (d), the system is in the ground state, with the magnetization at each vertex forming a two in-two out state. The magnetic stray field pattern is characterized by regular regions of alternating intensities. The boundary between these regions displays a meander pattern. We find that this pattern is due to the bending of the magnetization at the edges of the nanomagnets (see section 5.4) and therefore represents an indirect measurement of the edge bending.

In general, the quality of the individual scanning SQUID-on-tip images is strongly dependent on the quality of the working point in terms of the specific sensitivity and noise level. The biggest difference in terms of the quality of the scanning SQUID-on-tip images is visible in figure 5.7 (a) compared to (b). Both obtained magnetic field distributions $B_z(x, y)$ are shown in the same field of view, but the measured scanning SQUID-on-tip image in (b) have a much higher

noise level compared to (a). The reason is that the sensitivity $\partial B_z/\partial V_{\text{SQUID}}$ of the working point in (b) is lower, while the electronic noise is the same in both cases. This is also visible in the measured IVC and the corresponding voltage-to-flux ($V - \Phi$) SQUID transfer functions in figure 5.3 (a) and (b). In the series of the measured magnetic stray field distributions an increase of the magnetic stray field strength towards zero applied magnetic field is observed. The measured magnetic stray field strength changes from $B_z = \pm 0.3$ mT in figure 5.7 (a) and (b) to higher magnitude in (c) of $B_z = \pm 0.35$ mT and (d) of $B_z = \pm 0.55$ mT at an applied magnetic field close to zero. The reason for the observed increase is the different distribution of the magnetic charges in the system: these gradually become more localized at the nanomagnet edges as the external field magnitude decreases, leading to a more focused stray field pattern with larger local intensities, which leads to a stronger magnetic stray field in z -direction. It is the ground state ordering of the chiral ice, which is responsible for the observed alternating stray field distribution shown in figure 5.7 (d).

A further reduction of the applied magnetic field strength, initially does not change significantly the stray field distribution as shown in figure 5.8 at $\mu_0 H_x = -5$ mT. The system remains in the ground state until the switching field is reached. The switching field is dependent on the magnetic material and the geometry of the nanomagnet lattice and is found to be ± 10 mT in the studied chiral ice, depending on the previous applied magnetic field direction. At the switching field a complex stray field distribution was observed as shown in negative direction in (b).

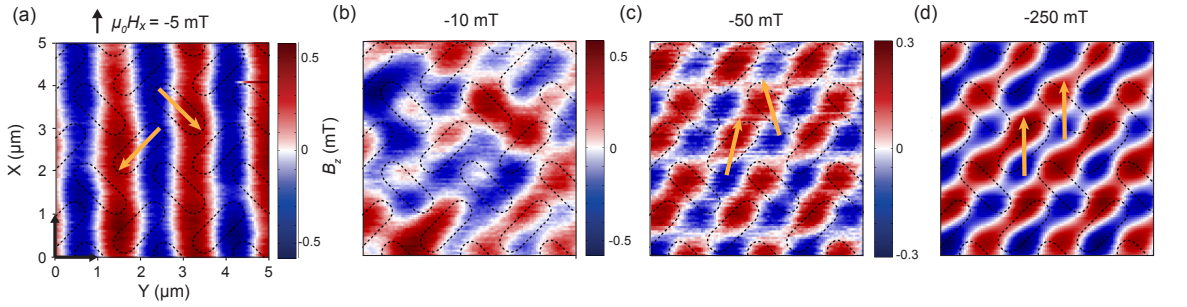


Figure 5.8. | (a,d), Shows a series of measured magnetic stray field distributions $B_z(x, y)$ of the studied chiral ice at different negative in-plane magnetic fields ($\mu_0 H_x$). The direction of $\mu_0 H_x$ is depicted as a black arrow in (a). In the following for each image the applied out-of-plane magnetic field strength is given, which allowed us to measure in the most sensitive working point: (a) $\mu_0 H_z = -0.3$ mT, (b) $\mu_0 H_z = -0.8$ mT, (c) $\mu_0 H_z = -0.5$ mT, (d) $\mu_0 H_z = -0.1$ mT. The dashed outlines indicate the positions of the Py nanomagnets on top of the non-magnetic Si substrate. In (a),(c) and (d) the orange arrows located in the centre of two nanomagnets depict the orientation of the single Ising-spins. The color bar of (c) also corresponds to that of (d).

This distribution is likely due to the breakup up of the magnetic structure into multiple domains. The obtained stray field distribution at $\mu_0 H_x = -50$ mT is similar to the one found at 50 mT in figure 5.8 (b), only with reversed field intensities. A further reduction of the in-plane field to $\mu_0 H_x = -250$ mT causes the magnetization to align with the external field, in the opposite direction with respect to figure 5.7 (a). To complete the hysteresis loop, the opposite direction of the measured stray field distributions $B_z(x, y)$ is shown in detail in Appendix E.1.

5.4. Micromagnetic Simulations of the in-plane field experiment

To interpret the details of the measurements, micromagnetic simulations are performed to get a deeper understanding of how the magnetization behaves as a function of applied in-plane magnetic field strengths. The fully three-dimensional micromagnetic simulations are based on a hybrid finite-element/boundary-element method, which has been carried out on a system of 144 nanomagnets, each with lateral dimensions of 800 x 290 nm and 10 nm thick. The simulated size corresponds to approximately 50% of the lateral size of the measured nanomagnets, keeping the thickness as in the experiments. The structure was discretized using a tetrahedral mesh with an average cell size corresponding to an equivalent cube with 3.9 nm side length. The following material parameters for Permalloy were used: saturation polarization $\mu_0 M_s = 1$ T, exchange constant $A_{\text{ex}} = 1.3 \cdot 10^{-11}$ J/m and zero magnetocrystalline anisotropy $K = 0$. The dipolar exchange length Δd is calculated using equation 3.2 and is 5.1 μm , which is larger than the mesh.

The micromagnetic simulations allowed us to determine the distance between the probe and the sample. To do so, a simulated magnetic stray field distribution $B_z^{\text{sim}}(x, y)$ was compared with its experimental counterpart $B_z(x, y)$, until the magnetic field strength coincided. The pattern obtained, was somewhat different from the experiment. From this we concluded, that also a tilt of the substrate with respect to the plane, must be taken into account. In order to obtain the most accurate value of the tilt, the micromagnetic simulations were carried out with different angles and then compared with its experimental counterpart, until the magnetic field strength as well as the pattern were consistent. Through this comparison the probe-to-sample distance and the tilt were determined to be approximately 450 nm and 15°, respectively. It is assumed that the distance between the probe and sample and the tilt remains the same throughout the whole experiment. A copper braid is most likely responsible for the tilt of the substrate with respect to the plane, mounted on the sides of the microscope. An image of the home-built scanning microscope is shown in Appendix C.1, where the copper braids are visible. These copper braids have the function to connect thermally the top and the bottom of the microscope. One copper braid was a bit longer on one side and caused thereby the rather large tilt. Consequently, in the simulated magnetic stray field distributions $B_z^{\text{sim}}(x, y)$, both the probe-to-sample distance of 450 nm and the tilt of 15° are always considered.

The micromagnetic simulations are performed by saturating the sample with the strongest field ($\mu_0 H_x = 250$ mT), obtaining the equilibrium configuration of the magnetization in that field, and then decreasing the field to a lower value (for example $\mu_0 H_x = 50$ mT) and calculating the equilibrium state. For the scanning SQUID-on-tip experiment, additionally a small out-of-plane magnetic field is applied, for all applied in-plane fields. This additional magnetic field ensures that the working point of the SQUID-on-tip is in the most sensitive region, as described in 5.1. Those small magnetic fields, which point in z -direction, are also considered in the micromagnetic simulations.

Figure 5.9 (a,d) shows a series of simulations of the magnetic field distribution $B_z^{\text{sim}}(x, y)$, considering the same region of the array and the same applied in-plane magnetic fields. The used working points are discussed in section 5.3 and the experimental images are shown in figure 5.7 (a,d). Like in the experiment, the micromagnetic simulations show an increase of the magnetic stray field magnitude around zero field. Figure 5.9 (e,h) shows the detailed magnetic configurations of four nanomagnets at a single vertex. These configurations correspond to the simulated magnetic field distributions $B_z^{\text{sim}}(x, y)$ shown in (a,d). In (a,d) the orange arrows depict the general direction of the average magnetization in the nanostructures deduced from

the simulated magnetic stray field distributions. In (d) four orange arrows at one vertex show that the chiral ice is in the ground state obeying the “ice rules.” All of the nanomagnets are in an “S”-state. The net vertex magnetization (M_v) is depicted as a bright green arrow in the center of the vertex in (d).

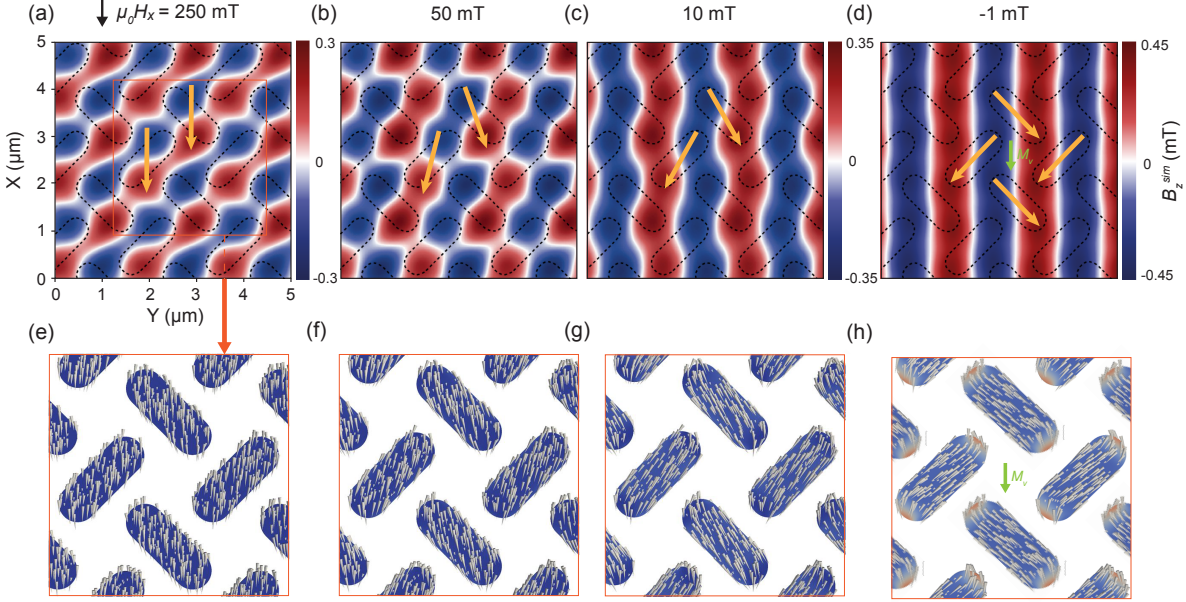


Figure 5.9. | (a,d), Shows micromagnetic simulations of the magnetic stray field distribution $B_z^{sim}(x, y)$ of the studied “chiral ice” at different in-plane magnetic fields $\mu_0 H_x$. The values of the in-plane fields correspond to the ones used in the experiment shown in figure 5.7 and described in section 5.3. In (a) - (c) orange arrows located in the centre of two nanomagnets depict the general direction of the average magnetization in the nanostructures deduced from the simulated stray field distributions $B_z^{sim}(x, y)$. In (d) four orange arrows indicate that the “chiral ice” is in a ground state obeying the ice rules. The net vertex magnetization (M_v) is depicted as a bright green arrow in the center of the vertex. The color bar of (a) also corresponds to that of (b). (e,h) shows the simulated magnetic configuration of a single vertex. The section corresponds to that of the dark orange square in (a). The small arrows represent the computed local magnetization of the nanomagnets. Each simulated magnetic configuration from (e,h) corresponds to the simulated magnetic stray field distribution $B_z^{sim}(x, y)$ from (a,d). The probe-to-sample distance is 450 nm and a tilt of 15° is considered.

The direction of the magnetization in the center (bulk-like region) of the nanostructures rotates as the external field is decreased and finally the magnetization is aligned along the easy axes of the nanomagnets in zero field. In addition, at the edges of the nanomagnets, the simulations show that the magnetization slightly bends at first, finally resulting in a strong bending at zero field.

In the detailed magnetic configuration of four nanomagnets at a single vertex in figure 5.9 (h), it is visible that at the edges the magnetization bends locally. The corresponding magnetic stray field pattern, shown in (d), is characterized by regular regions of alternating intensities. The boundary between these regions displays a slight meander pattern. To prove that this meander pattern has its origin in the edge bending, we performed micromagnetic simulations, which assume a uniform magnetization of the nanomagnets. Figure 5.10 (a) shows the simulated magnetic stray field distribution $B_z^{sim}(x, y)$ which contains edge bending. Figure 5.10 (b) shows the same area of the array, but assuming a uniform magnetization of the nanomagnets. The simulated magnetic stray field distribution assuming a uniform

magnetization is characterized by regular regions of alternating intensities, where no meander pattern is visible. In the simulated magnetic stray field distribution, which contains edge bending, a meander pattern starts to emerge. In figure 5.10 (c) additional the position of the nanomagnets is included. The meander pattern is caused by the fact that the stray field maximum and minimum shifts slightly away from the center due to the edge bending. In (c) a three-spin model (orange arrows), which was introduced in section 4.1, is used to describe more precisely the orientation of the magnetization. In the case of a uniform magnetization in (d), a single-spin is sufficient.

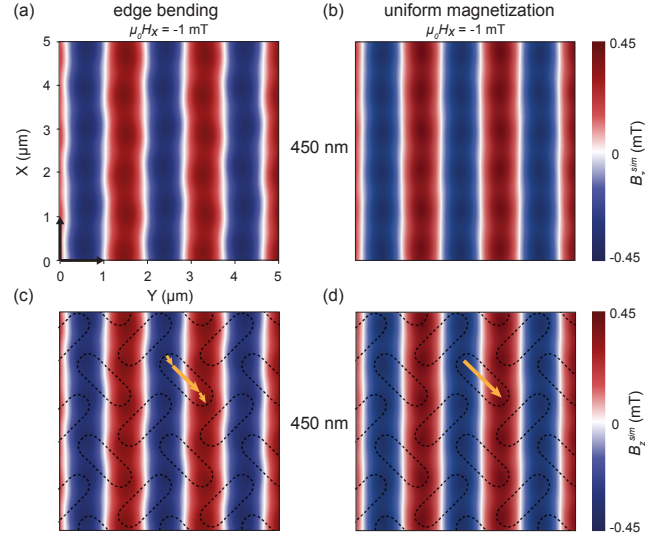


Figure 5.10. | (a) and (c) shows the same simulated magnetic stray field distribution $B_z^{sim}(x, y)$ close to zero field, which contains the bending of the magnetization at the edges. In (c) additional the positions of the nanomagnet are superimposed. (b) and (d) shows the same simulated magnetic stray field distribution $B_z^{sim}(x, y)$ close to zero field, but assuming a uniform magnetization of the nanomagnets. In (d) additional the positions of the nanomagnet are superimposed. In (c) a three-spin model (orange arrows) is used to describe more precisely the orientation of the magnetization. In the case of a uniform magnetization in (d), a single-spin is sufficient. The probe-to-sample distance is 450 nm and a tilt of 15° is considered.

To further investigate the effect of edge bending on the on the stray field pattern, micro-magnetic simulations were performed at various probe-to-sample distances. Figure 5.11 (a) and (b) shows the simulated magnetic stray field distribution, where (a) contains edge bending and (b) assume a uniform magnetization at a probe-to-sample distance of 500 nm. In (c) and (d) the probe-to-sample distance is 300 nm. Closer to the sample a small (periodic) departure from a straight line is visible, when a uniform magnetization of the nanomagnets is assumed. Most likely this is the influence of the periodicity of the chiral ice geometry on the stray field pattern. In the simulated magnetic stray field distribution $B_z^{sim}(x, y)$, which contains edge bending, the meander pattern is much more pronounced compared to the measured and simulated probe-to-sample distance of 450 nm, shown in figure 5.10.

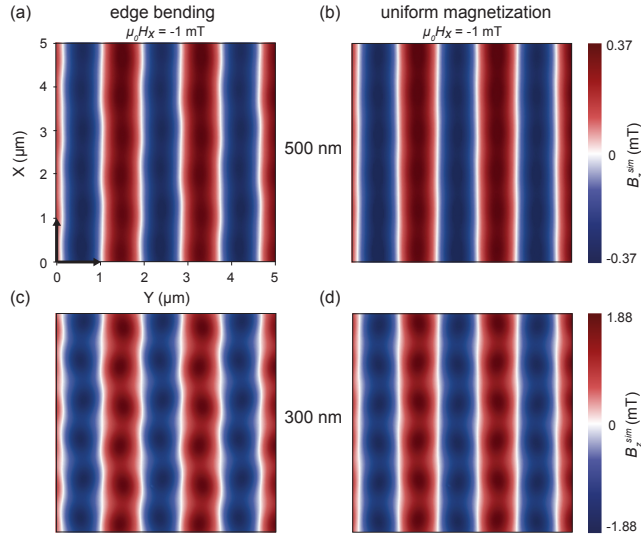


Figure 5.11. | Simulated magnetic stray field distributions $B_z^{sim}(x, y)$, which in (a) and (c) contain edge bending, while in (b) and (d) a uniform magnetization is assumed. In (a) and (b) the probe-to-sample separation is 500 nm, while in (c) and (d) it is 300 nm. A tilt of 15° is considered in (a,d).

In section 5.2, a magnetic field dependent ground state ordering in chiral ice was reported. Since the substrate has a tilt with respect to the plane, this ground state ordering can be understood qualitatively through a simple picture. Figure 5.12 (a) And (b) shows again the measured magnetic stray field distributions at $\mu_0 H_z = -6$ mT in each case. In (a) previously a magnetic field of $\mu_0 H_z = 708$ mT was applied to the chiral ice. In (b) the same field strength was applied, but in opposite direction. The high magnetic field strength causes almost all magnetic moments in the nanomagnets to point up or down, depending on the applied magnetic field direction. If we now consider a tilt with respect to the plane of 15° the magnetization has a preferred direction due to the tilt when the magnetic field strength is reduced. Figure 5.6 (c) shows a schematic drawing of a single nanomagnet, including a tilt of 15° , drawn in the case when previous a magnetic field of $\mu_0 H_z = 708$ mT was applied to the system. The local magnetization in each nanomagnet points up, as already shown previously in the measured magnetic stray field distribution in figure 5.5 (a). If the magnetic field is reduced to $\mu_0 H_z = -6$ mT the system falls into the ground state, obeying the ice rules. The net vertex magnetization points in the first case to the right, while in the second it points to the left due to the tilt.

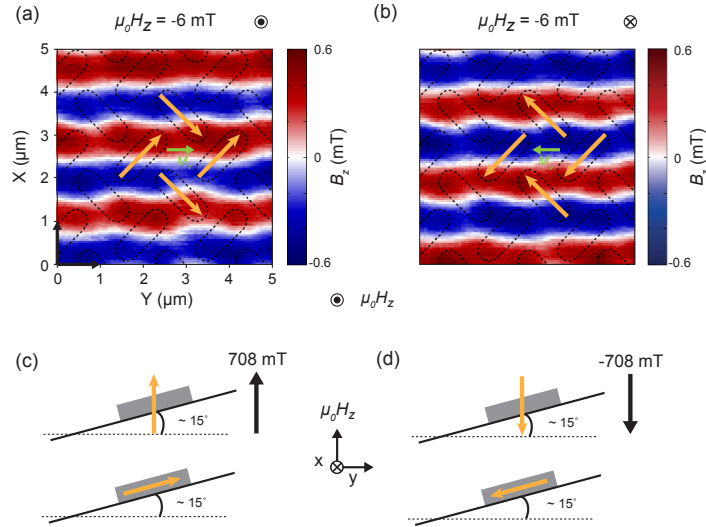


Figure 5.12. | (a) and (b) shows the measured magnetic stray field distribution $B_z(x, y)$ each at $\mu_0 H_z = -6$ mT. In (a) a magnetic field of $\mu_0 H_z = 708$ mT and in (b) of $\mu_0 H_z = -708$ mT was previous applied, to saturate the sample, before taking the images. The direction is thereby each depicted as black arrow, pointing out-of plane. Visible is that the “chiral ice” close to zero field ends up in a ground state, obeying the „ice rules“, but with a net vertex magnetization, which is pointing in opposite direction, depending on the previous applied magnetic field direction. (c) And (d) shows a schematic drawing of the substrate tilt in the microscope with respect to the plain. The black arrow shows the direction of the previous applied magnetic field and the corresponding magnetic configuration of the nanomagnet in the upper part and each at $\mu_0 H_z = -6$ mT in the lower part. A directed magnetic field dependent ground state ordering in chiral ice is observed, because of the preferred direction in rotation of the magnetization due to the tilt.

5.5. Conclusion and Outlook

For the first time scanning SQUID-on-tip was applied to a spin ice system and the evolution of the magnetization during a hysteresis loop was measured based on the stray field of the system, with the advantage of measuring the evolution of the magnetization as a function of an externally applied magnetic field. The micromagnetic simulations demonstrate that edge bending occurs in the studied spin ice system and contributes to the observed stray field patterns. The number of degrees of freedom in this system is thus much larger than can be described by dipolar models. A consequence of this fact is that novel dynamics, possibly even chaotic dynamics can arise, as well as new thermodynamic phases related to the edges in artificial spin ice and a rich mode spectra [125, 129]. One of the goals of investigating modes in artificial spin ice is to determine if it is possible to use them as reprogrammable and tunable magnonic crystals [126]. In this sense, the band structure can be modified by the edge bending to achieve a reprogrammable system [127]. An external magnetic field can also tune the band frequency by varying its magnitude $|H|$ and angle θ_H as already shown for the discussed “S”- and “C”-states previously [126].

The performed scanning SQUID-on-tip measurements represented a proof of principle. The next step would be to achieve higher spatial resolution, requiring a smaller effective SQUID-on-tip diameter and a shorter probe-to-sample distance. Similar magnetic stray field measurements can be performed with a different sample. Suitable would be the use of a square spin ice or a kagome spin ice. Both samples would give the opportunity to image for example the

magnetic stray field texture due to monopoles. Furthermore, in this kind of samples it would be interesting, to not only measure the stray field distribution, but also measure simultaneously the location of the nanomagnets. The next chapter 6 will describe a possible way to develop such a hybrid scanning probe as a new magnetic imaging tool.

6. A nanoSQUID on a Si-Cantilever: A hybrid system as a new magnetic imaging tool

In the previous chapters, the strengths of the SQUID-on-tip technology with the capability for quantitative nanoscale scanning magnetic microscopy with high magnetic field sensitivity and low spatial resolution has been demonstrated. In the last chapter, I would like to show how this magnetic imaging tool could be improved for future applications by extending its capability by one measurable size. The idea is to use instead of a hollow quartz tip a commercially available Si-cantilever, normally used for atomic force microscopy (AFM) imaging, as a support. To realize such a probe, a focused ion beam (FIB) is used to mill the apex of the Si-cantilever in a suitable shape, which later serves as a template for the nanoSQUID. The later Pb evaporation on the modified Si-cantilever is done in a similar fashion as for the SQUID-on-tip using the home-built thermal evaporation system. With this new technology we expect to retain the favorable properties of the SQUID-on-tip technique, while also adding sensitivity to tip-sample forces through standard non-contact AFM techniques. This hybrid system would allow to image the topography and the magnetic stray field of a magnetic nanostructure simultaneously. Thereby it would be possible to directly correlate changes in the stray magnetic field component with the surface topography of the sample.

6.1. Pb nanoSQUID on a Si-cantilever

To bring a SQUID in close proximity to a magnetic nanostructure and measure its magnetic stray field pattern, is a challenging task. This applies to conventional SQUIDs as well as for the in this theses described special SQUID-on-tip technique. To overcome this difficulty, it would be great to combine the property of a Si-cantilever with those of a SQUID. The idea is to realize a Pb nanoSQUID on the apex of a commercially available Si-cantilever, originally developed for atomic force microscopy (AFM). This combination first makes it much easier to bring the Pb nanoSQUID in close proximity to the sample, due to standard non-contact AFM techniques. Second once approached, one can additionally map the topography of the sample. This hybrid system allows to image simultaneously the magnetic stray field distribution $B_z(x, y)$, originating for instance from a current carrying wire (AC magnetic) or a magnetic nanostructure (DC magnetic), the associated local temperature distribution $\Delta T_{AC}(x, y)$ and the topography $\Delta z(x, y)$. This new magnetic imaging tool extends the capability of a scanning SQUID by a measurable size. The magnetization of a magnetic nanostructure and the resulting magnetic stray field may depend strongly on the shape. With this magnetic imaging tool it is possible to directly correlate changes in the stray magnetic field component with the surface topography of the sample.

6.2. Fabrication of a Pb nanoSQUID on a Si-cantilever

Conventional SQUIDS are usually obtained by e-beam lithography and chemical-mechanical polishing [130, 131]. To realize a SQUID at the apex of a Si-cantilever a completely different approach must be applied due to the shape. The shape of the Si-cantilever makes it impossible to use, for instance, e-beam lithography. This leaves the question arise what other possibilities exist for the fabrication of such a probe. One approach is, that one can use instead of lithographic techniques a focused ion beam (FIB) to mill the Si-cantilever shape at the apex in such a way that it later serves as a template for the nanoSQUID. Because this technology is a combination of a Si-cantilever with a SQUID, we will refer to it as SQUID-on-lever (SOL). Similar as for the SQUID-on-tip, the superconducting film can later be deposited on the modified Si-cantilever using the home-built thermal Pb evaporation system. The evaporation of Pb results in two superconducting leads running down to the apex of the Si-cantilever, where then the Pb nanoSQUID is located, consisting of a Pb loop intersected by two nanometric constrictions (Dayem bridges) in the region, where the two leads overlap each other.

The commercially available Si-cantilever consists of a carrier chip, from which a $500 \mu\text{m} \pm 5 \text{ nm}$ long and $100 \mu\text{m} \pm 5 \text{ nm}$ wide Si-cantilever protrudes on one side. Depending on the used type, the thickness is $1 \mu\text{m}$ or 500 nm . The Si-cantilevers consists of monolithic silicon, which is highly doped to dissipate static charge, further they are chemically inert. To hold the Si-cantilever in a fixed position during the evaporation process as well as in the microscope, a suitable holder had to be designed. The in-house-designed holder consists of Ti and was built that way, that a bias voltage can be applied to it, where the forward and return conductors are electrically isolated from each other. To be able to electrical connect the bias to the Si-cantilever, two Au pads were required on top of the carrier chip. In order to realize them, a suitable SOL Au-pad evaporation mask was designed. The evaporation mask allowed us to evaporate two 150 nm thick Au pads on top of the carrier chip, with an isolating gap between them (more details about the Au pads fabrication one can find in Appendix D.1). Figure 6.2 shows photographs of the in-house-designed holder in top view in (a), respectively in side view in (b). In front the affixed chip carrier is visible. For fixation a copper clamp was used, which makes further an electrical connection between the Ti-holder and the first Au-pad on top of the chip carrier, building the return conductor. For the forward conductor, a wire was used to make connection between Au-strips, permanently fixed on top of the Ti-holder and a copperplate screwed and therefore electrically connected to the top bias contact, mounted within an isolating bridge to the Ti-holder. Next to the bias contact the shorting screw is located. The shorting screw allows to make a short between forward and return conductors and prevents therefore the damage of the Pb nanoSQUID by electrical charge. To close the electrical circuit a wire bonder (Devoltec 5630) was used to make a connection with an Al-wire between an Au-strip and the second Au-pad on top of the chip carrier.

6.3. A single Dayem bridge at the apex of a Si-cantilever

In order to prove that, it is basically possible that the two Pb leads overlap each other in such a way at the apex of the Si-cantilever, that Dayem bridges are formed, first a single Dayem bridge is produced. To achieve that the Si-cantilever is milled in such a way, that a single weak-link is left at the apex, which serves later as a template for a single Dayem bridge. Figure 6.1 (a) shows a SEM image of the Si-cantilever after the FIB milling process, taken from the front.

The template for the single Dayem bridge after the FIB milling process has a length of $l_{sJJ} = 48 \text{ nm} \pm 5 \text{ nm}$ and is therefore lower than the coherence length (ξ) of Pb. A key factor for the functioning of a Dayem bridge. Later the home-built thermal evaporation system is used to evaporate two Pb leads running down to the apex from both sides. The Pb leads overlap each other just in the region where the single weak-link is located. Figure 6.1 (b) shows a SEM image taken after the evaporation of a 150 \AA thick Pb film from two sides at an angle of $\pm 75^\circ$. For clarity the superconducting film is colored in a light blue in the SEM image. It is visible that the two Pb leads just overlap each other solely where the previous manufactured weak-link is located, forming a single Dayem bridge (sJJ). To check if the device is working the current-to-voltage-characteristic (IVC) has to be measured. From the measured IVC at cryogenic temperature (4.2 K) a transition between the superconducting and resistive state is observed. From the IVC a critical current of $I_c = 100 \text{ \mu A}$ is determined. This represents a promising result for the development of a nanoSQUID, which should consist of two such Dayem bridges. To obtain the thermal sensitivity of the device the IVC measurement is repeated while increasing the temperature locally around the device in 0.175 K steps by using a heater, giving us the temperature dependence as shown in figure 6.1 (c). A higher ambient temperature leads to a low I_c until above the critical temperature (T_c) the whole device is resistive and shows a linear response. From the temperature dependence we find a thermal sensitivity of 34 \mu A/K .

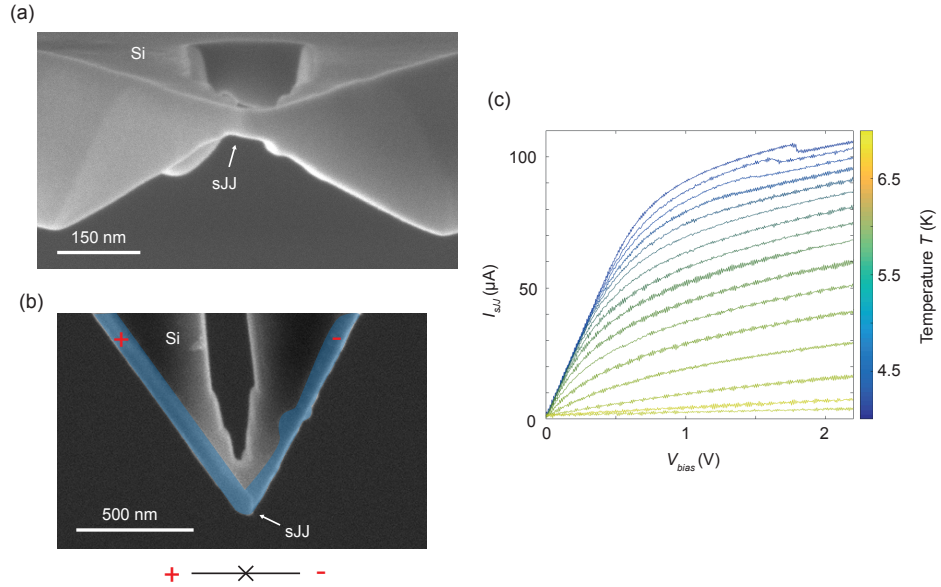


Figure 6.1. | (a) shows a SEM image of the Si-cantilever from the front after the FIB milling process with a geometry serving as a template for a single Dayem bridge at the apex. The position of the Dayem bridge at the apex of the Si-cantilever is shown with white arrows in (a) and (b). The weak-link after the FIB milling process has a length of $l_{sJJ} = 48 \text{ nm} \pm 5 \text{ nm}$. The SEM image taken from the top in (b) shows the Si-cantilever after the evaporation of a 150 \AA thick Pb film from the left and right (More details one can find in table D.3). For clarity the superconducting film is colored in a light blue in the SEM image. (c) shows the current-to-voltage-characteristics (IVC), which is measured at different temperatures ranging from 4.2K to 7.0 K in 0.175 K steps. We find at 4.2 K a critical current of 100 \mu A and from temperature dependency a thermal sensitivity of 34 \mu A/K .

The plan was to mount this working single Dayem bridge on a Si-cantilever in the microscope and approach with in in close proximity to a current carrying wire to image simultaneously

the magnetic stray field distribution $B_z(x, y)$, the associated local temperature distribution $\Delta T_{AC}(x, y)$ and the topography $\Delta z(x, y)$. We tried to mount the device in the microscope, but unfortunately the SSAA was not working properly after the cooldown, so we were not able to test the single Josephson junction on a Si-cantilever (sJJOL) as a scanning probe. The sJJOL fabrication history one can find in detail in Appendix D.3.

6.4. Two Dayem bridges at the apex of a Si-cantilever

After the successful production of a single Dayem bridge at the apex of a Si-cantilever, which showed the desired characteristics, the idea was to go a step further and produce two working Dayem bridges, which forms a Pb nanoSQUID. In the following I would like to show more in detail how the fabrication of a SQUID-on-lever (SOL), consisting of two Dayem bridges at the apex of a Si-cantilever proceeds. First the chip carrier, where previous two Au-pads are evaporated on top, is mounted on a special FIB holder. The FIB holder allows to place the protruding Si-cantilever on top of a razor blade under an optical microscope. It is important to place the Si-cantilever on a razor blade, since the interaction with the Ga-ions leads to a strong movement, which makes it impossible to fabricate nanoscale structures at the apex. To fabricate the template, for the later Pb nanoSQUID on a Si-cantilever, a FEI Helios NanoLab 650 SEM in combination with a focused Ga-ion beam (FIB) is used. The Ga-ion source was operated at 30 kV and with a low current of 7.7 pA to prevent the Si-cantilever from being damaged by the fabrication. With the FIB it is possible to mill a hole at the apex in the range of 66 - 350 nm. The resulting ring then serves as a template for the superconducting loop. In addition, it is possible to determine the positions and dimension of the constrictions. The constrictions serving as a template for the later Dayem bridges have a width in the range of 26 - 99 nm. After the FIB nanopatterning the carrier chip has to be mounted carefully on the Ti-holder for the microscope. The Ti-holder possesses a small slot including notches to have space with the tweezers during the alignment of the carrier chip. After alignment the carrier chip is fixed to the Ti-holder by a copper clamp. The copper clamp has two tasks, first to fix the chip carrier and secondly to provide an electrical connection between the Ti-holder and one Au-pad. The Ti-holder is then mounted at the end of the cold finger, which is rotatable 360° around its axis, while the Pb source is at a fixed position, in the home-built thermal Pb evaporation system. Figure 6.2 (c) shows a schematic diagram of the used “tipless” Si-cantilever, protruding in the middle of the carrier chip on the right side. The Si-cantilever is elevated a few micrometers. This geometry is important to ensure that the evaporated superconducting leads make an electrical connection to both Au-pads on top. The angle between the Pb source and the Ti-holder with respect to the normal of the protruding Si-cantilever, was set to $\pm 75^\circ$ and a Pb film (light blue) of about 180 Å was evaporated on both sides of the Si-cantilever. The two Pb leads make an electrical connection to the Au-pads on the carrier chip. The leads running down on the sides of the Si-cantilever and overlap each other at the apex, building there the two Dayem bridges. This SOL fabrication type refers to configuration ①, where the position of the Dayem bridges, building the Josephson Junctions (JJ), is at the top and bottom as shown in the electrical scheme in (d). Figure 6.2 (d) shows further a SEM image taken after the Pb evaporation. Visible are the two Au-pads in the upper left part as well as a 300 μm long Au-strip, which shorts the two Pb leads. The short leads to a non-hysteretic characteristic of the Pb nanoSQUID. After the Pb evaporation process the obtained SOL is ready to be characterized by applying a bias voltage to the device, while

measuring the current flowing through the Pb nanoSQUID. The characterization of the SOL is performed in the same way as for SQUID-on-tip, which was previously discussed in chapter 1.3.3.

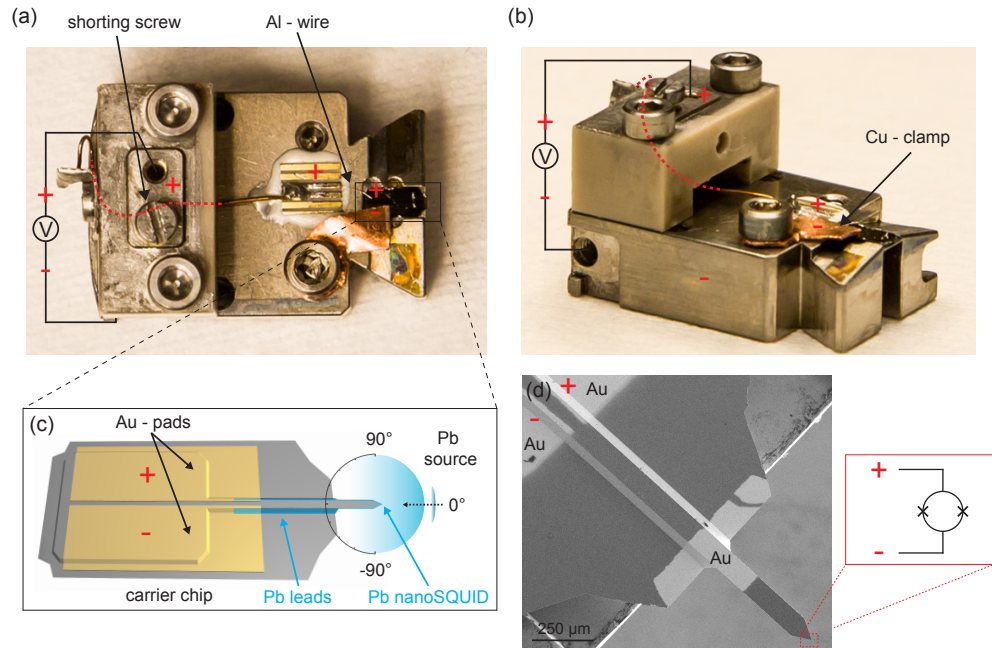


Figure 6.2. | Photographs of the in-house designed holder for the microscope: (a) shows the top view and (b) side view. The carrier chip of the Si-cantilever is clamped to the holder using a copper clamp, its function is further to close the electrical circuit of the applied bias voltage. Electrical connections, which are not completely visible are shown with red dashed lines. (c) A schematic diagram of a “tipless” ArrowTM TL1 cantilever in the pendulum geometry with Au contacts (yellow) and evaporated superconducting leads (light blue) running down to the apex on both sides is shown. The inset of the apex shows the electrical scheme of the positions of the JJs and the leads at the end of the Si-cantilever. This type of SOL fabrication shows the design of the configuration ①. The Pb source is at fixed position, while the Si-cantilever mounted on the cold finger is rotatable by 360° around its axis. To ensure that the evaporated Pb connects to the Au contacts as well as overlap in a small area at the apex, the usually set angle between the Si-cantilever and the Pb source is $\pm 75^\circ$. (d) SEM image taken after Pb evaporation on the ArrowTM TL1 Si-cantilever fixed on the Ti-holder. Clearly visible is that the protruding Si-cantilever is elevated. Further the two Au-pads are visible in the upper left part of the SEM image as well as a 300 μm long Au-strip, shorting the two Pb leads. The short leads to a non-hysteretic characteristic of the Pb nanoSQUID.

It turned out that the contact resistance can be reduced, when the position of one Au-pad is changed from the top to the bottom of the carrier chip, increasing therefore the contact area. This type of SOL fabrication refers to configuration ②. In this configuration, the Pb leads run down to apex on top and on bottom of the Si-cantilever. Therefore the previous milled nanometric constrictions had to be tilted by 90° . In this configuration one has to ensure that the Pb leads just overlap at the apex. To achieve this one has to mill a 100-nm-wide and at least 100-nm-deep trench along the edge of the triangle shaped Si-cantilever. This trench ends close to the nanometric constrictions on one side and on the other where the Si-cantilever straightens. In this configuration, the dimension of the trench and the hole in the center of the apex defines the size of the nanometric constrictions. Figure 6.3 shows SEM images of Si-cantilevers after the FIB nanopatterning of the aforementioned configuration ①

in (b) and of configuration ② in (d). (c) And (e) shows the corresponding Si-cantilever after the Pb evaporation, forming in a working case a Pb nanoSQUID at the apex. For clarity the superconducting film is colored in light blue in the SEM images. In (d) the milled trench is visible on the left and right side of the centered hole. For both configurations the electrical scheme is depicted, which shows the positions of the Dayem bridges and from which side the bias is applied to the superconducting loop.

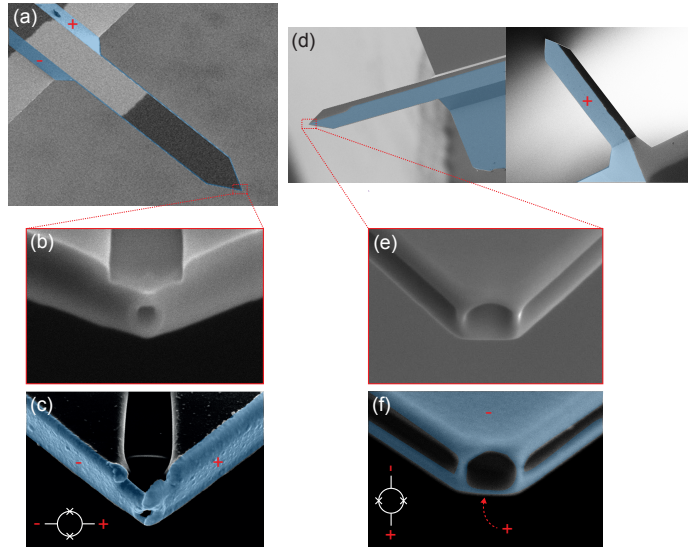


Figure 6.3. | (a) Overview SEM image of configuration ①. (d) Overview SEM image of configuration ②. In both cases the Si-cantilever is protruding from the carrier chip. After the Pb evaporation the Pb nanoSQUID is located at the apex in both cases. (b) and (e) shows SEM images of configuration ①, respectively configuration ②, taken after the FIB nanopatterning. (c) And (f) shows SEM images of the same Si-cantilevers, but taken after the Pb evaporation and showing therefore the resulting Pb nanoSQUIDs at the apex. For clarity the area, where the superconducting film is located, is colored in a light blue in the SEM images. The electrical scheme depicts the positions of the Dayem bridges, with respect to the corresponding SEM image.

The main difference between these two configurations lies in the different running of the leads. Configuration ① has the two leads running down on the sides to the apex of the Si-cantilever, while in configuration ② the two leads are running down at the top and bottom to the apex of the Si-cantilever. The main advantage of configuration ② compared to configuration ① is that, due to the bigger connection area between the bottom Au-contact and the Ti-holder, the contact resistance is less. The fabrication history of configuration ① and ②, including all important parameters, one can find in Appendix D.4, respectively in D.5. If the Pb nanoSQUIDs on Si-cantilever were not working at all, because no current was flowing or it showed a resistive behavior, most of the time just a single Dayem bridge worked, which results in single Josephson Junction (sJJ) behavior in the IVC. To solve this problem, the idea was to make the area at the apex, where the Pb nanoSQUID is located, smaller. Figure 6.4 (a) shows a SEM image taken after the FIB milling process. Visible is that the apex is milled in a way that the area where the hole and the constrictions are located are smaller. That was achieved by milling at the top and the bottom additionally trapezoid features at the apex, which leads to a pyramid-like shape. The pyramid-like geometry of the apex should help that the two lead leads overlap each other in a suitable fashion. This slightly modification of configuration ② is therefore called a Si-cantilever having a pyramid-like geometry.

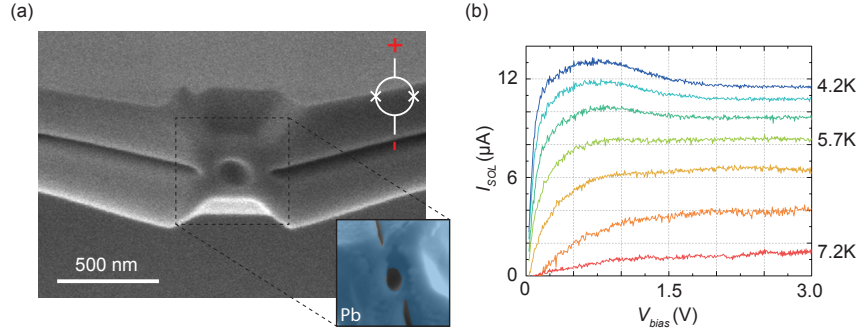


Figure 6.4. | (a) shows a SEM image of the Si-cantilever taken after the FIB milling process into a pyramid-like geometry at the apex. The dashed rectangle shows the section of the corresponding SEM image after the Pb evaporation of a 300 Å thick film, resulting in two connected weak-links (Dayem bridges) intersected by a hole with a diameter of $d_0 = 147 \text{ nm} \pm 5 \text{ nm}$, creating the Pb nanoSQUID. (b), Shows the current-to-voltage-characteristics (IVC) at 4.2 K, showing a nice transition between the superconducting and resistive part at a critical current of $I_c = 12.7 \text{ } \mu\text{A}$. From the temperature dependence measurement a thermal sensitivity of $12.9 \text{ } \mu\text{A/K}$ was found.

The hole in the center had a diameter of $d_0 = 147 \text{ nm} \pm 5 \text{ nm}$ and the template for the Dayem bridges had a size of $60 \text{ nm} \pm 5 \text{ nm}$. The dashed rectangle in (a) shows the section of the corresponding SEM image after the Pb evaporation of a 300 Å thick Pb film from the top and bottom. The angle between the Si-cantilever with respect to the fixed Pb source has been set to $\pm 80^\circ$. The chosen angle allows that the both leads become sufficiently thick and also that the amount of Pb overlapping at the apex is enough to create two Dayem bridges. Figure 6.4 (b) shows the IVC from which a critical current of $I_c = 12.7 \text{ } \mu\text{A}$ at 4.2 K is determined. This obtained critical current I_c is in an order of magnitude too small compared to the ideal value of $120 \text{ } \mu\text{A}$. A possible explanation could be that the thickness of the evaporated lead, overlapping at both bridges as well as the created superconducting ring at the apex is too thin. One possible way to increase the amount of Pb locally at the apex would be to perform a third evaporation step similar to the SQUID-on-tip fabrication, or just simply increase the amount of Pb during the evaporation of the two leads. The third Pb evaporation step is performed at an angle of 0° between the Si-cantilever with respect to Pb source. Compared to the SQUID-on-tip fabrication one has to be careful with the thickness of this Pb film, because it can short the top and bottom lead at the carrier chip. It turned out that a Pb film thickness of $120 \text{ } \text{Å}$, which is usually used for the SQUID-on-tip fabrication and was previously described in chapter 1.3.2, is enough to make a short between the locally covered top and bottom lead. Measurements showed that the limitation for the Pb film thickness, which makes no short, is around $80 \text{ } \text{Å}$. The reason is the following that a thin Pb film completely oxidizes and therefore has a high enough resistance that no current can flow between the two covered leads. The IVC measurement is repeated while increasing the temperature locally around the device using a heater until the critical temperature, giving us the temperature dependence. From the temperature dependence we find a thermal sensitivity of $12.9 \text{ } \mu\text{A/K}$.

We also mounted this SOL in the microscope and the idea was to do the same experiment, which was planned for the single Dayem bridge on Si-cantilever, namely the imaging of a current carrying wire, but unfortunately the Si-cantilever broke during the mounting in the microscope that's the reason why no measurements are shown at this point. Nevertheless, the

IVC measurements showed that it is basically possible to get two working Dayem bridges at the apex of a Si-cantilever.

6.5. Further development of the technology

As shown in the previous mentioned fabrication of configuration ① and ② many steps are involved to get a working Pb nanoSQUID at the apex of a Si-cantilever, which makes the production of those difficult. The success of fabrication depends on many parameters. An important parameter for instance is the obtained apex geometry through the FIB nanopatterning. The template geometry always differs slightly for each Si-cantilever. Another important factor is the used Pb evaporation angle including also the evaporated thickness of the Pb film. All of these parameters define in the end the size of the Dayem bridges and have therefore a direct influence on the IVC. Furthermore the used “tipless” Si-cantilever can only be operated in the pendulum geometry, which does not correspond to a standard AFM setup. For that reason it would be nice to have the opportunity to operate the Si-cantilever in a usual geometry, as for contact mode AFM imaging, which is a further development of the technology. In the usual geometry the Si-cantilever is located parallel to the sample surface. To achieve both less parameters and a standard operation, a suitable Si-cantilever was found in the form of a commercially available AFM probe (more details in Appendix D.2). This type of AFM probe is designed for contact mode AFM imaging. From the top of the Si-cantilever a tetrahedral tip protrudes perpendicular to the Si-cantilever. The height of the protruding tetrahedral tip at the apex is given to be 15 - 20 μm . Figure 6.5 (a) shows a SEM image of the AFM probe type used for configuration ③, placed on a razor blade, which allows to mill nanostructures using the FIB, due to the damped movement of the Si-cantilever. In (b) a higher magnified SEM image is shown, taken from the area where the tetrahedral tip protrudes of the Si-cantilever. At the end of the protruding tip the Pb nanoSQUID is located. (c), Shows a SEM image of the Si-cantilever corresponding to (b) but imaged from the side. Visible is at the end of the protruding tip the FIB milled plateau, which forms later the region for the template for the Pb nanoSQUID. Furthermore it can be seen that one edge of the tetrahedron has a rounded shape. This geometry helps to prevent that the Pb leads can make an electrical connection in this section, due to the shape, which acts like a shading mask. Another big advantage of this configuration ③ compared to configuration ① and ② is the following, that a nano-scaled tip can be machined at the end. The distance between the tip end and the Pb nanoSQUID is 270 nm in the shown case. The nano-scaled tip, having a tip size at the end of around 13 nm, has the function to protect the Pb nanoSQUID upon contact with the sample and is shown in (d) in more detail from the front. Behind this protection tip the edges of the machined plateau is visible, whereupon the nanoSQUID is placed. The topview in (e) shows a SEM image from the same region compared to (d) but taken after the evaporation of a 180Å thick Pb film at an angle of 90° with respect to Pb source. For clarity the superconducting film is colored in a light blue in the SEM image. The hole has a diameter of $l_0 = 170 \text{ nm} \pm 5 \text{ nm}$ and the Dayem bridges have a length of $l_{JJ} = 33 \text{ nm} \pm 5 \text{ nm}$. The IVC of this specific Pb nanoSQUID showed a resistive behavior and was therefore not suitable for further use. The whole production history of configuration ③ is shown in Appendix D.6. We had from the first fabricated sensor the indication that also this configuration might work at some point. There the IVC showed a critical current of 216 μm and a small thermal response. The diameter of the hole in center

was $l_0 = 190 \text{ nm} \pm 5 \text{ nm}$ and the width of the template for the Dayem bridges was with $l_{JJ} = 45 \text{ nm} \pm 5 \text{ nm}$ slightly bigger compared to the previous described.

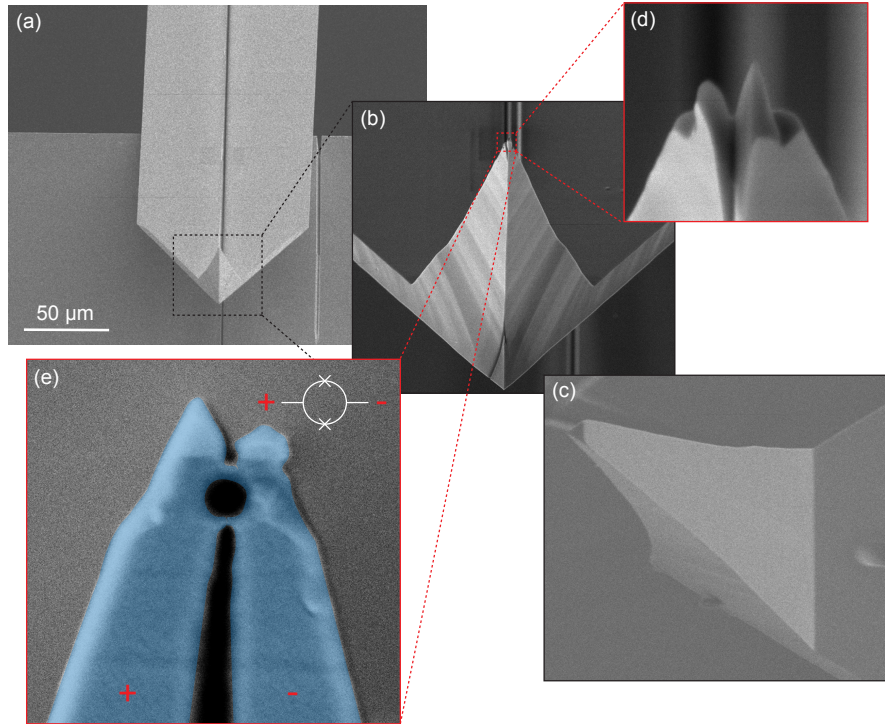


Figure 6.5. | (a) shows the SEM image of the used AFM probe type for configuration ③. The Si-cantilever is placed on a razor blade, which allows to mill nanostructures using the FIB, due to the damped movement. Visible is the cut through in the middle using the FIB. As a result, the Si-cantilever is divided into two arms, which then forms the template for the Pb leads. (b), Shows the same Si-cantilever but with higher magnification in the area where the tetrahedral tip protrudes at the end. (c), Shows a SEM image of the Si-cantilever corresponding to (b) but imaged from the side. Visible is at the end of the protruding tip the FIB milled plateau, which forms later the region for the template for the Pb nanoSQUID. Furthermore it can be seen that one edge of the tetrahedron has a rounded shape. This geometry helps to prevent the Pb leads from making an electrical connection in this section, due to the shape, which acts like a shadow mask. (d), Shows a front view of the shaped protection tip, which ends 270 nm above the plateau level. (e), Shows the corresponding top view of (d) but taken after the evaporation of a 180Å thick Pb film at an angle of 90° with respect to Pb source. Visible is the milled hole located at the center, having a diameter of $l_0 = 170 \text{ nm} \pm 5 \text{ nm}$. The milling of two trenches as close as possible to the hole leads to the creation of two bridges having a length of $l_{JJ} = 33 \text{ nm} \pm 5 \text{ nm}$. The milled hole as well as the milled trenches is visible. For clarity the superconducting film is colored in a light blue in the SEM image.

6.6. Next steps in the development of this promising scanning probe technology

The most promising result of a working SOL so far was achieved with the combination of configuration ① and ②, as described in subchapter 6.3. The main reason for the success was the special fabrication, which included a further milling step and leads to a pyramid-like geometry at the apex, where the Pb nanoSQUID is located. The smaller area increased the probability that the evaporated lead overlap in the right way and form two Dayem bridges, with the right dimensions. But this type of production is not reducing the amount of parameters and is therefore not the best option to follow in future due to the low reproducibility. Another promising result was obtained with configuration ③, where a tip protrudes at the apex, as described in subchapter 6.4. There the FIB nanopatterning is much more complicated compared to configuration ① and ②, but with a big advantage that just one evaporation step is needed to get the Pb leads running down to the apex on two thighs, where the Pb nanoSQUID is located. A further advantage of this configuration is that the Pb doesn't have to overlap to build the Josephson Junctions at the weak-links, which makes the connection in general more homogenous at the transition to the superconducting ring and the leads. The thickness of the Pb is depending on the amount evaporated and is for the leads, the superconducting ring as well as the formed Dayem bridges the same. In general the fabrication of the bridges needs high machining fidelity. Until now a Ga-ion beam was used for the fabrication. Instead of Ga-ion beam a He-ion beam can be used for the FIB nanopatterning. With such a helium beam one could create delicate sub-10 nm structures with an extremely high machining fidelity. This would improve the creation of the nanoSQUID's template and could increase the success rate due to the higher precision, especially in the case of configuration ③.

From an experimental point of view a suitable sample to be measured using the SOL as a new magnetic imaging tool could be for instance the artificial spin ice system, which was mentioned in chapter 5. In an artificial spin ice system, the information of the exact positions of the nanomagnets would have been really helpful to understand the imaged stray field distributions $B_z(x, y)$. In this thesis micromagnetic simulations were needed to extract the exact positions of the nanomagnets, the SOL would have made our live easier, because both information about position and the originating magnetic stray field would have been obtained simultaneously with this magnetic imaging tool. The successful production of such a device and the subsequent measurement would be a breakthrough in the research area of scanning probe microscopy and could find many applications in the basic research.

6.7. A tungsten carboxyl nanoSQUID on a Si-cantilever

Apart from the presented different production types to get a Pb nanoSQUID on Si-cantilever, a fourth completely different fabrication type was being considered. In this type of fabrication, the leads consist of each 250 Å thick gold, which run down on the top and the bottom of the Si-cantilever till the apex, in an offset fashion, as shown in a SEM image taken after the Au evaporation in figure 6.6 (a). The geometry of the Si-cantilever and the carrier chip helps, that the two Au leads are all over isolated from each other. Using a focused ion beam (FIB) the apex is first cut orthogonal to the longitudinal axis of the Si-cantilever in such a way that a plateau of the size 500 x 500 nm originates, as shown in (b). The cut plateau forms a flat surface for the later deposition of tungsten carboxyl $W(CO)_6$ (W-C), as superconducting

material, using focused ion beam induced deposition (FIBID) with a gallium ion beam. W-C nanowires were reported to exhibit superconductivity at a critical temperature T_c of 5.2 K [134], this value is much higher than for bulk crystalline tungsten of 0.01K [133]. The plan is that W-C is deposited in the such a way, that it forms a superconducting loop intersected by two constrictions and connects to the top and bottom Au leads, that a bias current (I_b) can flow through the structure forming a W-C nanoSQUID on a Si-cantilever. The proposed W-C structure is shown in figure 6.6 (c) as a schematic drawing (cyan) and on the right side the drawing of the corresponding electrical circuit is shown.

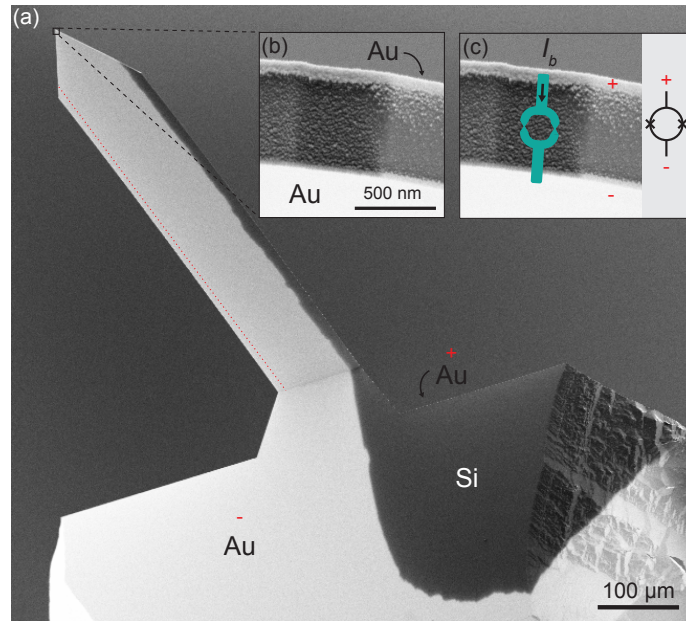


Figure 6.6. | (a) shows a bottom view SEM image of a Si-cantilever protruding from the carrier chip taken after the evaporation of 250 Å thick Au on both sides. The dashed red line shows approximately the position of the end of the upper lead similar to the visible end on the bottom side on the right (the two leads proceed offset from one another). The geometry of the Si-cantilever and the carrier chip helps, that the two Au leads are isolated from each other. (b), Shows a SEM image with a higher magnification from the apex in top view. Visible are the Au-leads on top and the bottom (bright contrast) of the Si-cantilever (gray contrast). Under the use of FIB, previous the apex was cut orthogonal to the longitudinal axis of the Si-cantilever, that a plateau of the size 500 x 500 nm originates. (c), Shows the same SEM image as in (b) but including a schematic drawing of the proposed tungsten-carboxyl $W(CO)_6$ (W-C) structure (cyan) on it. It is planned to deposit the W-C structure onto the Si cantilever using focused ion beam induced deposition (FIBID). The W-C is deposited in such a way, that it forms the superconducting loop intersected by two constrictions and connects to the top and bottom Au-leads, that a bias current (I_b) can flow through the structure. On the right side the corresponding electrical circuit is shown.

First tests have been carried out on single FIBID deposited W-C wires on a Si-substrate, intersected by a constrictions with a diameter of $d_c = \sim 15$ nm, which should have the function of a Josephson junction. It turned out that at a temperature of $T = 2$ K no Fraunhofer-like oscillation of the critical current as a function of an out-of-plane applied magnetic field up to $\mu_0 H_z = 2$ T of the W-C structure is observed. The main reason might be that the coherence length of the material is close to the measured coherence length of $\xi_0 = 5.9$ nm of a W-C wire [134]. One option might be to use instead of a Ga-ion beam a He-ion beam. Two advantages arises, first, structures can be fabricated smaller in the range of 5 nm and second, the W-C

wire and the constriction are done in a single step, which helps to have less damaging effects due to the Ga-ions. Another option would be to fabricate a W-C superconductor/normal metal/superconductor (SNS) Josephson junction [132]. As a normal metal junction one can deposit a W-C bridge by tuning the component ratio of tungsten and carboxyl that the material does not undergo a superconducting transition and stays metallic [135] or one can deposit just a carboxyl bridge. Figure 6.7 (a) shows SEM image of a 46 nm thick W-C single wire with a gap of 185 nm. (b), Shows a SEM image of a W-C single wire, where the gap is filled with carboxyl using the precursor $C_{10}H_8$. (c), Shows the same bridge as shown in (b) but with a tilt of 52° , where the connection on both sides to the superconducting W-C wires are visible.

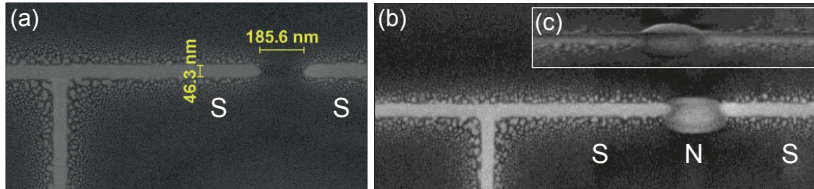


Figure 6.7. | (a) SEM image of a ~ 46 nm thick single W-C wire deposited on a Si-substrate using focused ion beam induced deposition (FIBID) with a gap left of ~ 185 nm in between, which can later be closed with a metallic material. (b) SEM image of a W-C single wire, where the gap is filled with carboxyl using the precursor $C_{10}H_8$ as metallic material, which should form a superconductor/normal metal/superconductor (SNS) Josephson junction. (c), Shows the same bridge as shown in (b) but with a tilt of 52° .

The current-to-voltage characteristics (IVC) of the shown W-C SNS Josephson junction has not been measured yet. But this type is the most promising one, because Dai et al. recently showed that such W-C SNS Josephson junction show a symmetric Fraunhofer-like oscillation of the critical current [132]. The next step in this project, to produce a W-C nanoSQUID on a Si-cantilever, is that the IVC should be measured soon by our collaborators from the Group of José María de Teresa Nogueras at the University of Zaragoza.

7. Conclusion, Discussion and Outlook

The aim of this thesis was initially a detailed analysis of the static magnetic properties of ferromagnetic nanostructures. The focus lied first on the investigation of ferromagnetic nanotubes (FNTs) having various ratios between diameter and length. The ferromagnetic nanotubes are made by depositing a thin CoFeB or Py film on non-magnetic GaAs nanowires having hexagonal cross-sections and acting as templates. They were investigated using two different magnetic imaging techniques. The first used magnetic imaging technique is sensitive to the direction of local magnetization, while the second is sensitive to the stray magnetic field, which is influenced by the prevailing local magnetization. It is in the first case x-ray magnetic circular dichroism photoemission electron microscopy (XMCD-PEEM) and in the second case a scanning SQUID-on-tip. The XMCD-PEEM measurements were performed at room-temperature, while the scanning SQUID-on-tip measurements were performed at cryogenic temperatures due to the critical temperature of the used superconducting material. Performed micromagnetic simulations predict and the obtained images of both measurement types confirm that equilibrium remnant magnetization configurations can be programmed by the ratio between diameter and length. The XMCD-PEEM measurements revealed that FNTs with a length longer than $2 \mu\text{m}$, have as a remnant state a mixed state, in which the magnetization in the middle is pointing uniformly towards the long axes of the FNTs, whereas near the tube ends curling states of various circular polarities occur. Whereas shorter FNTs favor global vortex state, where the magnetization points along the FNT circumference, or an opposing vortex state, which includes a Néel wall between two opposing vortices. A global vortex state, which is a flux-closure configuration might be interesting, because they produce minimal stray fields and can thereby find applications in densely packed storage devices. From additional simulations, it was suggested, that sample imperfections including variations in thickness and deviations from a perfect geometry are responsible for the discrepancy. In addition it was found under the use of the scanning SQUID-on-tip technique, that even a slight distortion due to the imperfections of real samples, the global vortex state is dominant and therefore robust. The imperfect geometry causes even the global vortex state to produce magnetic stray fields in the order of $100 \mu\text{T}$ at a probe to sample-distance of 300 nm . For future applications it would be great to have a finer control of the sample geometry in order to reduce the magnetic stray field originating from the FNTs, which would further minimizes the interactions of neighboring elements in such storage devices. Both used measurement types show the promise of using geometry to program both the overall equilibrium magnetization configurations and the reversal process in nanoscale magnet.

Recently other experiments on FNTs evidenced multiple magnetic domains and domain walls in electroless-deposited CoNiB nanotubes [136]. In their case, they claim that the orthoradial anisotropy may originate from the growth-induced strain and/or grain shape. Zimmermann et. al. reported a stable vortex ground state for long nanotubes consisting of Py, which was grown directly on the GaAs core. Also they report that a large growth-induced anisotropy is responsible for their finding, with an Al_2O_3 buffer layer, they were able to reduce the anisotropy by a factor of 1.5 [137]. In both cases, there is a big difference in the production

of FNT compared to us. Both growing steps are done in-situ in their case, while in our case the GaAs core and the CoFeB or Py deposition were grown at two distinct places. This might explain why we were able to image mixed states in long FNTs instead of multiple magnetic domains, because in our case the contact with air causes oxidation of the GaAs surface, which significantly reduces the growth induced anisotropy [139].

A further interesting experiment on FNTs might be to use for magnetic imaging a scanning transmission x-ray microscopy (STXM) [138]. This technique has the tremendous advantages that during imaging a magnetic field can be applied in-situ. This would allow to image the local magnetization of FNTs of the reversal process with a high spatial resolution down to 7 nm [140]. This would furthermore allow to determine the length of the vortices more accurately.

After the execution and detailed analysis of the FNTs experiments the focus shifted to investigate another ferromagnetic nanoscale system, which consists of periodically arranged Py nanomagnets. The nanomagnets are arranged in the geometry of a chiral ice system, which is strongly magnetostatically coupled. The aim was to image the static magnetic configurations of the spin ice system as a function of externally applied magnetic fields under the use of the for such purposes suitable SQUID-on-tip technique. In most of the studies such nanomagnets are approximated as Ising-spins and therefore described with dipolar models. But in fact our measurements reveal and micromagnetic simulations confirm that edge bending is present in such spin ice systems. This shows that in fact the number of the degrees of freedom is larger than captured with dipolar models. A consequence of this fact is that there is novel dynamics, possibly even chaotic dynamics and there are new thermodynamics phases related to the edges in artificial spin ice as well as a rich mode spectra [125, 129]. An application of such edge bending might be reprogrammable systems, where an externally magnetic field can tune the band frequency by varying its magnitude $|H|$ and angle θ_H [126].

The last part of this work was focused on developing a hybrid scanning probe as a new magnetic imaging tool, with which it will be possible to image the topography and the magnetic stray field of a magnetic nanostructure simultaneously. The basic idea was to combine the tremendous advantages of a SQUID with those of a mechanical resonator. To realize such a hybrid scanning probe, the apex of a Si-cantilever is milled in a suitable shape using a focused ion beam (FIB), which serves later as a template for the nanoSQUID. The later deposition of a thin Pb film on top of the modified Si-cantilever leads to a Pb nanoSQUID on top of a mechanical resonator.

The work shows different ways of production, which should pave the way to fabricate in future a working SQUID at the apex of a mechanical resonator. Already promising results in this direction have been achieved. So far, we were able to fabricate a single Dayem bridge (single Josephson junction) at the apex of a Si-cantilever (sJJOL). Furthermore, we have an indication that also two Dayem bridges forming a Pb SQUID at the apex of a Si-cantilever (SOL) might work, if all parameters have the suitable dimension. What is missing so far are measurements, where we use such a sJJOL or a SOL, as a hybrid scanning probe. The successful production of such a SOL and the subsequent measurement on a suitable sample would be a breakthrough in the research area of scanning probe microscopy and could find many applications in the basic research. This mainly because the hybrid technique allow to correlate directly the stray field with the topography of a suitable sample.

Acknowledgements

All periods in life will once come to an end – this might be the lyrics of a new song from n.eo – but it isn't. I started my PhD work in the Poggio Group in 2014, more than four years ago. In this period of time I learned a lot of new things, but now it's time to tell you the truth, the whole work would have been impossible without the help of a large number of persons. Now that the degree is approaching, it's time to thank all who have accompanied me the last exciting years. First of all I want to thank Martino Poggio. I highly appreciated to work with you and to be a part of your fantastic group. Furthermore I would like to thank Denis Vasjukov, which introduced me in the fantastic world of the SQUID-on-tip technology. It was an honor for me to work with you. Your big knowledge about SQUIDS in general as well as your outstanding engineering skills, were very important. Armin Kleibert for first giving me the opportunity to perform measurements at the Surface/Interface: Microscopy (SIM) beamline even after my master thesis at PSI and second, for all the discussion about the XMCD-PEEM experiment and the phone calls at two o'clock in the night, when for some reason the PEEM stopped working. Alan Farhan, Michelle Buzzi, Jaianth Vijayakumar, David Bracher which all have made a bigger or smaller contribution that the XMCD-PEEM experiment succeeds. Boris Gross, Andrea Mehlin and Patrick Appel, the beamtime squad, which made the night and the day more bearable in the middle of nowhere. Boris Gross also for the numerical simulations, which corroborate the XMCD-PEEM measurements and as my valued lunch partner, at almost every lunchtime. Arne Buchter, which introduced me in the first year into the laboratory environment and showed me all the little tricks to survive. After his graduation as a serious squash partner. Sebastian Gliga for the fabrication of the chiral ice sample and for all the performed micromagnetic simulations of this system, even in the last second before submitting this work. I highly appreciated to work with you. Lorenzo Ceccarelli and later also Giulio Romagnoli, members of the SQUID squad. We fought against all odds and got the various SQUID-on-tip experiments running. Without you guys, absolutely impossible. All other members of the Poggio Group, which are namely Floris Braakman, Davide Cadeddu, Nicola Rossi, Panagiotis Fountas, Thibaud Ruelle, Simon Phillip, David Jaeger and Hinrich Mattiat. The former members, Benedikt Herzog, Dennis Weber and Michele Montinaro, who have already graduated and moved on. It was always fun with all of you at all the different BBQ evenings or as crazy FC Basel supporters in the famous Muttenserkerve in the St.Jakob stadium or somewhere else. The incredible mechanics shop at the University of Basel, in particular Sascha Martin, Stefan Gentsch and Patrick Stöcklin. Dominik Sifrig, who always gave me the important liquid helium. A big thank to the whole band and all the supporters, which make my life colorful. My whole family. Anna, who accompanied me on this way and has always taken me as I am.

Thanks to all the little and big heroes. Stand tall, stand proud in October 2018.

As you were ...

Bibliography

- [1] E. Beaurepaire, H. Bulou, F. Scheurer, K. Jean-Paul, Springer Proceedings in Physics **133**, Springer , Berlin (Germany) (2010).
- [2] J. L. Erskine, E. A. Stern, Phys. Rev. B **12**, 5016 (1975).
- [3] G. Schütz, W. Wagner, W. Willhelm, P. Kienle, R. Zeller, R. Frahm, and G. Materlik, Phys. Rev. Lett. **58**, 737 (1987).
- [4] J. Stöhr, Y. Wu, NATO ASI Series, Series E: Applied Sciences **254**, 221 (1994).
- [5] T. Tsukahara, et al., Japanese Journal of Applied Physics **56**, 060304 (2017).
- [6] T. J. Regan, H. Ohldag, C. Stamm, F. Nolting, J. Lüning, J. Stöhr, and R. L. Withe, Phys. Rev. B **64**, 214422 (2001).
- [7] F. Nolting, Magnetic Imaging with X-rays **133**, Berlin Heidelberg: Springer Verlag , 245-366 (2010).
- [8] L. Le Guyader, A. Kleibert, A. F. Rodríguez, S. E. Moussaoui, A. Balan, M. Buzzi, J. Raabe, and F. Nolting, J. Electron. Spectrosc. Relat. Phenom. **185**, 371 (2012).
- [9] J. Stöhr, S. Anders, IBM J. Res. Develop. **44**, (2000).
- [10] F. Kronast, J. Schlichting, F. Radu, S. K. Mishra, T. Noll, H. A. Dürr, Surface and Interface Analysis **42**, 1532 (2010).
- [11] U. Flechsig, F. Nolting, A. Frañl-Rodríguez, J. Krempasky, C. Quitmann, T. Schmidt, S. Spielmann, and D. Zimoch, AIP Conf. Proc. **1234**, 319 (2010).
- [12] B. H. Frazer, B. Gilbert, B. R. Sonderegger, G. De Stasio, Surface Science **537**, 161 (2003).
- [13] S. Anders, H.A. Padmore, R.M. Duarte, T. Renner, T. Stammel, A. Scholl, H.R. Scheinfein, J. Stöhr, L. Seve, and B. Sinkovic, Rev. Sci. Instrum. , **70**, 3973 (1999).
- [14] J. Stöhr, Y. Wu, B. D. Hermsmeier, M. G. Samant, G. R. Harp, S. Koranda, D. Dunham, and B. P. Tonner, Science **259**, 658 (1993).
- [15] E. Bauer, C. Koziol, G. Lilienkamp, and T. Schmidt, J. Electron. Spectrosc. Relat. Phenom. **84**, 201-209 (1997).
- [16] T. Schmidt, S. Heune, J. Slezak, J. Diaz, K.C. Prince, G. Lilienkamp, and E. Bauer, Surf. Rev. Lett. **5**, 1287 (1998).
- [17] R. Könenkamp, R.C. Word, G.F. Rempfer, T. Dixon, L. Almaraz, and T. Jones, Ultra-microscopy **110**, 899-902 (2010).

- [18] A. Farhan, P. M. Derlet, A. Kleibert, A. Balan, R.V. Chopdekar, M. Wyss, L. Anghinolfi, F. Nolting, and L.J. Heyderman, *Nature Physics* **9**, 375 (2013).
- [19] A. Farhan, P. M. Derlet, A. Kleibert, A. Balan, R.V. Chopdekar, M. Wyss, J. Perron, A. Scholl, F. Nolting, and L.J. Heyderman, *Phys. Rev. Lett.* **111**, 057204 (2013).
- [20] A. Farhan, A. Kleibert, P. M. Derlet, L. Anghinolfi, A. Balan, R. V. Chopdekar, M. Wyss, S. Gliga, F. Nolting, L. J. Heyderman, *Phys. Rev. B* **89**, 214405 (2014).
- [21] J. Bardeen, L. N. Cooper and J. R. Schrieffer, *Phys. Rev.* **5**, 1175–1204 (1957).
- [22] J. Clarke and A. I. Braginski, *The SQUID Handbook*, Wiley-VCH Weinheim (2004).
- [23] M. J. Martínez-Pérez, D. Kölle, *Phys. Sci. Rev* **2**, 20178001 (2017).
- [24] C. Granata, A. Vettoliere, *Physics Reports* **614**, 69 (2016).
- [25] F. London, *Superfluid*, Wiley-VCH New York (1950).
- [26] B. D. Josephson, *Phys. Lett.* **1**, 251-253 (1962).
- [27] R. F. Gasparovic, W. L. McLean, *Phys. Rev. B* **2**, 2519 (1970).
- [28] R. Gross, A. Marx, F. Deppe, *De Gruyter Textbook* 10:3110417065 (2005).
- [29] P. W. Anderson, and J. M. Rowell, *Phys. Rev. Lett.* **10**, 230-232 (1963).
- [30] D. D. Coon, and M. D. Fiske, *Phys. Rev.* **138**, A744 (1965).
- [31] R. Doll, and M. Näbauer, *Phys. Rev. Lett.* **7**, 51 (1961).
- [32] B. S. Deaver, and W. M. Fairbank, *Phys. Rev. Lett.* **7**, 43 (1961).
- [33] J. R. Kirtley et al., *arXiv:1605.09483* (2016).
- [34] A. Buchter, J. Nagel, D. Ruffer, F. Xue, D. P. Weber, O. F. Kieler, T. Weimann, J. Kohlmann, A. B. Zorin, E. Russo-Averchi, R. Huber, P. Berberich, A. Fontcuberta i Morral, M. Kemmler, R. Kleiner, D. Koelle, D. Grundler and M. Poggio, *Phys. Rev. Lett.* **111**, 067202 (2013).
- [35] D. J. Van Harlingen, J. Nagel, R. H. Koch, J. Clarke, *Appl. Phys. Lett.* **41**, 197 (1982).
- [36] D. D. Awschalom, J. R. Rozen, M. B. Ketchen, W. J. Gallagher, A. W. Kleinsasser, R. L. Sandstrom, B. Bumble *Appl. Phys. Lett.* **53**, 2108 (1988).
- [37] E. M. Levenson-Falk, R. Vijay, N. Antler, I. Siddiqi, *Superconductor Science and Technology* **26**, 5 (2013).
- [38] D. Vasyukov, Y. Anahory, L. Embon, D. Halbertal, J. C. Cuppens, L. Neeman, A. Finkler, Y. Segev, Y. Myasoedov, M. L. Rappaport, M. E. Huber, and E. Zeldov, *Nature Nanotechnology* **8**, 639 (2013).
- [39] A. Finkler, Y. Segev, Y. Myasoedov, M. L. Rappaport, M. L. Ne'eman, D. Vasyukov, E. Zeldov, M. E. Huber, J. Martin, *Nano Letters* **10**, 3 (2010).

- [40] D. Halbertal, J. Cuppens, M. B. Shalom, L. Embon, N. Shadmi, Y. Anahory, H. R. Naren, J. Sarkar, A. Uri, Y. Ronen, Y. Myasoedov, L. S. Levitov, E. Joselevich, A. K. Geim, E. Zeldov, *Nature* **539**, 407 (2016).
- [41] Y. Anahory, J. Reiner, L. Embon, D. Halbertal, A. Yakovenko, Y. Myasoedov, M. L. Rappaport, M. E. Huber, and E. Zeldov, *Nano Lett.* **14**, 6481 (2014).
- [42] A. Uri, A. Y. Meltzer, Y. Anahory, L. Embon, E. O. Lachman, D. Halbertal, H. R. Naren, Y. Myasoedov, M. E. Huber, A. F. Young, and E. Zeldov, *Nano Lett.* **16**, 6910 (2016).
- [43] L. Embon, Y. Anahory, A. Suhov, D. Halbertal, J. Cuppens, A. Yakovenko, A. Uri, Y. Myasoedov, M. L. Rappaport, M. E. Huber, A. Gurevich and E. Zeldov, *Scientific Reports* **5**, 7598 (2015).
- [44] E. O. Lachman, A. F. Young, A. Richardella, J. Cuppens, H. R. Naren, Y. Anahory, A. Y. Meltzer, A. Kandala, S. Kempinger, Y. Myasoedov, M. E. Huber, N. Samarth and E. Zeldov, *Science Advances* **1**, e1500740 (2015).
- [45] Y. Anahory, L. Embon, C. J. Li, S. Banerjee, A. Meltzer, A. Naren, A. Y. Yakovenko, J. Cuppens, Y. Myasoedov, M. L. Rappaport, M. E. Huber, K. Michaeli, T. Venkatesan, Ariando and E. Zeldov, *Nature Communications* **7**, 12566 (2016).
- [46] N. Yabuki, R. Moriya, M. Arai, Y. Sata, S. Morikawa, S. Masubuchi, T. Machida, *Nature Communications* **7**, 10616 (2016).
- [47] I. Petkovic, M. Aprili, S. E. Barnes, F. Beuneu, S. Maekawa, *Phys. Rev. B* **80**, 22 (2009).
- [48] E. Meyer, H. J. Hug, R. Bennewitz, *Scanning Probe Microscopy*, Springer, Berlin Heidelberg (2004).
- [49] G. Binnig, H. Rohrer, C. Gerber, E. Weibel, *Phys. Rev. Lett.* **49**, 57 (1982).
- [50] G. Binnig, C. F. Quate, C. Gerber, *Phys. Rev. Lett.* **56**, 930 (1986).
- [51] Y. Martin, H. K. Wickramasinghe, *Appl. Phys. Lett.* **20**, 1455 (1987).
- [52] I. Schmid, M. A. Marioni, P. Kappenberger, S. Romer, M. Parlinska-Wojtan, H. J. Hug, O. Hellwig, M. J. Carrey and E. E. Fullerton, *Phys. Rev. Lett.* **105**, 197201 (2010).
- [53] R. P. Welty, J. M. Martinis, *IEEE Transactions on Magnetics* **27**, 2 (1991).
- [54] C. L. Degen, M. Poggio, H. J. Mamin, C. T. Rettner, and D. Rugar, *Proceedings of the National Academy of Sciences* **106**, 1313 (2009).
- [55] C. L. Degen, *Appl. Phys. Lett.* **92**, 243111 (2008).
- [56] P. Maletinsky, S. Hong, M. S. Grinold, B. Hausmann, M. D. Lukin, R. L. Walsworth, M. Loncar, and A. Yacoby, *Nature Nanotechnology* **7**, 320 (2012).
- [57] A. Lupaşcu, C. J. M. Verwijs, R. N. Schouten, C. J. P. M. Harmans, and J. E. Mooij, *Phys. Rev. Lett.* **93**, 177006 (2004).

- [58] D. Ruffer, M. Slot, R. Huber, T. Schwarze, F. Heimbach, G. Tütüncüoğlu, F. Matteini, E. Russo-Averchi, A. Kovács, R. Dunin-Borkowski, R. R. Zamani, J. R. Morante, J. Arbiol, A. F. i. Morral, and D. Grundler, *APL Mater.* **2**, 076112 (2014).
- [59] B. Gross, D. P. Weber, D. Ruffer, A. Buchter, F. Heimbach, A. Fontcuberta i Morral, D. Grundler, and M. Poggio, *Phys. Rev. B* **93**, 064409 (2016) .
- [60] A. Mehlin, B. Gross, M. Wyss, T. Schefer, G. Tütüncüoğlu, F. Heimbach, A. Fontcuberta i Morral, D. Grundler, and M. Poggio, *Phys. Rev. B* **97**, 134422 (2018) .
- [61] J. A. Katine, M. K. Ho, Y. S. Ju, and C. T. Rettner, *Appl. Phys. Lett.* **83**, 401 (2003).
- [62] S. Khizroev and D. Litvinov, *Nanotechnology* **15**, R7 (2004).
- [63] C. O. Knutson, Magnetic domain wall dynamics in nanoscale thin film structures, UT Electronic Theses and Dissertations, University of Texas at Austin (2008).
- [64] A. Buchter, R. Wölbing, M. Wyss, O. F. Kieler, T. Weimann, J. Kohlmann, A. B. Zorin, D. Ruffer, F. Matteini, G. Tütüncüoğlu, F. Heimbach, A. Kleibert, A. Fontcuberta i Morral, D. Grundler, R. Kleiner, D. Koelle, and M. Poggio, *Phys. Rev. B* **92**, 214432 (2015).
- [65] A. Buchter, University of Basel **11582**, Doctoral Thesis (2015).
- [66] S. P. Parkin, and S. - H. Yang, *Nature Nanotechnology* **10**, 195 (2015).
- [67] S. P. Parkin, M. Hayashi, and L. Thomas, *Science* **320**, 5873 (2008).
- [68] Y. Zheng, J.-G. Zhu, *Journal of Applied Physics* **81**, 5471 (1997).
- [69] O. Fruchart, J.-P. Nozieres, W. Wernsdorfer, D. Givord, F. Rousseaux, D. Decanini, *Phys. Rev. Lett.* **82**, 1305 (1999).
- [70] R. P. Cowburn and M. E. Welland, *Science* **287**, 1466 (2000).
- [71] M. M. Maqableh, X. Huang, S.-Y. Sung, K. S. M. Reddy, G. Norby, R. H. Victora, and B. J. H. Stadler, *Nano Lett.* **12**, 4102 (2012).
- [72] S. Khizroev, M. H. Kryder, D. Litvinov, and D. A. Thompson, *Appl. Phys. Lett.* **81**, 2256 (2002).
- [73] M. Poggio and C. L. Degen, *Nanotechnology* **21**, 342001 (2010).
- [74] H. Campanella, M. Jaafar, J. Llobet, J. Esteve, M. Vázquez, A. Asenjo, R. P. d. Real, and J. A. Plaza, *Nanotechnology* **22**, 505301 (2011).
- [75] P. Landeros, O. J. Suarez, A. Cuchillo, and P. Vargas, *Phys. Rev. B* **79**, 024404 (2009).
- [76] M. Daub, M. Knez, U. Goesele, and K. Nielsch, *J. Appl. Phys.* **101**, 09J111 (2007).
- [77] Z. K. Wang, H. S. Lim, H. Y. Liu, S. C. Ng, M. H. Kuok, L. L. Tay, D. J. Cottam, K. L. Hobbs, P. R. Larson, J. C. Keay, G. D. Lian, and M. B. Johnson, *Phys. Rev. Lett.* **94**, 137208 (2005).

- [78] J. Escrig, P. Landeros, P. Altbir, E. E. Vogel, P. Vargas, *Journal of Magnetism and Magnetic Materials* **308**, 233 (2007).
- [79] J. Escrig, P. Landeros, P. Altbir, and E. E. Vogel, *Journal of Magnetism and Magnetic Materials* **310**, 2448 (2007).
- [80] A. P. Chen, N. A. Usov, J. M. Blanco, and J. Gonzalez, *J. Magn. Magn. Mater.* **316**, e317 (2007).
- [81] A.-P. Chen, J. M. Gonzalez, and K. Y. Guslienko, *J. Appl. Phys.* **109**, 073923 (2011).
- [82] A. P. Chen, K. Y. Guslienko, and J. Gonzalez, *J. Appl. Phys.* **108**, 083920 (2010).
- [83] D. Li, R. S. Thompson, G. Bergmann, and J. G. Lu, *Adv. Mater.* **20**, 4575 (2008).
- [84] D. Ruffer, R. Huber, P. Berberich, S. Albert, E. Russo-Averchi, M. Heiss, J. Arbiol, A. F. i. Morral, and D. Grundler, *Nanoscale* **4**, 4989 (2012).
- [85] D. P. Weber, D. Ruffer, A. Buchter, F. Xue, E. Russo-Averchi, R. Huber, P. Berberich, J. Arbiol, A. Fontcuberta i Morral, D. Grundler, and M. Poggio, *Nano Lett.* **12**, 6139 (2012).
- [86] R. Streubel, J. Lee, D. Makarov, M.-Y. Im, D. Karanushenko, L. Han, R. Schäfer, P. Fischer, S.-K. Kim, and O. G. Schmidt, *Adv. Mater.* **26**, 316 (2014).
- [87] R. Streubel, L. Han, F. Kronast, A. A. Ünal, O. G. Schmidt, and D. Makarov, *Nano Lett.* **14**, 3981 (2014).
- [88] R. Streubel, F. Kronast, P. Fischer, D. Parkinson, O. G. Schmidt, and D. Makarov, *Nat. Commun.* **6** (2015).
- [89] J. Lee, D. Suess, T. Schrefl, K. H. Oh, and J. Fidler, *J. Magn. Magn. Mater.* **310**, 2445 (2007).
- [90] X. F. Han, Z. C. Wen, and H. X. Wei, *J. Appl. Phys.* **103**, 07E933 (2008).
- [91] S. Jamet, S. Da Col, N. Rougemaille, A. Wartelle, A. Locatelli, T. O. Montes, B. Santos Burgos, R. Afid, L. Cagnon, S. Bochmann, J. Bachmann, O. Fruchart, and J. C. Toussaint, *Phys. Rev. B* **92**, 144428 (2015).
- [92] S. Da Col, S. Jamet, N. Rougemaille, A. Locatelli, T. O. Montes, B. S. Burgos, R. Afid, M. Darques, L. Cagnon, J. C. Toussaint, and O. Fruchart, *Phys. Rev. B* **89**, 180405 (2014).
- [93] N. A. Usov, A. Zhukov, and J. Gonzalez, *J. Magn. Magn. Mater.* **316**, 255 (2007).
- [94] D. Vasyukov, L. Ceccarelli, M. Wyss, B. Gross, A. Schwarb, A. Mehlin, N. Rossi, G. Tütüncüoğlu, F. Heimbach, R. R. Zamani, A. Kovács, A. Fontcuberta i Morral, D. Grundler, and M. Poggio, *Nano Lett.* **18**, 964 (2018).
- [95] P. Landeros, S. Allende, J. Escrig, E. Salcedo, D. Altbir, and E. E. Vogel, *Appl. Phys. Lett.* **90**, 102501 (2007).

- [96] P. Landeros and A. S. Núñez, *Journal of Applied Physics* **108**, 033917 (2010).
- [97] D. Rueffer, Lausanne, EPFL **6316**, PhD thesis (2014).
- [98] Y. Gaididei, V. P. Kravchuk, and D. D. Sheka, *Phys. Rev. Lett.* **112**, 257203 (2014).
- [99] R. Streubel, P. Fischer, F. Kronast, V. P. Kravchuk, D. D. Sheka, Yuri Gaididei, O. G. Schmidt, and D. Makarov, *J. Phys. D: Appl. Phys.* **49**, 363001 (2016).
- [100] J. A. Otálora, M. Yan, H. Schultheiss, R. Hertel, and A. Kákay, *Phys. Rev. Lett.* **117**, 227203 (2016).
- [101] M. Yan, A. Kákay, C. Andreas, and R. Hertel, *Phys. Rev. B* **88**, 220412 (2013).
- [102] Y. C. Sui, R. Skomski, K. D. Sorge, and D. J. Sellmayer, *Appl. Phys. Lett.* **84**, 1525 (2004).
- [103] K. Nielsch, F. J. Castaño, C. A. Ross, and R. Krishnan, *J. Appl. Phys.* **98**, 034318 (2005).
- [104] A. T. Hindmarch, C. J. Kinane, M. MacKenzie, J. N. Chapman, M. Henini, D. Taylor, D. A. Arena, J. Dvorak, B. J. Hickey, and C. H. Marrows, *Phys. Rev. Lett.* **100**, 117201 (2008).
- [105] T. Schwarze and D. Grundler, *Appl. Phys. Lett.* **102**, 222412 (2013).
- [106] K. Baumgaertl, F. Heimbach, S. Maendl, D. Rueffer, A. Fontcuberta i Morral, and D. Grundler, *Appl. Phys. Lett.* **108** (2016).
- [107] J. Kimling, F. Kronast, S. Martens, T. Böhnert, M. Martens, J. Herrero-Albillos, L. Tati-Bismaths, U. Merkt, K. Nielsch, and G. Meier, *Phys. Rev. B* **84**, 174406 (2011).
- [108] A. Vansteenkiste, J. Leliaert, M. Dvornik, M. Helsen, F. Garcia-Sanchez, and B. Van Waeyenberge, *AIP Adv.* **4**, 107133 (2014).
- [109] W. F. Giaque, M. F. Ashley, *Phys. Rev.* **43**, 81 (1933).
- [110] W. F. Giaque, J. W. Stout, *J. Am. Chem. Soc.* **58**, 1144 (1936).
- [111] L. Pauling, *J. Am. Chem. Soc.* **57**, 2680 (1935).
- [112] J. D. Bernal, R. H. Fowler, *The Journal of Chemical Physics* **1**, 515 (1933).
- [113] M. J. Harris, S. T. Bramwell, D. F. McMorrow, D. F. Zeiske, K. W. Godfrey, *Phys. Rev. Lett.* **79**, 2554 (1997).
- [114] R. F. Wang, C. Nisoli, R. S. Freitas, J. Li, W. McConville, B. J. Cooley, M. S. Lund, N. Samarth, C. Leighton, V. H. Crespi, and P. Schiffer, *Nature* **439**, 303 (2006).
- [115] I. Gilbert, Y. Lao, I. Carrasquillo, L. O'Brien, J. D. Watts, M. Manno, C. Leighton, A. Scholl, C. Nisoli, P. Schiffer, *Nature Physics* **12**, 162 (2016).
- [116] C. Nisoli, arXiv:1711.00921 (2017).

- [117] M. J. Morrison, T. R. Nelson, C. Nisoli, *New Journal of Physics* **4**, 045009 (2013).
- [118] J. P. Morgan, A. Stein, S. Langridge, C. H. Marrows, *Nature Physics* **7**, 75 (2010).
- [119] S. Ladak, D. E. Read, G. K. Perkins, L. F. Cohen, and W. R. Branford, *Nature Physics* **6**, 359 (2010).
- [120] C. Phatak, A. K. Petford-Long, O. Heinonen, M. Tanase, M. De Graef, *Physical Review B* **83**, 5 (2011).
- [121] S. Gliga, G. Hrkac, C. Donnelly, J. Buchi, A. Kleibert, J. Cui, A. Farhan, E. Kirk, R. V. Chopdekar, Y. Masaki, N. S. Bingham, A. Scholl, R. L. Stamps, L. J. Heyderman, *Nat Mater* **16**, 1106 (2017).
- [122] S. T. Bramwell, *Nat Mater* **16**, 1053 (2017).
- [123] E. Mengotti, L. J. Heyderman, A. F. Rodriguez, F. Nolting, R. V. Hugli, H. B. Braun, *Nat Phys* **7**, 68 (2011).
- [124] S. Gliga, A. Kakay, L. J. Heyderman, R. Hertel, O. Heinonen, *Phys. Rev. B* **92**, 5 (2015).
- [125] S. Gliga, A. Kakay, R. Hertel, O. Heinonen, *Phys. Rev. Lett.* **110**, 117205 (2013).
- [126] E. Iacocca, S. Gliga, R. L. Stamps, O. Heinonen, *Phys. Rev. B* **93**, 134420 (2016).
- [127] E. Iacocca, O. Heinonen, *Physical Review Applied* **8**, 034015 (2017).
- [128] J. Drisko, T. Marsh, J. Cumings, *Nature Communication* **8**, 14009 (2017).
- [129] M. B. Jungfleisch, W. Zhang, E. Iacocca, J. Sklenar, J. Ding, W. Jiang, S. Zhang, J. E. Pearson, V. Novosad, J. B. Ketterson, O. Heinonen, A. Hoffman, *Phys. Rev. B* **93**, 100401(R) (2016).
- [130] J. Nagel, O. F. Kieler, T. Weimann, R. Wölbing, J. Kohlmann, A. B. Zorin, R. Kleiner, D. Koelle, *Appl. Phys. Lett.* **99**, 032506 (2011).
- [131] R. Wölbing, J. Nagel, T. Schwarz, O. Kieler, T. Weimann, J. Kohlmann, A. B. Zorin, M. Kemmler, R. Kleiner, D. Koelle, *Appl. Phys. Lett.* **102**, 192601 (2013).
- [132] J. Dai, R. Kometani, K. Onomitsu, Y. Krockenberger, H. Yamaguchi, I. Sunao, S. Warisawa, *Journal of Micromechanics and Microengineering* **24**, 055015 (2014).
- [133] J. W. Gibson, R. A. Hein, *Phys. Rev. Lett.* **12**, 688 (1964).
- [134] E. S. Sadki, S. Ooi, K. Hirata, *Appl. Phys. Lett.* **85**, 6206 (2004).
- [135] J. Dai, K. Onomitsu, R. Kometani, Y. Krockenberger, H. Yamaguchi, S. Ishihara, S. Warisawa, *Japanese Journal of Applied Physics* **52**, 075001 (2013).
- [136] M. Stano, S. Schaefer, A. Wartelle, M. Rioult, R. Belkhou, A. Sala, T. O. Mentès, A. Locatelli, L. Cagnon, B. Trapp, S. Bochmann, S. Martin, E. Gautier, J.-C. Toussaint, W. Ensinger and O. Fruchart, *arXiv:1704.06614* (2017).

- [137] M. Zimmermann, T. N. G. Meier, F. Dirnberger, A. Kákay, M. Decker, S. Wintz, S. Finizio, E. Josten, J. Raabe, M. Kronseder, D. Bougeard, J. Lindner, C. H. Back, *Nano Lett.* **18**, 2828 (2018).
- [138] J. Raabe, G. Tzvetkov, U. Flechsig, M. Böge, A. Jaggi, B. Sarafimov, M. G. C. Vernooij, T. Huthwelker, H. Ade, D. Kilcoyne, T. Tyliczszak, R. H. Fink, C. Quitmann, *Review of Scientific Instruments* **79**, 113704 (2008).
- [139] M. Zimmermann, Static and dynamic properties of hexagonally shaped magnetic nanotubes , 37820 (2018).
- [140] B. Rössner, F. Koch, F. Döring, V. A. Guzenko, M. Meyer, J. L. Ornelas, A. Späth, R. H. Fink, S. Stanescu, S. Swaraj, R. Belkhou, B. Watts, J. Raabe, C. David, *Microsc. Microanal.* **24**, 270 (2018)

Appendix A.

A: XMCD-PEEM Measurements

A.1. XMCD-PEEM sample holder

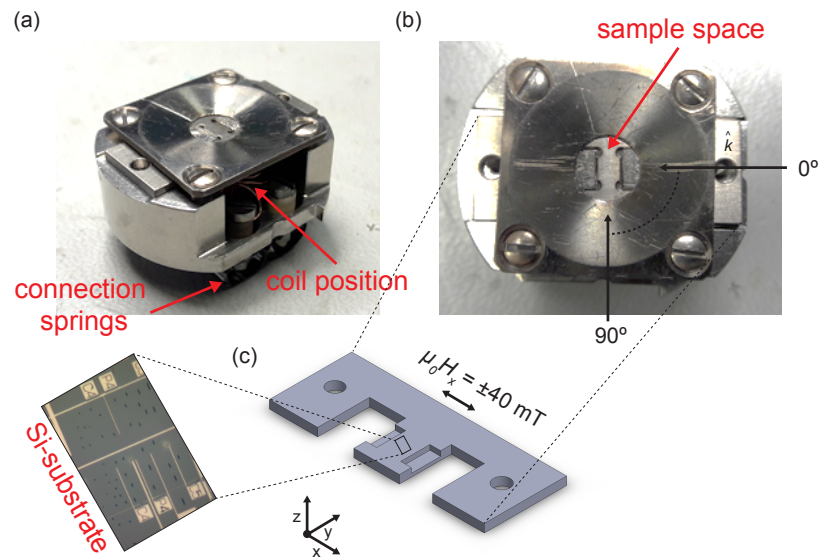


Figure A.1. | Image of the used PEEM sample holder for the XMCD-PEEM measurements described in chapter 3 from the side in (a) and from the top in (b). In (b) the direction of the incoming wave vector \hat{k} before at 0° and after rotation of the holder to 90° is depicted as a black arrow. In (c) the especially for the XMCD-PEEM measurement designed holder for the sample is shown. The silicon substrate with the on top placed CoFeB and Py NTs was mounted on the middle arm between two pole pieces of almost pure iron. The coil, located underneath the middle arm, which entwined the pure iron allows to apply a homogeneous magnetic field of $\mu_0 H_x = \pm 40 \text{ mT}$ to the sample space at room temperature and under ultra-high vacuum (UHV) conditions.

A.2. XMCD-PEEM, PEEM, and SEM images

Adapted from:

M. Wyss, A. Mehlin, B. Gross, A. Buchter, A. Farhan, M. Buzzi, A. Kleibert, G. Tütüncüoğlu, F. Heimbach, A. Fontcuberta i Morral, D. Grundler, and M. Poggio 'Imaging magnetic vortex configurations in ferromagnetic nanotubes', Phys. Rev. B **96**, 024423 (2017)

XMCD-PEEM, PEEM, and SEM images of CoFeB and Py NTs

XMCD-PEEM images (top left), SEMs (bottom left), and PEEM images (right) recorded with σ^- polarized x-rays for each measured CoFeB NT. The dashed lines show the position of the NT as taken from SEM. The corresponding phase diagram is shown in Figure B.1 (a).
 •: matching vortices. •: opposing vortices. •: relative vortex circulation switched after applying a field of ± 40 mT along \hat{n} . ⊙: matching vortices before and after applying a field of ± 40 mT along \hat{n} . ⊙: opposing vortex circulation before and after applying a field of ± 40 mT along \hat{n} .

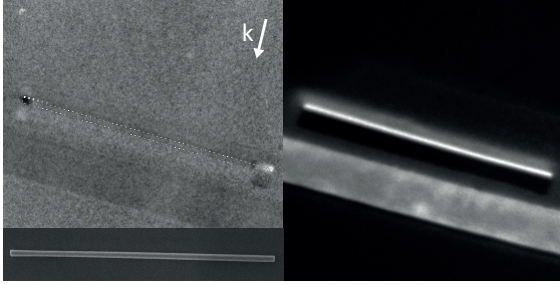


Figure A.2. | • : $l = 11.3 \mu\text{m}$, $d = 300 \text{ nm}$.
CoFeB.

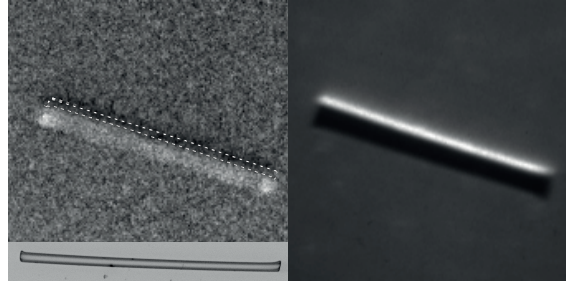


Figure A.3. | • : $l = 7.24 \mu\text{m}$, $d = 265 \text{ nm}$.
CoFeB.

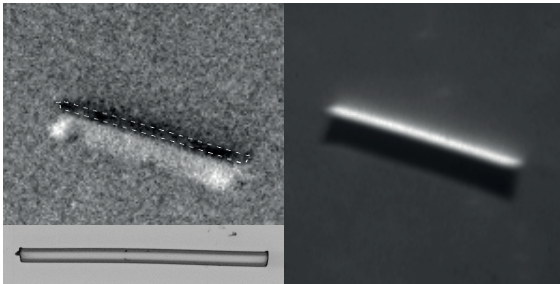


Figure A.4. | • : $l = 5.15 \mu\text{m}$, $d = 314 \text{ nm}$.
CoFeB.

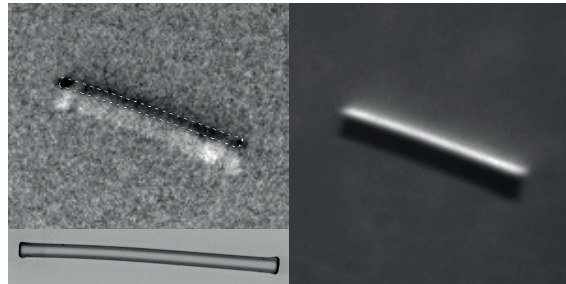


Figure A.5. | • : $l = 5.09 \mu\text{m}$, $d = 276 \text{ nm}$.
CoFeB.

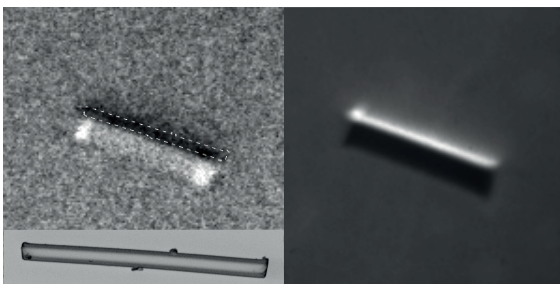


Figure A.6. | • : $l = 4.06 \mu\text{m}$, $d = 305 \text{ nm}$.
CoFeB.

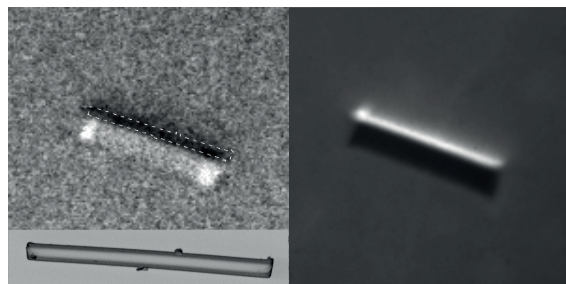


Figure A.7. | ⊙ : $l = 3.65 \mu\text{m}$, $d = 265 \text{ nm}$.
CoFeB.

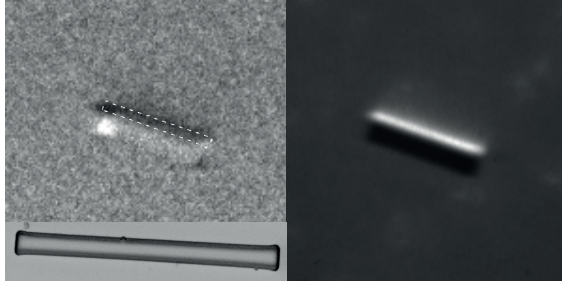


Figure A.8. | ● : $l = 3.14 \mu\text{m}$, $d = 270 \text{ nm}$.
CoFeB.

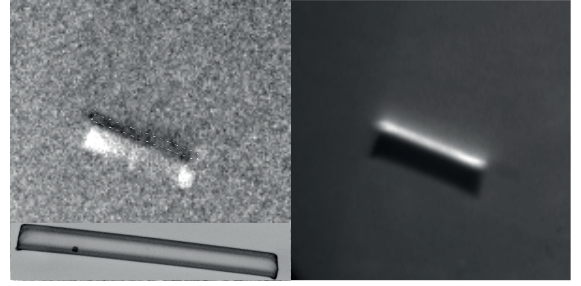


Figure A.9. | ● : $l = 3.07 \mu\text{m}$, $d = 285 \text{ nm}$.
CoFeB.

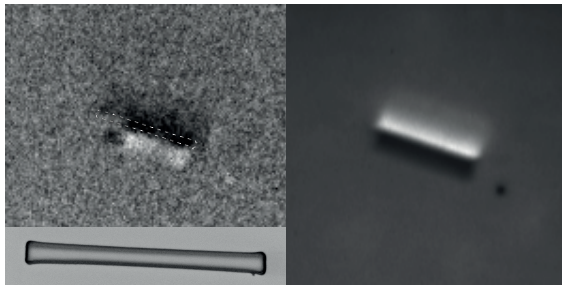


Figure A.10. | ● : $l = 2.87 \mu\text{m}$, $d = 227 \text{ nm}$.
CoFeB.

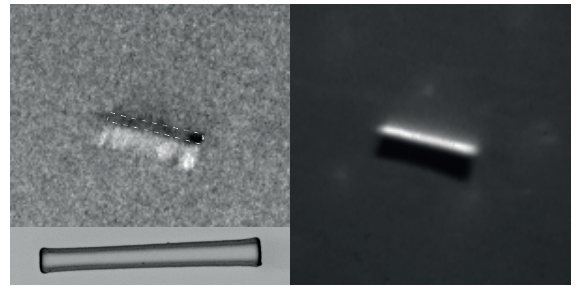


Figure A.11. | ● : $l = 2.61 \mu\text{m}$, $d = 289 \text{ nm}$.
CoFeB.

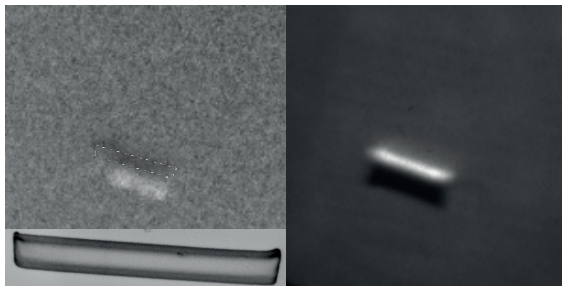


Figure A.12. | ● : $l = 2.18 \mu\text{m}$, $d = 279 \text{ nm}$.
CoFeB.

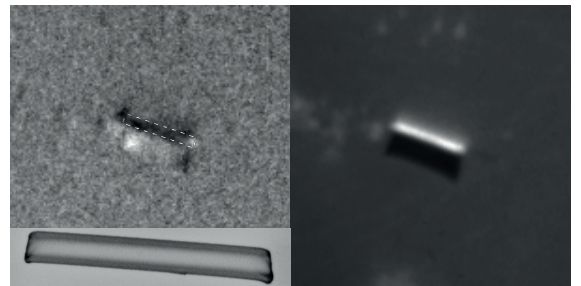


Figure A.13. | ● : $l = 2.03 \mu\text{m}$, $d = 272 \text{ nm}$.
CoFeB.

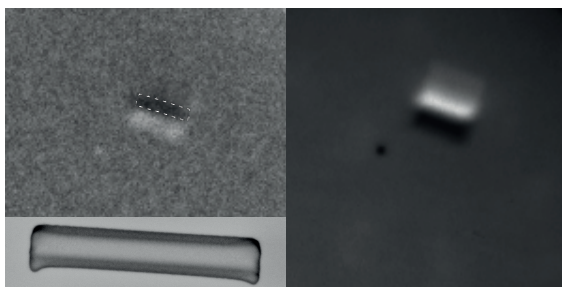


Figure A.14. | ● : $l = 1.57 \mu\text{m}$, $d = 283 \text{ nm}$.
CoFeB.

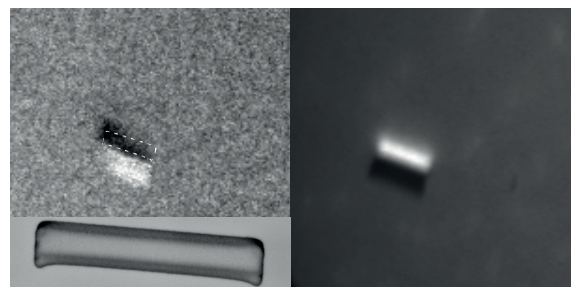


Figure A.15. | ● : $l = 1.57 \mu\text{m}$, $d = 285 \text{ nm}$.
CoFeB.

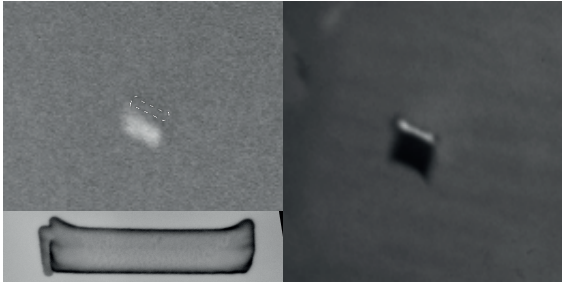


Figure A.16. | \odot : $l = 1.18 \mu\text{m}$, $d = 248 \text{ nm}$.
CoFeB.

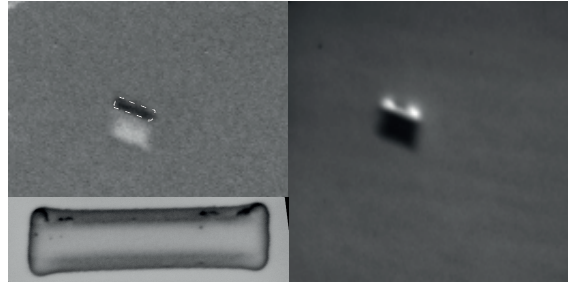


Figure A.17. | \odot : $l = 1.06 \mu\text{m}$, $d = 283 \text{ nm}$.
CoFeB.

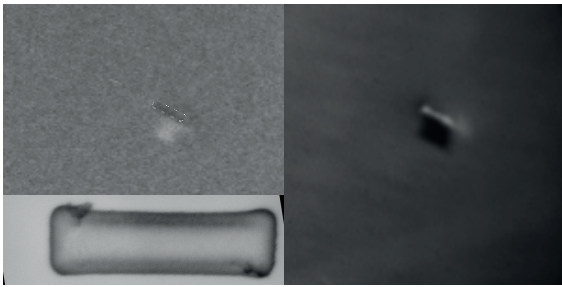


Figure A.18. | \bullet : $l = 0.83 \mu\text{m}$, $d = 236 \text{ nm}$.
CoFeB.

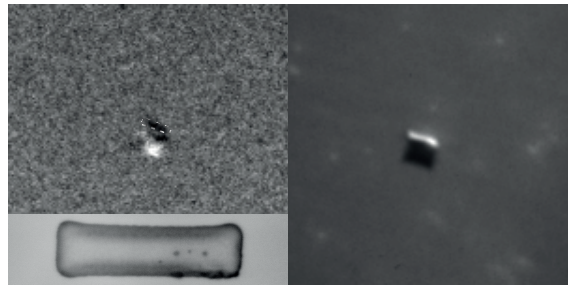


Figure A.19. | \bullet : $l = 0.80 \mu\text{m}$, $d = 228 \text{ nm}$.
CoFeB.

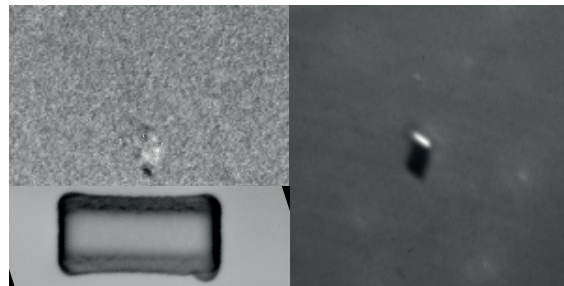


Figure A.20. | \odot : $l = 0.54 \mu\text{m}$, $d = 293 \text{ nm}$.
CoFeB.

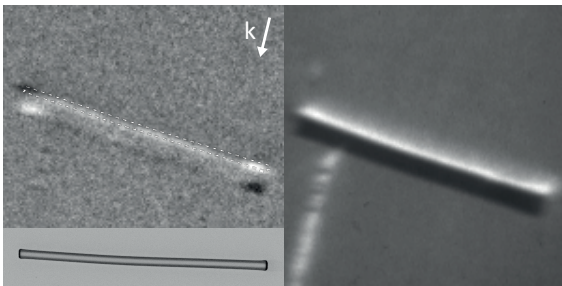


Figure A.21. | \bullet : $l = 6.90 \mu\text{m}$, $d = 243 \text{ nm}$. Py.

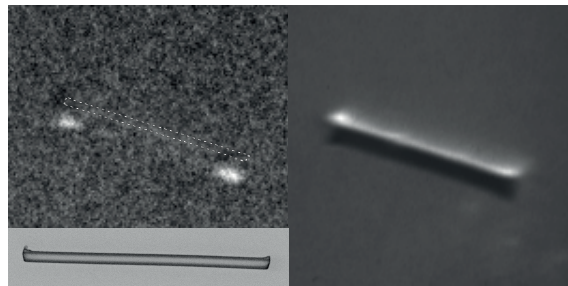


Figure A.22. | \bullet : $l = 5.13 \mu\text{m}$, $d = 234 \text{ nm}$. Py.

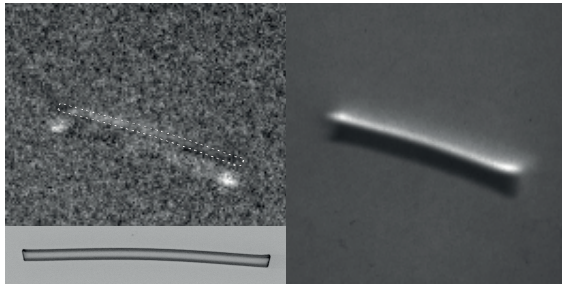


Figure A.23. | ● : $l = 5.10 \mu\text{m}$, $d = 242 \text{ nm}$. Py.

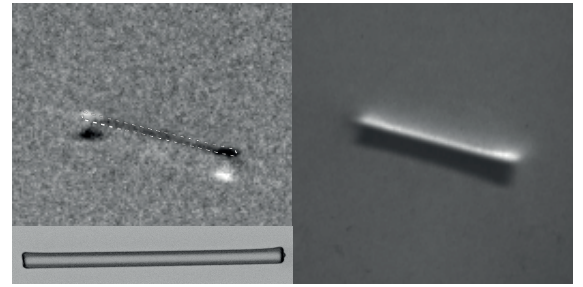


Figure A.24. | ● : $l = 4.34 \mu\text{m}$, $d = 239 \text{ nm}$. Py.

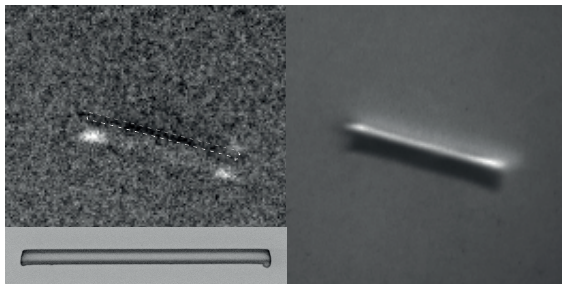


Figure A.25. | ● : $l = 4.15 \mu\text{m}$, $d = 258 \text{ nm}$. Py.

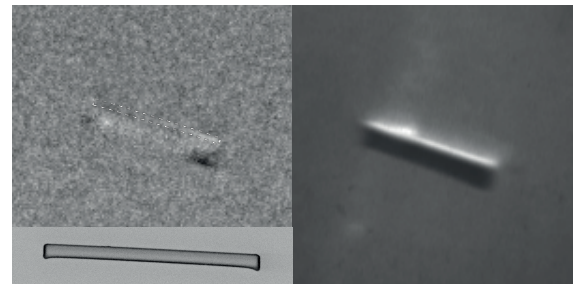


Figure A.26. | ● : $l = 3.63 \mu\text{m}$, $d = 212 \text{ nm}$. Py.

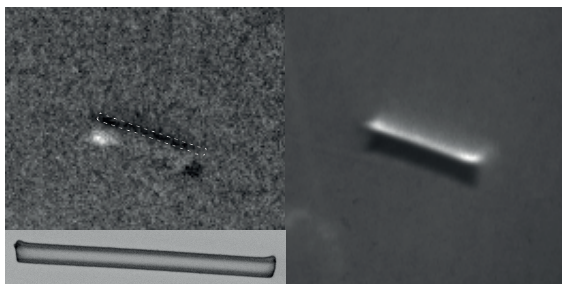


Figure A.27. | ⊙ : $l = 3.07 \mu\text{m}$, $d = 228 \text{ nm}$. Py.

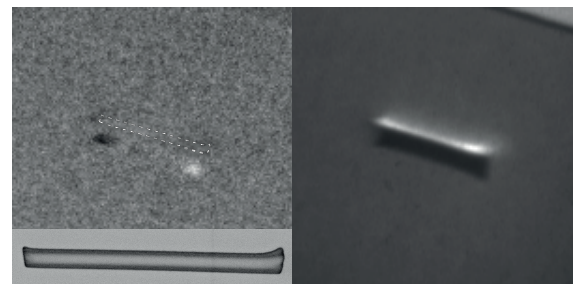


Figure A.28. | ● : $l = 3.05 \mu\text{m}$, $d = 223 \text{ nm}$. Py.

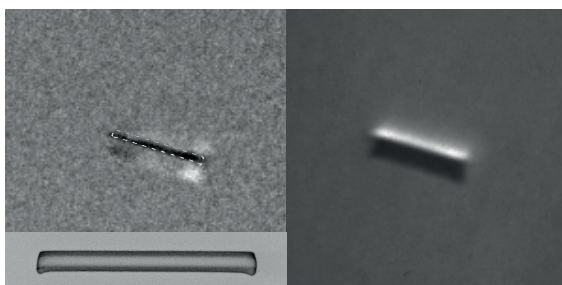


Figure A.29. | ⊙ : $l = 2.58 \mu\text{m}$, $d = 251 \text{ nm}$. Py.

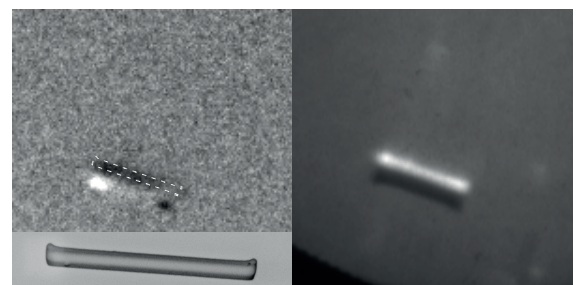


Figure A.30. | ● : $l = 2.47 \mu\text{m}$, $d = 215 \text{ nm}$. Py.

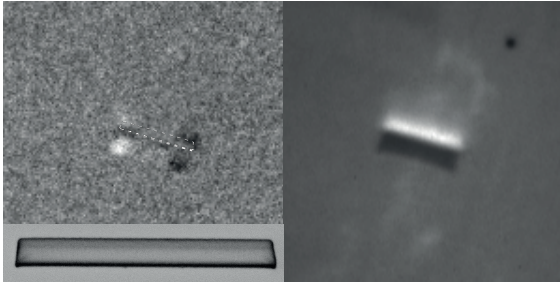


Figure A.31. | ● : $l = 2.13 \mu\text{m}$, $d = 212 \text{ nm}$. Py.

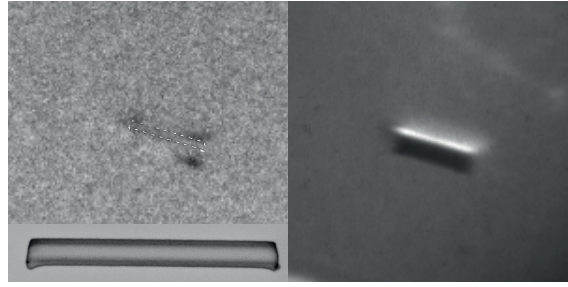


Figure A.32. | ● : $l = 2.07 \mu\text{m}$, $d = 225 \text{ nm}$. Py.

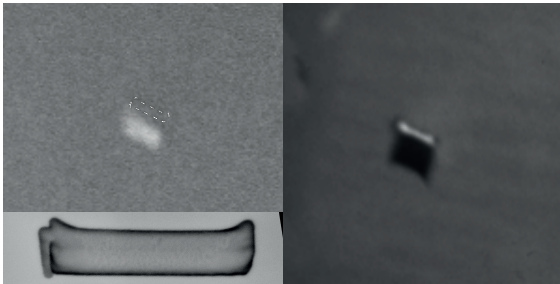


Figure A.33. | ● : $l = 1.86 \mu\text{m}$, $d = 209 \text{ nm}$. Py.

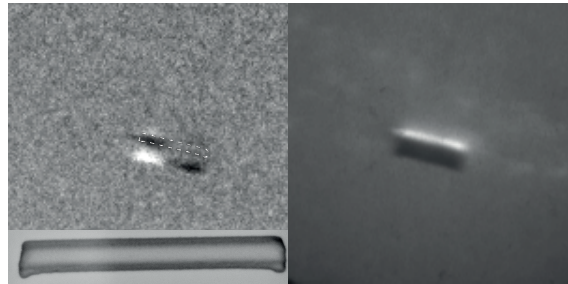


Figure A.34. | ● : $l = 1.85 \mu\text{m}$, $d = 211 \text{ nm}$. Py.

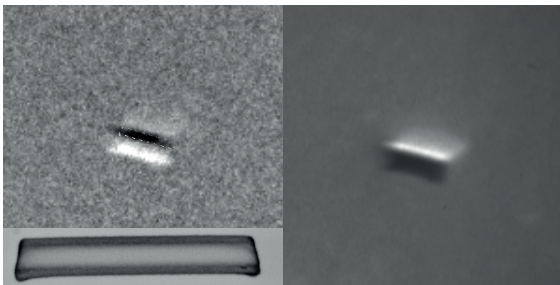


Figure A.35. | ● : $l = 1.53 \mu\text{m}$, $d = 237 \text{ nm}$. Py.

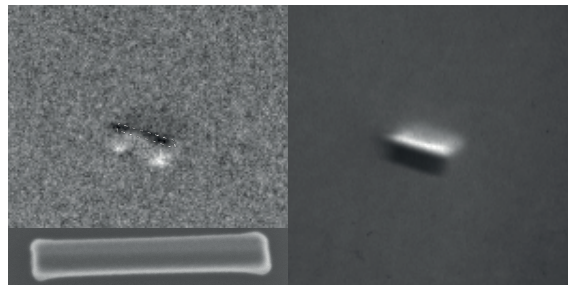


Figure A.36. | ○ : $l = 1.53 \mu\text{m}$, $d = 215 \text{ nm}$. Py.

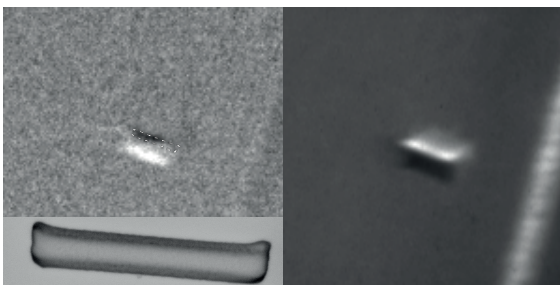


Figure A.37. | ○ : $l = 1.33 \mu\text{m}$, $d = 215 \text{ nm}$. Py.

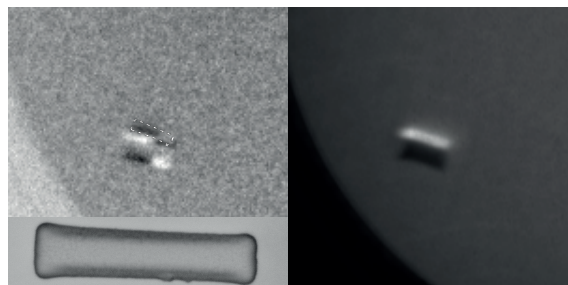


Figure A.38. | ● : $l = 1.24 \mu\text{m}$, $d = 265 \text{ nm}$. Py.

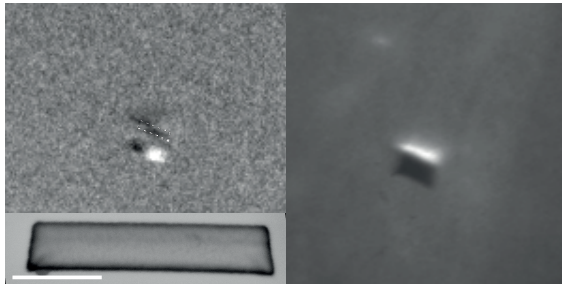


Figure A.39. | ● : $l = 1.09 \mu\text{m}$, $d = 211 \text{ nm}$. Py.

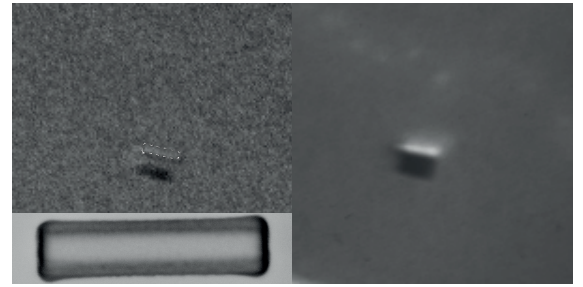


Figure A.40. | ● : $l = 1.02 \mu\text{m}$, $d = 259 \text{ nm}$. Py.

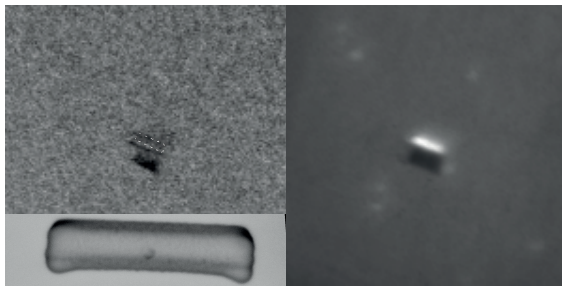


Figure A.41. | ○ : $l = 0.92 \mu\text{m}$, $d = 221 \text{ nm}$. Py.

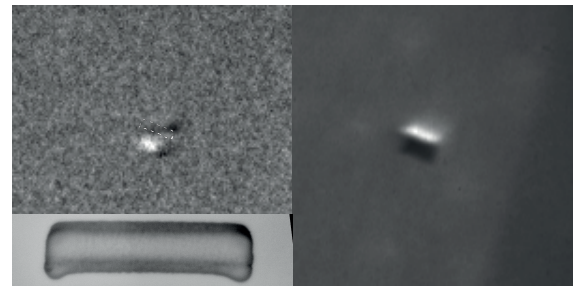


Figure A.42. | ● : $l = 0.90 \mu\text{m}$, $d = 221 \text{ nm}$. Py.

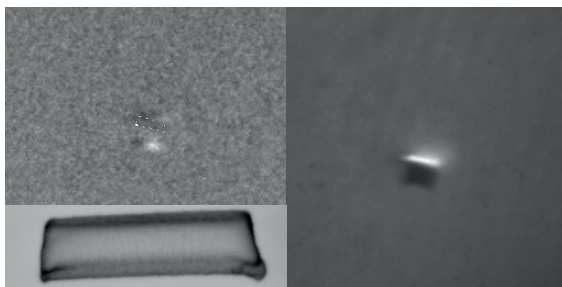


Figure A.43. | ○ : $l = 0.77 \mu\text{m}$, $d = 237 \text{ nm}$. Py.

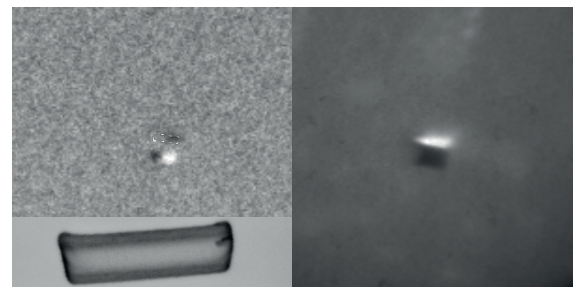


Figure A.44. | ● : $l = 0.73 \mu\text{m}$, $d = 221 \text{ nm}$. Py.

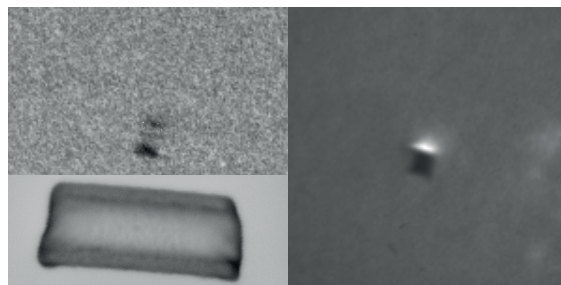


Figure A.45. | ○ : $l = 0.58 \mu\text{m}$, $d = 244 \text{ nm}$. Py.

Appendix B.

B: Phase Diagrams of the XMCD-PEEM Measurements

Adapted from:

M. Wyss, A. Mehlin, B. Gross, A. Buchter, A. Farhan, M. Buzzi, A. Kleibert, G. Tütüncüoğlu, F. Heimbach, A. Fontcuberta i Morral, D. Grundler, and M. Poggio
'Imaging magnetic vortex configurations in ferromagnetic nanotubes',
Phys. Rev. B **96**, 024423 (2017)

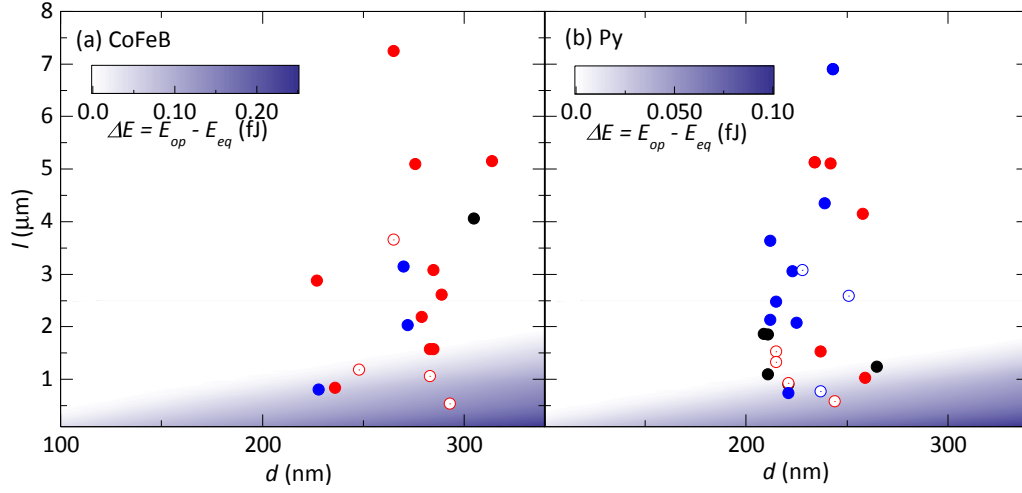


Figure B.1. | Phase diagrams of relative vortex circulation for (a) CoFeB and (b) Py. Numerically calculated $\Delta E = E_{op} - E_{eq}$ is plotted in the color scale as a function of NT diameter d and length l . E_{op} (E_{eq}) represents the energy of an equilibrium configuration with opposing (matching) circulation. Regions of $\Delta E > 0$ (shaded) show where end vortices with matching circulation are likely, while regions of $\Delta E \approx 0$ (white) show where vortices with matching or opposing circulation are equally likely. Data points represent remnant states measured in real NTs by XMCD-PEEM. ●: matching vortices. ●: opposing vortices. ●: relative vortex circulation switched after applying a field of ± 40 mT along \hat{n} . ○: matching vortices before and after applying a field of ± 40 mT along \hat{n} . ○: opposing vortices before and after applying a field of ± 40 mT along \hat{n} .

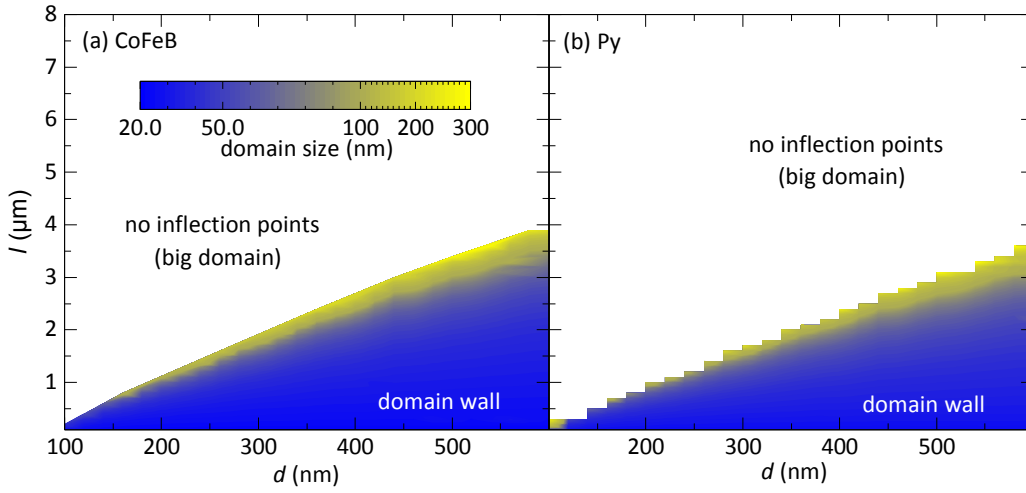


Figure B.2. | Phase diagrams for (a) CoFeB and (b) Py NTs considering only opposing circulation magnetization configurations. The size of the central axial domain is plotted in the color scale and is calculated using the distance between inflection points in the order parameter $M_n/|M|$ along \hat{n} . A clear boundary between a mixed state with opposing vortex circulation and an opposing vortex state can be identified.

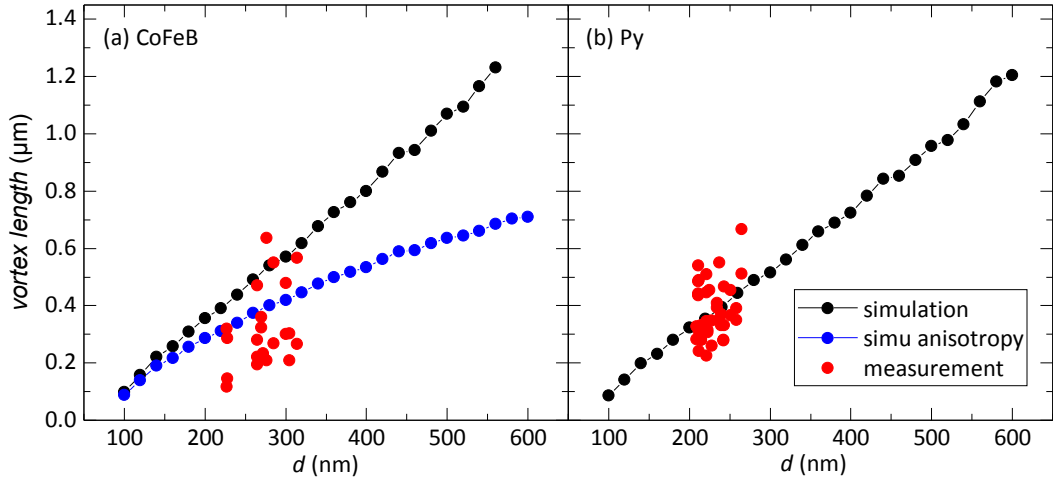


Figure B.3. | Length of the end vortices for (a) CoFeB and (b) Py. Black points: Simulated vortex length for $l = 3.9 \mu\text{m}$ and matching vortex circulation (l does not significantly influence the size of the vortices.) Blue points: Simulation for CoFeB including a growth induced anisotropy postulated by Baumgaertl et al. to explain their magneto-transport results [106]. The simulation considers a uni-axial anisotropy with $K_u = 5 \text{ kJ/m}^3$ with a different axis for each facet. Each axis is tilted by 55° towards the z axis with respect to the facet's surface normal. Red points: Length of the vortices extracted from XMCD-PEEM images. The vortex length is determined by the following procedure: We take 10% of the maximum intensity over the background to determine the beginning and end of a vortex. The difference is the length of the vortex. The general trend of increasing vortex length as a function of tube diameter is also predicted by Landeros et al. [75].

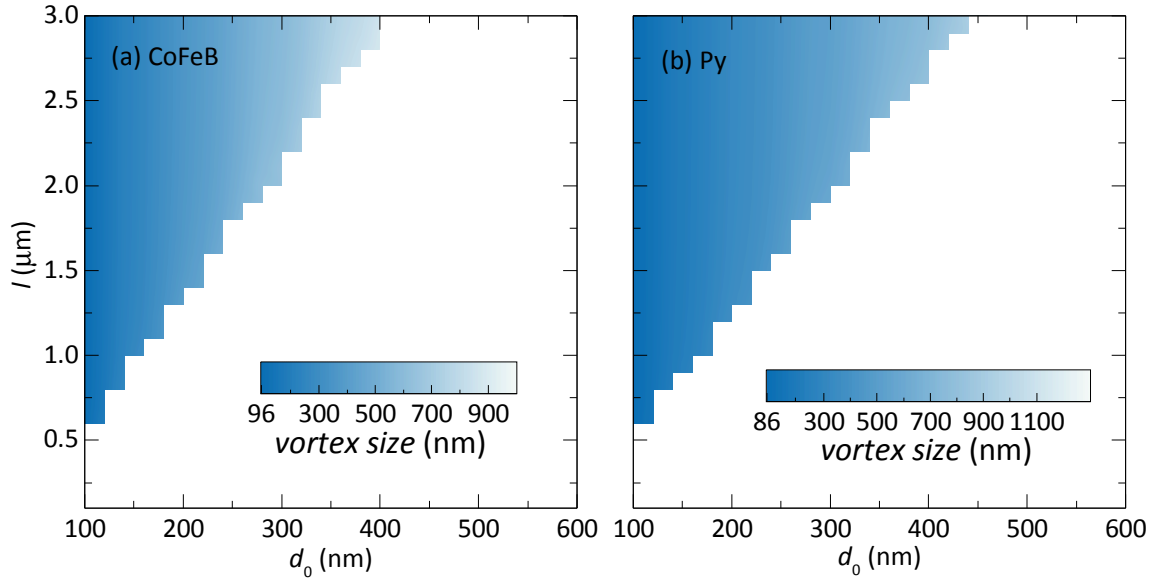


Figure B.4. | Phase diagrams for (a) CoFeB and (b) Py NTs. The vortex size is plotted as a function of the FNT length l and diameter d_0 . Nicely visible is that length of the FNT not significantly influences the size of the vortices.

Appendix C.

C: Scientific Systems

C.1. home-built scanning microscope

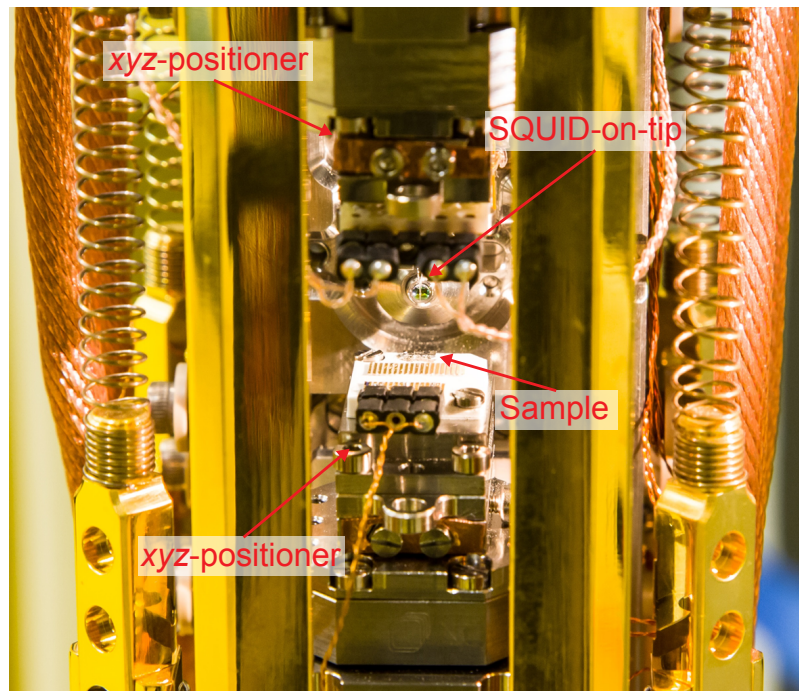


Figure C.1. | Image of the home-built scanning microscope. The design constitutes of two attocube stacks allowing the movement of the SQUID-on-tip and the sample in xyz -direction. For all SQUID-on-tip experiments just the bottom xyz -positioner is used. The stacks are mounted on a titanium frame, providing a rigid structure. The frame is suspended on springs with resonant frequency below 1 Hz, effectively isolating external vibrations. The thermal coupling to the frame is delivered via thick copper braids, also providing additional damping. In the microscope, in which the chiral artificial spin ice experiment have been performed one copper braid was longer compared to the others caused a tilt of 15° with respect to the plane. The experimental results are shown in subchapter 5.3 and 5.2.

C.2. home-built thermal Pb evaporation system

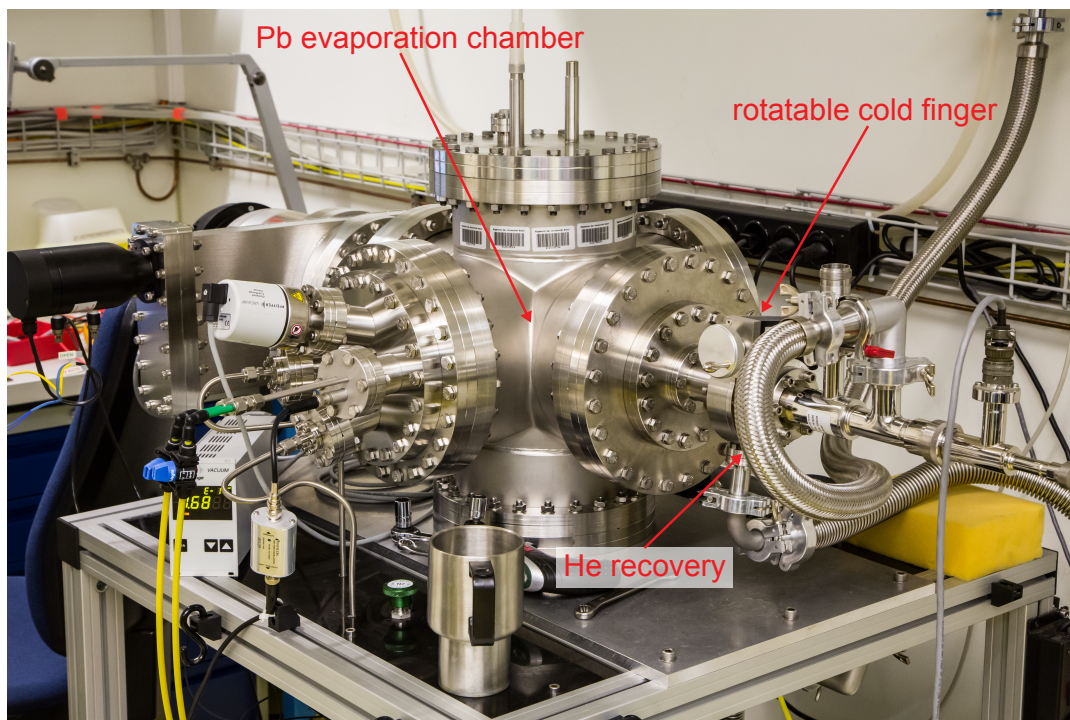


Figure C.2. | Image of the home-built Pb evaporation system. The cold finger allows to reach 4.2 K using liquid helium and is further rotatable 360°. The system allows to reach ultra-high vacuum (UHV) conditions with a base pressure of 1.5×10^{-7} mbar and a pressure during deposition of 8.0×10^{-7} mbar. The system further allows to introduce ^4He gas into the chamber at 1.0×10^{-5} mbar to facilitate pipette cooling.

Appendix D.

D: Pb nanoSQUID on Si-cantilever

D.1. Evaporation mask for the fabrication of Au-pads on the carrier chip

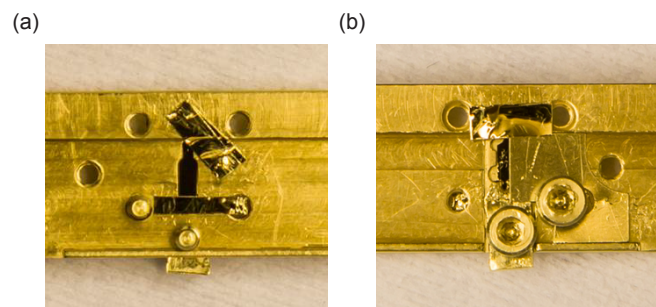


Figure D.1. | Picture of the used SOL evaporation mask for the fabrication of Au-pads for configuration ② on the carrier chip is shown. In (a) the bottom view of the SOL evaporation mask is shown to get the bottom Au-pad. In (b) the top view of the SOL evaporation mask is shown to get the top Au-pad. Two different types of evaporation masks were used. One mask consists of a thin metal sheet, which can be aligned precise, under an optical microscope using tweezers. After the first Au evaporation, this type of mask is repositioned such that it covers completely the already existing Au-pad, a small isolating gap of few μm forms between the two Au-pads. The second type of evaporation mask used, is sticky tape consisting of a polyimide film (Kapton). This tape can be cut into the required size, and placed in the proper position with tweezers under an optical microscope.

D.2. Si-cantilever properties

In this thesis two different types of Si-cantilevers are used:

For configuration ① and ② the commercially available ArrowTM TL1 Si-cantilevers are used. These Si-cantilevers have a length and width of $500 \mu\text{m} \pm 5 \text{ nm}$, respectively $100 \mu\text{m} \pm 5 \text{ nm}$ and depending on the type a thickness of $1 \mu\text{m}$ or 500 nm . The resonance frequency and the force constant of this type of Si-cantilevers is given to be 6 kHz , respectively 0.03 N/m . Depending on the geometry the resonance frequency as well as the force constant can range from $3 - 14 \text{ kHz}$, respectively from $0.004 - 0.54 \text{ N/m}$. These values are given by the manufacturer (NanoWorld AG).

For configuration ③ the commercially available ATEC-CONTTM AFM probe is used. This type of Si-cantilever is designed for contact mode AFM imaging. From the top a

tetrahedral tip protrudes perpendicular to the Si-cantilever. The mean width and length of this Si-cantilever is $50 \mu\text{m} \pm 5 \mu\text{m}$, respectively $450 \mu\text{m} \pm 10 \mu\text{m}$ and the thickness is $2 \mu\text{m} \pm 1 \mu\text{m}$. The height of the protruding tip at the apex is given to be 15 - 20 μm . The protruding tip at the end of the Si-cantilever is not straight at the apex and therefore has a suitable geometry to prevent that the evaporated Pb leads are not connecting in this area, when the used Pb evaporation angle is set to 90° . The resonance frequency and the force constant of this type of cantilevers are given to be 15 kHz, respectively 0.2 N/m. Depending on the geometry of the Si-cantilever the resonance frequency as well as the force constant can range from 7 - 25 kHz, respectively from 0.02 - 0.75 N/m. These values are given by the manufacturer (NanoWorld AG). For the Au-pads fabrication the same evaporation masks were used as already discussed and shown in detail in Appendix D.1.

D.3. Single Dayem bridge on a Si-cantilever

Label	Angle [x°]	t_{Pb} [Å]	FIB [\sim nm]	I_c [μA]	Thermal sensitivity	SC behaving
sA1°	-75/75	150/150	48	100	34 $\mu\text{A}/\text{K}$	sJJ
sA13	-75/75	150/150	56	20	4 $\mu\text{A}/\text{K}$	sJJ
sA18	-75/75	180/180	56	200	26 $\mu\text{A}/\text{K}$	sJJ

Table D.1. | Fabrication history of cantilevers milled for single junctions configuration. The used ArrowTM TL1 cantilevers have a length and width of 500 μm respectively 100 μm and have a thickness of 500 nm. SC: superconducting, sJJ: single Josephson Junction. ° this specific sJJ is described more in detail in chapter 6.2.

D.4. Configuration ①: Two Dayem bridges on a Si-cantilever

Label	Angle [x°]	t_{Pb} [Å]	FIB [\sim nm]	I_c [μA]	Thermal sensitivity	SC behaving
A04*	-50/50	200/200	300	450	-	sJJ
A07	-75/75	150/150	174	40	-	sJJ
A10	-75/75	180/180	39	50	-	sJJ
A12	-75/75	180/180	80	1200	-	sJJ

Table D.2. | Fabrication history of configuration ①. Configuration ① means that both Au contacts are located on top of the carrier chip and the two superconducting leads running down from the Au contacts to the apex on the side of the Si-cantilever. The used ArrowTM TL1 cantilevers have a length and width of 500 μm respectively 100 μm and a thickness of 500 nm. (* cantilever thickness: 1 μm). Characterization Notation: SC: superconducting, sJJ: single Josephson Junction.

D.5. Configuration ②: Two Dayem bridges on a Si-cantilever

Label	Angle [x°]	t_{Pb} [Å]	FIB [\sim nm]	I_c [μA]	Thermal sensitivity	SC behaving
N06	-90/90/0	260/260/150	410	750	-	sJJ
N07	-90/90/0	250/250/140	250	350	-	sJJ
N10	-70/80	230/230	310	40	32 $\mu\text{A}/\text{K}$	sJJ
N11	-70/80	230/290	270	1	-	sJJ
N20p°	-80/80	300/300	147	12.7	12.9 $\mu\text{A}/\text{K}$	tJJ
N22p	-80/80/0	320/320/50	134	1.4	-	sJJ

Table D.3. | Fabrication history of configuration ②. Configuration ② means that the superconducting leads running down at the top and bottom to the apex of the Si-cantilever. The therefore used ArrowTM TL1 Si-cantilevers have a length and width of 500 μm respectively 100 μm and have a thickness of 500 nm. Characterization Notation: s: single junction, p: pyramid geometry, SC: superconducting, sJJ: single Josephson Junction, tJJ: two Josephson Junction (SQUID). ° This SOL is described more in detail in chapter 6.3.

D.6. Configuration ③:

Label	Angle [$^{\circ}$]	t_{Pb} [\AA]	FIB [\sim nm] d, l_c	I_c [μA]	Thermal sensitivity	SC behaving
L01	0	180	190 , 45	216	very small	-
L02	0	150	150 , 40	-	-	resistive
L03	0	180	170 , 33	-	-	resistive
L04	0	210	180 , (53 · 81)	-	-	resistive

Table D.4. | Fabrication History of configuration ③. (ATEC-CONTTM). SC: superconducting, l_c : Length of the constriction, which form the template for the positions of the Dayem bridges.

Appendix E.

E: Chiral Artificial Spin Ice

E.1. Magnetic reversal measurements with applied in-plane magnetic fields

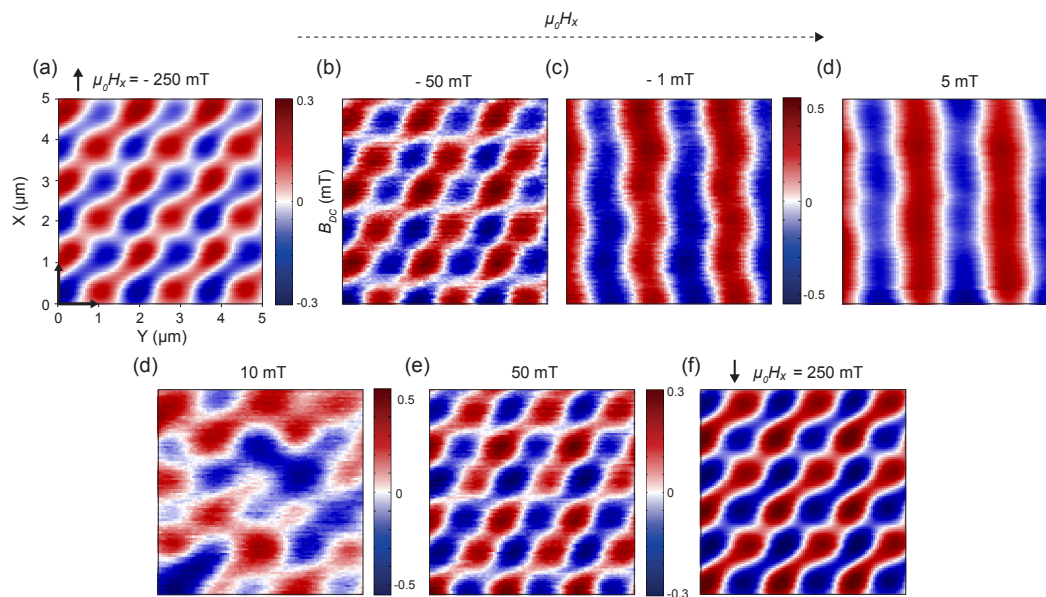


Figure E.1. (a,f), Shows a series of measured magnetic stray field distributions $B_z(x,y)$ of a chiral artificial spin ice system at different in-plane magnetic fields $\mu_0 H_x$. Starting field $\mu_0 H_x = -250$ mT in (a) towards $\mu_0 H_x = 250$ mT in (f). The opposite magnetic field direction is shown in subchapter 5.3. The color bar of (a), (c) and (e) also corresponds to that of (b), (d) and (f).

E.2. Magnetic reversal measurements with applied out-of-plane magnetic fields

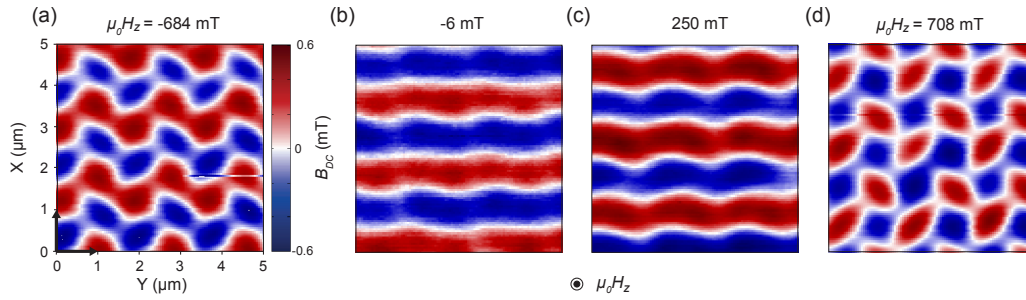


Figure E.2. | (a,d), Shows a series of measured magnetic stray field distributions $B_z(x,y)$ of a chiral artificial spin ice system at different out-of-plane magnetic fields $\mu_0 H_z$. Before imaging the magnetic field distribution at $\mu_0 H_z = -684 \text{ mT}$ a magnetic field of $\mu_0 H_z = -708 \text{ mT}$ of was applied to the system. The other magnetic field direction is shown in subchapter 5.2. The color bar of (a) also corresponds to that of (b,d).

Curriculum Vitae

Marcus Wyss

Department of Physics
University of Basel
Klingelbergstrasse 82
4056 Basel
Switzerland

Birth: July 2nd 1984 in Basel, Switzerland

Citizenship: Swiss

Education

- 2018 PhD (Dr. phil.) in Experimental Physics
University of Basel, Switzerland
- 2013 Master in Science in Nanosciences
University of Basel, Switzerland
- 2011 Bachelor in Science in Nanosciences
University of Basel, Switzerland
- 2007 Passarelle
Gymnasium Kirschgarten Basel, Switzerland
- 2005 Berufmaturitäts Schule (BMS)
Allgemeine Gewerbeschule Basel, Switzerland
- 2004 Eidgenössisch Diplomierter Elektroinstallateur
Allgemeine Gewerbeschule Basel, Switzerland

Scientific Talks at Conferences

- 2018 The 9th Joint European Magnetic Symposia (JEMS). 03 - 07 September, Mainz, Germany, Title: *Imaging the magnetic stray field of artificial chiral spin ice.*
- 2018 IEEE Conference on Advances in Magnetism 04 - 07 February, La Thuile, Italy, Title: *Imaging the magnetic stray field of an artificial chiral spin ice.*
- 2017 NCCR QSIT - Quantum Science and Technology, General Meeting. 01 - 03 February, Arosa, Switzerland, Title: *Nano-SQUID scanning probe magnetometry.*
- 2016 The 8th Joint European Magnetic Symposia (JEMS). 21 - 26 August, SECC: Scottish Exhibition and Conference Centre, Glasgow, UK, Title: *X-PEEM imaging of ferromagnetic nanotubes.*

List of Publications

(*) Publication covered in this thesis

1. A. Farhan, P. M. Derlet, A. Kleibert, A. Balan, R. V. Chopdekar, M. Wyss, L. Anghinolfi, F. Nolting, L. J. Heyderman,
Exploring hyper-cubic energy landscapes in thermally active finite artificial spin-ice systems,
Nature Physics **9**, 375 (2013)
2. A. Farhan, P. M. Derlet, A. Kleibert, A. Balan, R. V. Chopdekar, M. Wyss, J. Perron, A. Scholl, F. Nolting, L. J. Heyderman,
Direct Observation of Thermal Relaxation in Artificial Spin Ice,
Phys. Rev. Lett. **111**, 057204 (2013)
3. A. Farhan, A. Kleibert, P. M. Derlet, L. Anghinolfi, A. Balan, R. V. Chopdekar, M. Wyss, S. Gliga, F. Nolting, L. J. Heyderman,
Thermally induced magnetic relaxation in building blocks of artificial kagome spin ice,
Phys. Rev. B **89**, 214405 (2014)
4. A. Buchter, R. Woelbing, M. Wyss, O. F. Kieler, T. Weimann, J. Kohlmann, A. B. Zorin, D. Ruffer, F. Matteini, G. Tütüncüoğlu, F. Heimbach, A. Kleibert, A. Fontcuberta i Morral, D. Grundler, R. Kleiner, D. Kölle, M. Poggio,
Magnetization reversal of an individual exchange biased permalloy nanotube,
Phys. Rev. B **92**, 214432 (2015)
5. (*) M. Wyss, A. Mehlin, B. Gross, A. Buchter, A. Farhan, M. Buzzi, A. Kleibert, G. Tütüncüoğlu, F. Heimbach, A. Fontcuberta i Morral, D. Grundler, and M. Poggio
Imaging magnetic vortex configurations in ferromagnetic nanotubes,
Phys. Rev. B **96**, 024423 (2017)
6. A. Mehlin, B. Gross, M. Wyss, T. Schefer, G. Tütüncüoğlu, F. Heimbach, A. Fontcuberta i Morral, D. Grundler, and M. Poggio
Observation of vortex-nucleated magnetization reversal in individual ferromagnetic nanotubes,
Phys. Rev. B **97**, 134422 (2018)
7. (*) D. Vasyukov, L. Ceccarelli, M. Wyss, B. Gross, A. Schwarb, A. Mehlin, N. Rossi, G. Tütüncüoğlu, F. Heimbach, R. R. Zamani, A. Kovács, A. Fontcuberta i Morral, D. Grundler, M. Poggio
Imaging stray magnetic field of individual ferromagnetic nanotubes,
Nano Lett. **18**, 964 (2018)
8. (*) M. Wyss, S. Gliga, D. Vasyukov, L. Ceccarelli, G. Romagnoli, Robert L. Stamps, and M. Poggio
Imaging stray magnetic field patterns of chiral artificial spin ice,
in preperation (2019)